Faculty of Science and Technology

MASTER'S THESIS

Study program/ Specialization: Petroleum Engineering/ Production Engineering	Spring semester, 2011 Open access
Writer: Alexander Romanov	………………………………………… (Writer's signature)
Faculty supervisor: Aly Anis Hamouda	
Title of thesis: Thermal Recovery of Heavy Oil by (Steam-Assisted Gravity Drainage) SAGD Method	
Credits (ECTS): 30	
Key words: SAGD Bitumen Oil sand Steam injection Temperature distribution Heat transfer Temperature gradient	Pages: ………………… + enclosure: ………… Stavanger, June 14th, 2011 Date/year

THERMAL RECOVERY OF HEAVY OIL BY (STEAM-ASSISTED GRAVITY DRAINAGE) SAGD METHOD

By

Alexander Romanov

A THESIS SUBMITTED TO
DEPARTMENT OF PETROLEUM ENGINEERING
UNIVERSITY OF STAVANGER
IN PARTIAL FULFILMENT OF THE REQUIREMENT
FOR THE DEGREE OF
MASTER OF SCIENCE

University of Stavanger
June 2011

Acknowledgements

I would like to express my sincere gratitude to all those who helped me throughout my master's studies, who has been helpful in completing my master thesis and supported me during all time. I would like to say special thanks to:

- Professor Aly Anis Hamouda, my supervisor and my teacher, for his guidance, sharing of knowledge, and continuous encouragement throughout my master's studies.
- Department of Petroleum Engineering of UiS (Norway) and Oil and Gas Department of ASTU (Russia) and Statoil ASA (Norway), for their ASTUIS exchange program and financial support.
- My friends, colleagues and teachers at the University of Stavanger for their friendship, support and guidance.
- Last, but not least, my family, for their love, support, and encouragement.

ABSTRACT

This thesis presents experimental and numerical study of SAGD process. In spite of vast investigation done in literature for the area of steam injection, the mechanism(s) of heat flow in the reservoir are not fully understood. Understanding heat flow mechanism(s) and temperature distribution contribute to better optimization of the process and improvement of the numerical tools for simulation of SAGD process.

Experimental work and scaled numerical simulation performed to understand main key processes during SAGD. Basically, a model reservoir is constructed with heavy oil to be recovered by steam injection. Mapping of temperature/steam propagation within the model reservoir clearly demonstrates fast steam rise to the overburden and propagation horizontally at the top of reservoir away from vertical injector plan. Hence, top of reservoir becomes the second heating source for underlying layers.

Analysis of temperature distribution in the reservoir and temperature gradients around sensors shows that at interface of steam chamber convective heat transfer contributes to the heat flow. As steam chamber develops further, conduction mechanism becomes dominating.

Numerical simulation using dimensional analysis with experimental data, built in CMG's WinProp & STARS simulator version 2009 is done to investigate objectives of this work. Comparison of simulated results illustrates that numerical model has under estimation of temperature growth in beginning of SAGD process, but at later time results become similar to experimental measurements. It is also observed that time delay of temperature propagation is not the same for each part of reservoir, but it is smaller for closest area to steam injection source, and increases with the horizontal distance from SAGD well pair.

Other quantitative parameters, such as oil recovery and water consumption, estimated from numerical simulation, show fairly good agreement with experimental measurements.

Keywords: SAGD, bitumen, oil sand, steam injection, temperature distribution, heat transfer, temperature gradient

TABLE OF CONTENTS

LIST OF FIGURES

LIST OF FIGURES

LIST OF TABLES

LIST OF SYMBOLS

Symbol	Definition	Units
WI	Well index	
S_{Oi}	Initial oil saturation	
g	Gravity acceleration	m/s^2
k	Absolute permeability.	mD
x	Distance measured normal to the advancing front	m
U	Velocity of advancing front	m/s
t	Time	S
T_r	Initial reservoir temperature	C
T_s	Steam temperature	C
h	Vertical distance from production well to the top of formation	m
s	One-half slab thickness (m)	m
S_{Or}	Residual oil saturation	
T_a	Initial temperature of slab	C
$\overline{T_b}$	Average temperature of the slab	C
F_O	Fourier number	
t'	Dimensionless time	
k_r	Relative permeability	
r_w	Wellbore radius	m
f	Fanning friction factor	
r_a	Annulus radius	m
r_t	Tubing radius	m
R_g	Void fraction	
R	Universal gas constant	J/mol/K
v	Molar volume	
d_{ij}	Empirically determined interaction coefficient	
K	Function of Reynolds number	
k_a	Annulus permeability	mD
K_o	Conductive transmissibility	md-m
Re	Reynolds number	
S_w	Water saturation	
S_{wir}	Irreducible water saturation	
T_j	Transmissibility	md-m
Y	Flowing mass void fraction	

Greek symbols

Symbol	Definition	Units
ξ	Specific distance in from interface	m
v_o	Kinematics oil viscosity	cs
θ	Inclined angle of the steam interface from horizontal	degree
α	Thermal diffusivity of oil sand	m/s^2
v_S	Oil kinematic viscosity at steam temperature	cs
ρ	Mass density	kg/m^3
μ	Oil viscosity	cp
ϕ	Porosity	
λ_M	Fluid mobility	
$\dfrac{\partial \phi}{\partial x}$	Potential gradient	kPa/m
ε	Relative roughness	
Ω	Omega factor	
ω	Acentric factor	

Subscripts

Symbol	Description
o	oil
g	gas
w	water
s	steam
r	reservoir
h	horizontal
v	vertical
c	critical
t	tubing

CHAPTER I
INTRODUCTION

1 INTRODUCTION

This chapter consists of four sections. First section gives explanation about general aspects of bitumen. Second section of this chapter gives overview of Steam-Assisted Gravity Drainage research. Third section gives explanation about objectives of this study.

1.1 General Aspects of Bitumen

The area of interest of this thesis is production of bitumen from tar sands (oil sands) by the help of enhanced recovery methods. Tar sands consist of sand, bitumen and water as shown in **Figure 1-1**. Bitumen is a mixture of organic liquids that are highly viscous, black, sticky, and composed primarily of highly condensed polycyclic aromatic hydrocarbons. At room temperature, the bitumen has a consistency much like cold molasses. It typically contains more sulfur, metals and heavy hydrocarbons than conventional crude oil (Government of Alberta)[23].
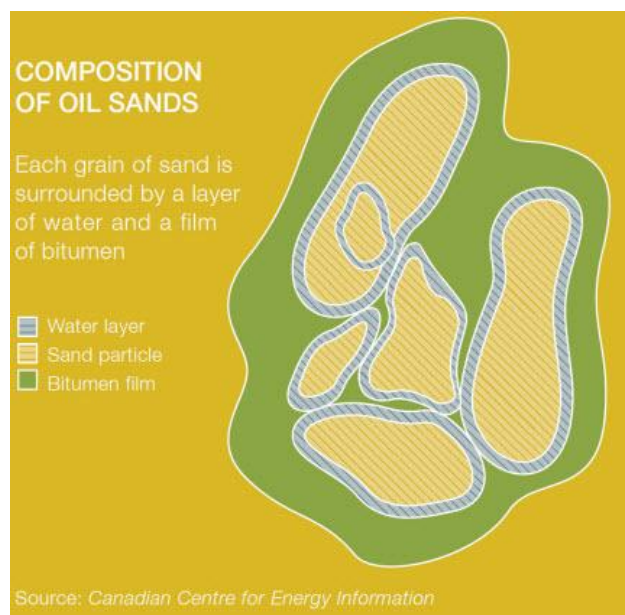
Figure 1-1: Composition of oil sands (Source: Canadian Center for Energy Information)[10]

Historically the term heavy oil and bitumen has been used to describe oil that is more dense and viscous than conventional oil. In 1982 a committee of UNITAR (United Nations Institute for Training and Research) delegates created a two step classification process. Firstly, materials with gas-free viscosity greater than 10000 mPa·s at reservoir temperature are classified as immobile bitumen. Secondly density is used to sub-classify oils with viscosities of 10000 mPa·s or less (Miller, 1994)[34]. According to this classification, bitumen is defined as crude oil with viscosity >10000 mPa·s and density >1000 kg/m3 or °API <10.

Oil sand history started from a hot water flotation process developed to produce bitumen for roofing and road surfacing, by entrepreneur R.C. Fitzsimmons **i**n the 1920s at a plant near Bitumount, 80 kilometers north of Fort McMurray. Dr. Karl Clark, a scientist with the Alberta Research Council in the 1920s, pioneered experiments with a hot water flotation process which involved mixing oil sand with hot water and aerating the resultant slurry. This would then separate into a floating froth of bitumen and a clean layer of sand which would settle tat the bottom of the tank. In 1936 another developer, Max Ball, founded Abasand Oils Ltd. His plant west of Fort McMurray produced diesel oil from the oil sands. The first commercial project started in 1963, and prior to the construction decision ownership rested with the Sun Oil Company (later Suncor Energy). The Suncor project came on stream in 1967 and became the world's first oil sands operation (Syncrude Canada ltd.)[44].

The Western Hemisphere possesses 69 percent of the world's technically recoverable heavy oil and 82 percent of the technically recoverable natural bitumen. In contrast, the Eastern Hemisphere possesses about 85 percent of the world's light oil reserves. Heavy oil and natural bitumen are present worldwide. The largest extra-heavy oil accumulation is the Venezuelan Orinoco heavy-oil belt containing 90 percent of the world's extra-heavy oil when measured on an in-place basis. Eighty-one percent of the world's known recoverable bitumen is located in the Alberta, Canada accumulation. Together the two deposits contain about 3,600 billion barrels of oil in place. For a detailed description of major heavy oil resources around the world, see **Figure 1-2**.
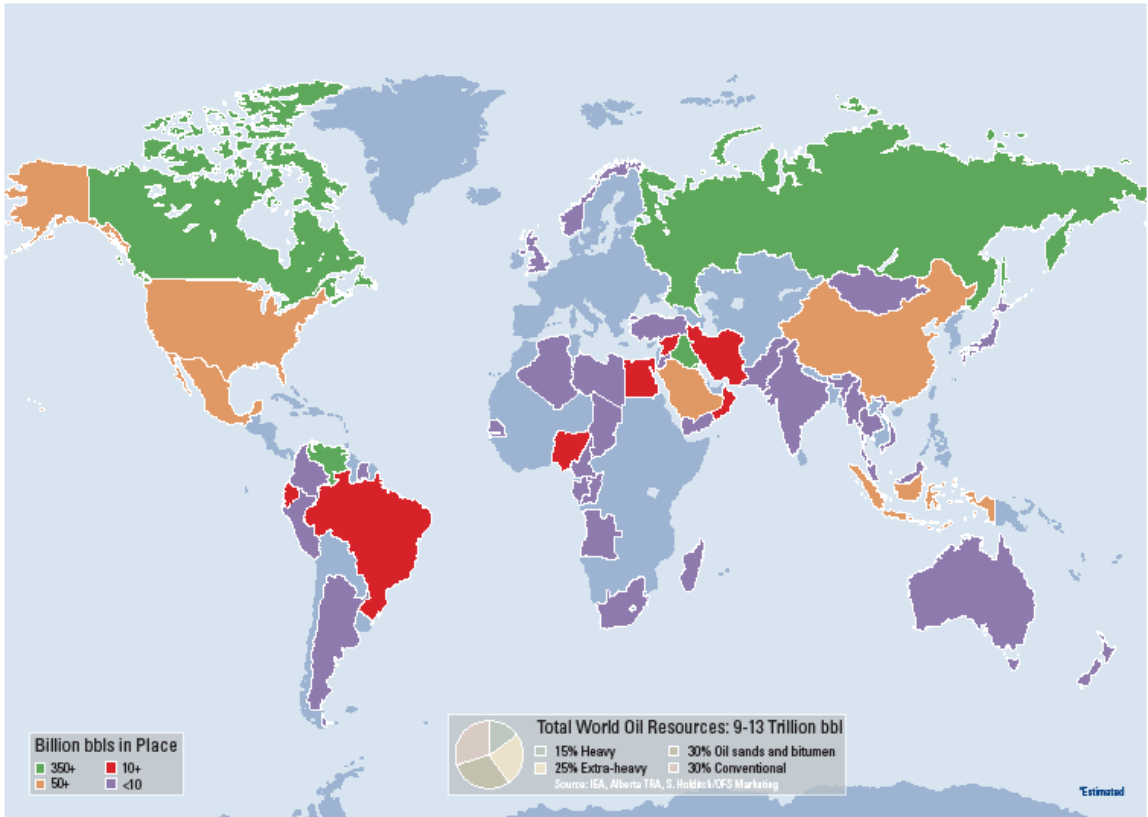
Figure 1-2: Worldwide heavy oil resources (after www.heavyoilinfo.com)[25]

The IEA estimates that there are 6 trillion barrels of heavy oil worldwide, with 2 trillion barrels ultimately recoverable. Western Canada is estimated to hold 2.5 trillion barrels, current reserves amounting to 175 billion barrels (BBO). Venezuela is estimated to hold 1.5 trillion barrels, with current reserves of 270 billion barrels. Russia may also have an excess of 1 trillion barrels of heavy oil (Flint, 2005)[19].

Production methods can be classified as surface mining or well production. Primary subsurface production methods include cold production (horizontal and multilateral wells, water flood, and cold heavy oil production with sand) and thermal production (cyclic steam stimulation, steamflood, and steam-assisted gravity drainage).

However, there are several barriers to the rapid growth of heavy oil and extra-heavy oil, and the bitumen production. Open-pit mining has a large environmental impact and can only exploit resources near the surface. Open-pit mining is a mature technology and only evolutionary improvements in technology are likely. By contrast, there are several commercial in situ production technologies and several more in the research or pilot phase. Many of the in situ production methods require an external energy source to heat the heavy oil in order to reduce its viscosity. Natural gas is currently the predominant fuel used to generate steam, but it is becoming more expensive due to short supply in North America. Alternative fuels such as coal, heavy oil, or byproducts of heavy oil upgrading could be used, but simply burning them will release large quantities of the green house gas CO_2. One option is gasification with CO_2 capture and sequestration to minimize greenhouse gases. Nuclear power has also been proposed, but faces societal opposition. Another fuel option is using the unconventional oil itself by injecting air into the reservoir for in situ combustion.

Clerk (2007)[11] reviewed other in situ methods undergoing pilot testing are using a solvent to reduce heavy oil viscosity by itself or combined with steam. These could reduce energy requirements and possibly open resources that otherwise are located at too large depths, in arctic regions, or offshore where steam injection is difficult. Heavy oil, extra-heavy oil, and bitumen projects are large undertakings and very capital intensive. In addition to the production infrastructure, additional upgrading, refining, and transportation facilities are needed.

Despite the large reserves, the cost of extracting the oil from bituminous sands has historically made production of the oil sands unprofitable: the cost of selling the extracted crude would not cover the direct costs of recovery. These costs are related to labour during sand mining and fuel needed to extract the crude.

In 2006, the National Energy Board of Canada[36] estimated the operating cost of a new mining operation in the Athabasca oil sands to be C$9 to C$12 per barrel, while the cost of an in-situ SAGD operation (using dual horizontal wells) would be C$10 to C$14 per barrel. The costs are comparable to the operating costs for conventional oil wells which can range from less than one dollar per barrel in Iraq and Saudi Arabia to over six dollars in the United States and Canada's conventional oil reserves.

The capital cost of the equipment required to mine the sands and hault it to processing is a major consideration when starting production. The NEB estimates that capital costs raise the total cost of production to C$18 to C$20 per barrel for a new mining operation and C$18 to C$22 per barrel for a SAGD operation. This does not include the cost of upgrading the crude bitumen to synthetic crude oil, which makes the final costs C$36 to C$40 per barrel for a new mining operation.

Edmunds and Gittins (1993)[15] pointed out main parameters for SAGD projects. Bitumen is a low value product, and therefore commercial exploitation demands the most efficient recovery process. Calendar Day Oil Rate (CDOR) and Steam/Oil Ratio (SOR) are the strongest determinants of the capital and operating costs of thermal recovery. The CDOR determines the initial investment required for drilling, completion, and tie in of the wells. Field operating costs, especially labor, are more a function of the number of wellheads than of the field production capacity, so high CDOR's help to minimize unit production costs. The impact of the SOR on fuel costs is widely appreciated, but in addition, since a major portion of the surface facilities are concerned with sourcing, treating, boiling, separating, recycling, and disposing of water, the SOR has a very substantial impact on capital costs (the mass of water produced by a SAGD scheme is approximately equal to the injected steam).

1.2 Steam-Assisted Gravity Drainage

Green and Willhite (1998)[24] stated that thermal recovery processes rely on the use of thermal energy in some form both to increase the reservoir temperature, thereby reducing oil viscosity and to displace oil to a producing well. The motivation for developing thermal recovery processes was the existence of major reservoirs all over the world that were known to contain billions of barrels of heavy oil and tar sands not possible to produce with the help of conventional techniques. In many reservoirs, the oil viscosity was so high that primary recovery on the order of a few percent of original oil in place was common. In some reservoirs, primary recovery was negligible.

Steam injection base has been used for many decades to improve recovery of heavy oil. The main mechanism during steam injection is the reduction of oil viscosity and residual oil saturation by increasing the reservoir temperature. This technology is now being exploited thanks to increased oil prices. While traditional drilling methods were prevalent up until the 1990's, high crude prices of the 21st Century are encouraging more unconventional methods (such as SAGD) to extract crude oil. Summary of screening criteria for steam based enhanced oil recovery is shown in **Table 1-1**.

Table 1-1: Screening criteria for steam based enhanced oil recovery (Source: Taber et al., 1996)[45]

EOR method	Oil properties			Reservoir characteristics				
	Gravity, API	Viscosity, cp	Composition	Oil saturation (% PV)	Formation type	Net thick-ness, ft	Average permea-bility, md	Depth (ft)
Steam	>8-13,5	<200000	N.C.	>40	High porosity sand/ sandstone	>20	>200	>4500

The steam-assisted gravity drainage approach employs gravity drainage to move the crude oil to the production well, but the contact with the reservoir is much greater because horizontal wells are employed. These wells have much greater contact with the reservoir than do conventional wells and adequate flows can be achieved with heads equivalent to that obtained from gravity: this is not possible with vertical wells. It is the use of horizontal wells which allows oil to be produced at economical rates with the main driving force being gravity. The process allows oil to remain hot as it drains downwards and there is a systematic coverage of the reservoir so that high recoveries can be achieved (Butler, 1994)[8].

The process has several features:

- The displacement of the oil is systematic and high recoveries can be obtained;

- In suitable applications, oil to steam ratios higher than those found for conventional steamflooding can be achieved;

- The process can be used in even the heaviest of bitumen reservoirs without extensive preheating. The feature making this possible is that once the oil is heated, it remains hot as it drains to the production well. This is unlike conventional steamflooding where oil which is displaced from the steam chamber tends to cool on its way to production.

Good et al. (1994)[22] described two basic SAGD mechanisms exist in oil sands: ceiling drainage and slope drainage influencing performance:

- Ceiling drainage occurs as the steam chest is expanding upwards. Steam rises to the ceiling and heated bitumen is pulled away from the front and drains in a counter current fashion. Limits on the vertical component of a local pressure field in which counter current flow can occur and on bitumen drainage rate are the reasons why pairs of wells are used. Steam chest (ceiling) rising rate, an important aspect of the process, is a strong function of steam temperature and vertical permeability;

- Slope drainage first analyzed by scaled physical models by Butler and Stephens (1981)[4] is the main SAGD producing mechanism. It was found that the bitumen production rate is only a function of the height of the slope, and not the angle of recline. Shallow angle slopes have lower gravity components parallel to the slope

but have longer slopes exposed to steam. The two factors tend to cancel each other out. It was also found that the bitumen production rate is a function of the square root of permeability and height and the inverse square root of bitumen viscosity at steam conditions. This is a consequence of the need to maintain mobility in the drainage layer by conduction;

- Other reservoir conditions which influence SAGD performance include heterogeneities and solution gas. With respect to heterogeneities, AOSTRA studies indicate that the influences of shale and clay layers are complex and highly dependent on their actual dimensional distribution. Continuous shale with only a few breaks may severely restrict gravity drainage. If barriers are small and widely spaced however they will not seriously impede drainage and may actually increase the number of sloped surfaces exposed to conduction heating.

SAGD is a combined conduction/convection mechanism that is more like ablation (i.e., propagation of a melting front into a solid material) than displacement, the usual petroleum engineering paradigm for thermal recovery. The density difference between the steam and bitumen causes the bitumen to drain to the bottom of the chamber along with the steam condensate that is formed as a result of the heat conduction ahead of the front. The rate of drainage is controlled by permeability. Liquids within the steam chamber drain very rapidly relative to the speed of frontal advance, so that the steam chamber gas saturations are high and the water and oil saturations are close to the residual values. Cumulative oil production is nearly proportional to the steam chamber volume. (Edmunds et al., 1991)[16]

Though SAGD is an attractive method for heavy oil reservoirs, there are some restrictions for reservoir parameters to be favorable for SAGD operations. Based on the simulation results of a typical Cold Lake reservoir in Alberta, reservoirs with a minimum thickness of 20 m, vertical permeability of 2.5 Darcy and relatively clean sand reservoirs are favorable for SAGD application (Shin and Polikar, 2007)[42]. Another simulation study, done by Kamath et al (1993)[30], shows that SAGD performance improves significantly with high steam injectivities, low mobile water saturation near the producer, absence of continuous shale barriers, high vertical to horizontal permeability ratio and optimum injector-producer vertical spacing.

Reservoir parameters making the SAGD method unattractive[2,33]:

- Pay thickness less than 12 m with continuous quality pay (>10wt% oil);

- Permeability less than 3 Darcy;

- High both areal and vertical heterogeneity in permeability and reservoir mobility;

- Water saturations too high compared to irreducible water saturations S_{wir} ;

- Reservoirs with large gas-cap or bottom water zone;

- Reservoir operating pressure less than 1000 kPa;

- High adverse fluid/rock interactions.

A major consideration in the development and operation of SAGD projects is the cost of generating steam and associated CO_2 emission. Important factors that must be considered are the steam oil ratio (SOR) and the cost of the fuel required per cubic meter of steam.

With heat recovery it takes about 500 SCF of natural gas to produce one barrel of 100% quality steam (89 Sm^3/m^3). In efficient SAGD projects, the SOR is about 2 to 5, depending on the reservoir and fluid properties, so the volume of gas required falls in the range of 1000 SCF to 2500 SCF per barrel of produced oil. Since the value of the produced oil has not increased proportionately, there is an increased need to minimize fuel consumption and cost in SAGD operations (Butler, 2001)[7].

The second concern is considerable water consumption. SAGD projects are big water consumers in the regions of production. Although nowadays operators tend to use mainly underground sources of water and improve its recycling, still reduction of water consumption remains vital issue. The third concern is low thermal efficiency of SAGD. The reason of low thermal efficiency is that during the recovery process steam chamber growth should be maintained by continuous steam injection and the entire part of the reservoir that is depleted becomes heated to the steam temperature. Moreover, after the steam chamber hits the top of the formation, heat losses to the overburden layers start increasing and the larger the area of steam chamber/top of the formation contact and its temperature the larger the heat losses.

Butler (1998)[6] summarized different pitfalls and problems experienced when developing SAGD projects:

- Reservoir quality is poorer than expected; e.g., lower S_{oi} and higher S_w.

- Production well screen is damaged by steam-driven sand erosion – particularly in pumpless, self-flowing wells.

- Lifting capacity is inadequate and steam chamber can not be drawn down – particularly with very long wells.

- Steam chamber pressure is too low to prevent water intrusion. The wells may be too long for the available boiler capacity.

Singhal et al. (1998)[43] also mentioned other potential problems and limitations of SAGD

- hot effluent/ high water-cut production,

- frequent changes in operating regime (making management of SAGD projects a labour intensive one),

- deterioration of production at late stages,

- high operating costs.

During the years of extensive piloting and commercial implementation a lot of improvements of the existing technology have been proposed to address above mentioned and other technological issues (Ibattullin and Zolotukhin, 2009)[26]. All the attempts to improve SAGD performance could be subdivided into the following categories):

- Improvements at the one well pair scale (High/Low Pressure-SAGD, subcool optimization, artificial lift, injected fluid modification, *etc*);

- Improvements at the reservoir scale (XSAGD, Fast-SAGD, JAGD, geomechanical improvement, *etc*);

- Improvements at the field scale including integrated schemes with production and on-site upgrading (NEXEN/OPTI project, *etc*).

- Improvement of injected fluid composition (ES-SAGD, VAPEX, SAGP, SAS, SAP, *etc*).

The SAGD process has been investigated using theoretical, numerical, and experimental studies. Kisman and Yeung (1995)[31] conducted reservoir simulation sensitivity studies for the Burnt Lake oil sands lease and found that the lower the operating pressure, the lower the oil rate and SOR. Ito and Suzuki (1999)[29] analyzed SAGD simulation results in the Hangingstone Reservoir and showed that the optimum subcool, which is the temperature difference between the injected steam and the produced fluids, lies between 30 and 40°C. Egermann et al. (2001)[17] proposed a method based on numerical simulation to obtain and maintain an optimized development of the steam chamber throughout the production life of the well pair. The proposed approach was applied to Mobil's Celtic SAGD pilot. They showed that roughly 100% incremental oil production can be achieved by adjusting the steam injection rate to the potential of the reservoir and monitoring the production rate to keep the steam chamber as large as possible but far enough away from the production well to prevent steam breakthrough. The presence of bottom water further aggravates this situation because it may dramatically increase heat losses.

Gates and Chakrabarty (2005)[21] used a genetic algorithm together with the STARS™ simulator to optimize the cSOR by altering the steam injection pressure in a generic two-dimensional McMurray Reservoir model. They concluded that the cSOR can be reduced significantly by choosing to operate SAGD with a profile of steam injection pressures throughout the life of the process rather than with constant injection pressure. The results indicate that the steam injection pressure should be relatively high before the chamber contacts the overburden, and lower afterwards to reduce heat losses to the caprock.

Edmunds and Gittins(1993)[15] discussed the concept of steam distribution in SAGD wells and the importance of the pressure drop in the injection liner in defining chamber shape and process performance. The general concept is as follows: injection well pressure gradients are inferred into the reservoir and overpower the relatively small pressure gradients in the production wells, resulting in a sloped fluid interface. The fluid accumulates to compensate for the overall pressure gradients by increasing hydrostatic head in the lower pressure areas of

the reservoir. Thus, it is generally accepted that optimal injection wells should be designed to ensure that the average pressure drop is less than 45 kPa for well pairs with a vertical separation of 5 m.

Ong and Butler (1990)[37] also evaluated the impact of wellbore pressure drop and well size on SAGD performance, focusing on mixed viscosity relationships and the hydraulic capacity of the production well. They concluded that SAGD performance would be impeded if the well diameter was too small, which would cause hydraulic losses in the well and skew the liquid interface parallel to the well pair.

1.3 Objectives of This Study

1) To investigate heat flow mechanisms in thermal recovery with steam injection from experimental work.

2) To investigate temperature distribution within the reservoir during SAGD process.

3) To provide different approaches for understanding the mechanisms of reservoir heating for better optimization of the used steam.

4) To compare experimental results with Butler's analytical model.

5) To compare experimental results with numerical simulation model.

CHAPTER II
THEORETICAL BACKGROUND

2   THEORETICAL BACKGROUND

This chapter consists of two sections. First section gives a description of Steam-Assisted Gravity Drainage theory form Butler's analytical model. Second section provides description of discretized wellbore option in the numerical simulator used for SAGD model.

2.1 Steam-Assisted Gravity Drainage Theory

The recovery of heavy crudes using a special form of steamflooding has become known as Steam-Assisted Gravity Drainage (SAGD) process. The gravity drainage idea was originally conceived and developed by Dr. Roger Butler in the 1970's, about the same time as the introduction of the horizontal well. He tested the concept with Imperial Oil in the 1980, in a pilot at Cold Lake featuring one of the first horizontal wells in the industry with vertical injectors.

Alberta Oil Sands Technology and Research Authority (AOSTRA) commenced development of the Underground Test Facility (UTF) in December 1982. Feasibility studies were completed by January 1984. One of the first processes selected for testing at the UTF was SAGD. Drilling of the wells for a 3 well pair technical pilot (Phase A) of the twin well steam assisted gravity drainage process was initiated in October 1986 and completed and tied in during 1987. The pilot was very successful and lead to a Phase B pre-commercial pilot. The AOSTRA patented SAGD process has been proven economically feasible for the Athabasca McMurray Oil Sands with shaft and tunnel access at the UTF site (Good et al., 1994)[22].

Steam assisted gravity drainage is a thermal in-situ heavy oil process. The process begins with a preheating phase by circulating steam in both wells so that bitumen is heated enough to flow to the lower production well. The steam chamber heats and drains more and more bitumen until it overtakes the oil bearing pores between well pair. Steam circulation in the production well is then stopped and injected into the upper injection well only. The cone shaped steam chamber, anchored at the production well, started developing upwards from the injection well. As new bitumen surfaces are heated, the oil drops in viscosity and flows downwards along the steam chamber boundary into the production well due to gravity as seen on **Figure 2-1** (Butler, 1991)[9].
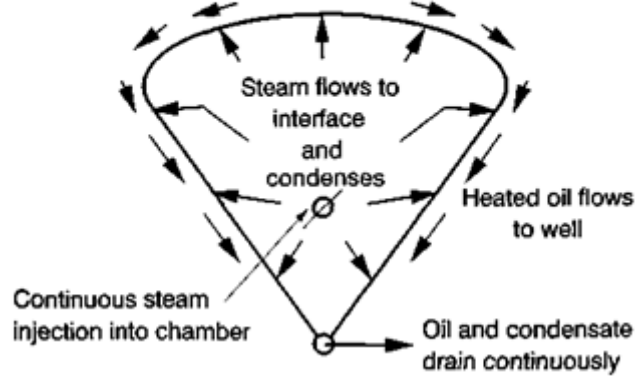
Figure 2-1: Typical horizontal well pair in Butler's SAGD[9]

The interface is at steam temperature T_s. Beyond the interface, into reservoir, successive layers of material are cooler. Oil drainage rate due to gravity is described by Darcy's law per unit length of the horizontal producer

$$dq = \frac{k\,g\sin\theta}{v_o}\,d\xi \qquad\qquad \textbf{(Eq. 2-1)}$$

Where:

v_o : kinematics oil viscosity

g : gravity acceleration

θ : inclined angle of the steam interface from horizontal

k : absolute permeability.

In this model, reservoir heating was assumed to be due to steady state heat conduction, and the steam zone interface was assumed to move uniformly at a constant velocity U as shown in **Figure 2-2**. The temperature distribution between the constant velocity steam zone interface and unheated reservoir was thus given by

$$\frac{T-T_r}{T_s-T_r} = e^{-U\xi/a} \qquad\qquad \textbf{(Eq. 2-2)}$$

Where:

$\xi = x - U\,t$: specific distance from the interface

x : distance measured normal to the advancing front

U : velocity of advancing front

t : time

T_r : initial reservoir temperature (21 deg C)

T_s : steam temperature (103 deg C).
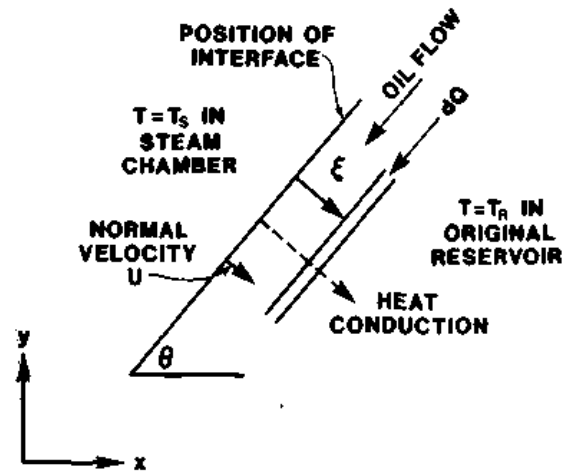
Figure 2-2: Schematic diagram to calculate fluid displacement in SAGD process in Butler's model[9]

If the reservoir was unheated, then v_o in **Equation (2-1)** would be kinematic oil viscosity at reservoir temperature. Increase in flow due to heating is then given by:

$$dq - dq_r = kg \sin\theta \left(\frac{1}{v} - \frac{1}{v_R} \right) d\xi$$

(Eq. 2-3)

Interpretation of **Equation (2-3)** results:

$$q = kg \sin\theta \int_0^\infty \left(\frac{1}{v} - \frac{1}{v_R} \right) d\xi$$

(Eq. 2-4)

To evaluate the integral it is necessary to know viscosity of the oil as a function of distance from the interface. Since **Equation (2-2)** gives the temperature as a function of distance, it is necessary to know the viscosity only as a function of temperature to evaluate q.

The variation of viscosity with temperature depends upon the properties of the particular oil in the reservoir. One arbitrary form of temperature function that corresponds reasonably well to the performance of actual oil over the range of interest is given by **Equation (2-5)**

$$\frac{v_S}{v} = \left(\frac{T - T_R}{T_S - T_R} \right)^m$$

(Eq. 2-5)

In order to use Equation (2-5) it is necessary to specify the viscosity at the steam temperature T_S and a value for the parameter m. For heavy crudes, it is found that the parameter m should have a value of about 3 to 4.

If the kinematic oil viscosity ν_R is very high, $\dfrac{1}{\nu_R} \approx 0$, and:

$$\int_0^\infty \left(\frac{1}{\nu} - \frac{1}{\nu_R} \right) d\xi = \frac{\alpha}{U} \frac{1}{m\nu_S} \qquad \textbf{(Eq. 2-6)}$$

Combining **Equation (2-4)** and **(2-6)** and eliminating the integrals gives the expression shown in **Equation (2-7)** for the flow q.

$$q = \frac{kg\alpha \sin\theta}{m\nu_S U} \qquad \textbf{(Eq. 2-7)}$$

The property m was used in the empirical equation of the flow rate to account for the effect of temperature on viscosity. Using the relationship between temperature and distance described by **Equation (2-2),** it is possible to change the variable of integration in **Equation (2-4)** from distance to temperature. The expression for $d\xi$ given by **Equation (2-8)** is obtained by differentiating **Equation (2-2)** and combining the result with **Equation (2-2)** by eliminating the exponential term.

$$d\xi = -\frac{\alpha}{U} \frac{dT}{T - T_R} \qquad \textbf{(Eq. 2-8)}$$

Substitution of $d\xi$ from **Equation (2-8)** gives the following expression for the integral of **Equation (2-4)**

$$\int_0^\infty \left(\frac{1}{\nu} - \frac{1}{\nu_R} \right) d\xi = \frac{\alpha}{U} \int_{T_R}^{T_S} \left(\frac{1}{\nu} - \frac{1}{\nu_R} \right) \frac{dT}{T - T_R} \qquad \textbf{(Eq. 2-9)}$$

Equation (2-9) allows the evaluation of the integral for any specified dependence of viscosity on temperature. In order to continue using this equation it is convenient to redefine m. Combining **Equation (2-6)** and **(2-9)** and solving for m results in:

$$m = \left[\nu_S \int_{T_R}^{T_S} \left(\frac{1}{\nu} - \frac{1}{\nu_R} \right) \frac{dT}{T - T_R} \right]^{-1} \qquad \textbf{(Eq. 2-10)}$$

This defines m as a function of the viscosity-temperature characteristics of the oil, the steam temperature, and the reservoir temperature. For a specific type of oil with experimental data on its viscosity-temperature curve, the m exponent can be calculated accordingly. As such, m is mainly a function of the characteristics of the viscosity-temperature relationship for the oil (or bitumen) being considered, in the steam to reservoir temperature range m is a dimensionless number that does not vary rapidly with either T_R or T_S. In many applications it is adequate to consider m as a constant.

Relationship between the flow of oil q and the front velocity can be defined by considering the material balance at the interface. If the interface is advancing, then oil must be flowing out of the region at a faster rate than it is flowing in; it is the difference in the rates that determines the advance of the interface rather than rate itself. The following oil drainage rate equation is obtained:

$$q = \sqrt{\frac{2\phi\Delta S_O kg\alpha h}{mv_S}} \quad \text{(one side)} \tag{Eq. 2-11}$$

Equation (2-11) is marked *one side*. It gives the rate at which oil drains from one side of the steam chamber. For the usual field situation where oil is draining from both sides of the steam chamber, the rate must be doubled. The equation above is a function of the drainage height but is not dependent on the shape of the interface or on its horizontal extension.

It is assumed if that the steam chamber initially is a vertical plane above the production well, then the horizontal displacement is given as function of time t and height y by **Equation (2-12).**

$$x = t\sqrt{\frac{kg\alpha}{2\varphi\Delta S_O mv_S (h-y)}} \tag{Eq. 2-12}$$

Equation (2-12) may be rearranged to give y as a function of x and t, as:

$$y = h - \frac{kg\alpha}{2\varphi\Delta S_O mv_S}\left(\frac{t}{x}\right)^2 \tag{Eq. 2-13}$$

Values of dimensionless form of x and y at different t are plotted in **Figure 2-3**.
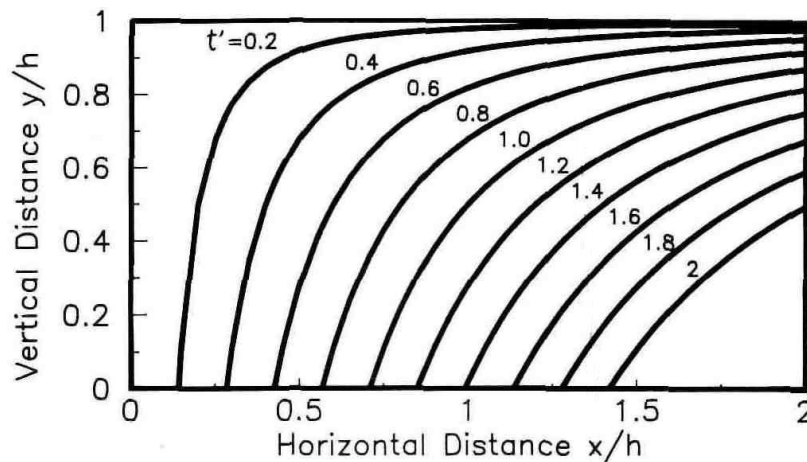
Figure 2-3: Calculated interface curves (Source: Butler, 1991)[9]

It is important to note that the model assumed conduction as the dominant mode of heat transfer as the temperature difference was developed from **Equation (2-2)**, and the entire

process was localized at the interface. Convection of heat ahead of steam zone interface was not considered.

It was implicitly assumed that all the heated oil ahead of the interface was produced once it reached the bottom of the steam zone. As such, no horizontal potential gradient was required for the oil production ahead of the steam zone interface at the bottom of the steam zone. In reality the pressure gradient between the horizontal injector and producer would be required to provide the driving force (Priyadi, 2008)[39].

The dimensionless similarity between experimental and numerical model could be achieved by using the dimensionless time as determined by

$$t' = \frac{t}{h}\sqrt{\frac{kg\alpha}{\phi \Delta S_O m \nu_S h}}$$ **(Eq. 2-14)**

Where:

t	: time
h	: vertical distance from production well to the top of formation
k	: absolute permeability
g	: gravity acceleration
α	: thermal diffusivity of oilsand
ϕ	: porosity
$\Delta S_O = S_{Oi} - S_{Or}$	: differential oil saturation
m	: function of the viscosity-temperature characteristics of the oil, the

steam temperature, and the reservoir temperature

ν_S	: oil kinematic viscosity at steam temperature.

Analysis of dimensionless similarity through usage of dimensionless time shows that the only condition for dimensionless time does not overcome this problem.

The extent of the rise of the temperature in a solid body being heated by conduction is determined by the dimensionless number

$$F_O = \frac{\alpha t}{h^2}$$ **(Eq. 2-15)**

F_O is known as the Fourier number. It may be viewed as dimensionless time, comparing the depth of the penetration of isotherms into a body that is being heated by conduction, to its physical dimensions, For dimensionless similarity between the experimental and numerical model, F_O and t' should be equal. If they are equal in both models, it follows that their quotient

$$B_3 = \frac{t'}{F_O} = \sqrt{\frac{kgh}{\alpha\phi\Delta S_O m\nu_S}}$$

(**Eq. 2-16**)

is also equal. This is the additional condition for dimensionless similarity.

Extension of the original SAGD theory was described by Butler and Stephens (1981)[4]. A point of concern related to the solution derived in the original theory was that the oil draining down the interface curves would have to drain horizontally to the well after it reached the bottom. Some of the available head must be used to cause this lateral flow. It was assumed that the lower parts of interface curve of **Figure 2-3** can be replaced by a tangent drawn from the production well to the curves as shown in **Figure 2-4**.
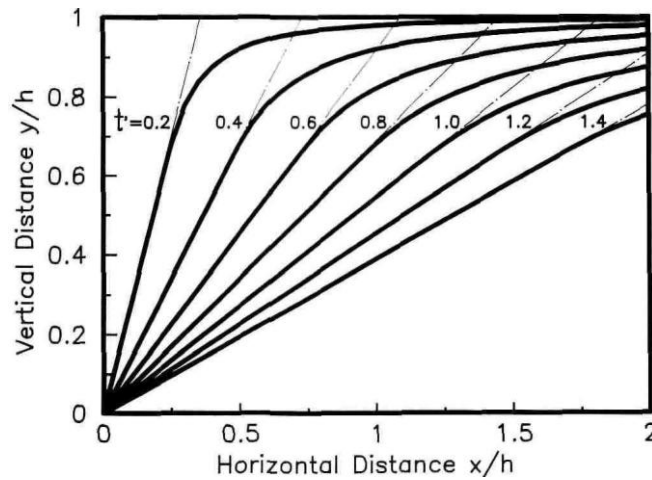
Figure 2-4: Calculated interface positions for an infinite reservoir using TANDRAIN assumption (Source: Butler, 1991)[9]

Effective head causing oil drainage rate is reduced from h to 75% of h. The remainder of the head is used to cause horizontal movement of the draining oil.

$$q = \sqrt{\frac{1.5\phi\Delta S_O kg\alpha h}{m\nu_S}}$$

(**Eq. 2-17**)

Butler and Petela (1989)[3] studied the growth of the steam zone during the initial stage of the SAGD process. The growth of the steam chamber was observed to occur downwards from injector to producer initially. It was controlled mostly by pressure gradient between wells and also by thermal properties of the reservoir. Development of an equation for breakthrough time was done with the assumption that steam condensate and oil flow were a single fluid.

Reis (1992)[40] assumed the steam zone shape to be an inverted triangle in order to develop a simple analytical model for predicting recovery performance for the linear SAGD process. The inverted triangular steam zone was anchored to the producer. Steady state solution to 1-d heat conduction ahead of moving steam zone interface was applied (Carslaw and Jaeger, 1959). Due to these assumptions, solutions for the energy balance and SOR were determined.

Results were compared to experimental data presented by Butler *et al*. (1981). Little agreement between results was obtained.

During laboratory experiments, Butler (1994)[8] observed that the steam chamber does not grow as a flat front, but as a series of individual ragged fingers. He explained the existence of this effect by instability, created by the high difference in densities of rising steam and reservoir oil. Butler proposed his steam fingering theory in 1987[5]. The main points of this theory include:

- Steam flows upward from the lower boundary, providing heat to rise reservoir temperature to steam temperature.
- Heated material is leaving through the lower boundary as a number of identified streams.
- Residual oil leaves the system with velocity equal to that of the steam chamber rise.
- Flowing hot oil and condensate leave at higher velocities because they have a downward velocity relative to the hot rock and residual oil.
- The entering steam moves at higher velocity than the chamber in order to pass through the lower boundary.
- At the very top of the steam chamber steam fingers move into the relatively cold reservoir, heating the cold oil by conduction.

Ito and Ipek (2005)[28] discussed the steam fingering phenomenon in application to field data. They concluded that steam fingering plays an important role in the rise of the steam chamber and that a high pressure operation is important for activating steam fingers.

Though SAGD theory looks quite simple at the first glance, some authors have investigated pitfalls related this mechanism. Farouq-Ali (1997)[18] had some concerns on the theoretical SAGD model. He highlighted important notes regarding SAGD assumptions, such as usage of single fluid flow, constant pressure in steam chamber, only steam flowing in steam chamber and residual oil saturation in the chamber and heat transfer ahead of steam chamber to cold oil is by conduction only.

2.2 Numerical Modelling for SAGD[12]

2.2.1 Sink/Source Model

In a sink/source (SS) model, flow from/to a reservoir is presented by a single term in the reservoir flow equation. Steady state is assumed in the wellbore, i.e. there is no wellbore storativity. Only one equation per completion (layer) is solved with a bottom hole pressure as a primary variable. That means only the pressure distribution due to gravity is known in the wellbore, but not the composition and temperature. Heat conduction between the wellbore and the reservoir is also neglected. Fluid flow from/to the reservoir is calculated from **Equation (2-18)**:

$$q_j = WI\lambda_M \ p_w - p_{ij} \quad j = w, o, g. \quad\quad \textbf{(Eq. 2-18)}$$

WI is a well index that describes the geometry of a specified wellbore. It may be calculated based on the Peaceman model and also takes into account the reservoir heterogeneity. λ_M represents a fluid mobility and has a different meaning for injector and producer. When fluid is injected, λ would be the total mobility of a grid block. When fluid is produced λ would be the mobility of each phase produced from the grid block.

A simpler Sink/Source well model may be adequate:

- For reservoirs with reasonable injectivity where the effect of heat conduction between a wellbore and a reservoir is negligible. Injectivity is very low in heavy oil or tar sands reservoirs without bottom water. Therefore oil may initially be mobilized only by heat conduction, which is not possible with a Sink/Source model.
- For processes with small flow rate or big pipe diameters where frictional pressure drop is almost nonexistent.
- For short horizontal wells with a possibility of homogeneous fluid along a wellbore.
- For homogeneous reservoirs where wellbore-reservoir communication is uniform.
- For vertical wells where fluid segregation is minimal.
- For reservoirs which have much higher draw-down than the expected friction pressure drop. One has to keep in mind that the absolute value of the frictional pressure drop is not as important as is the ratio of frictional pressure drop in the wellbore and pressure drop in the reservoir. It means that low frictional pressure drop may affect results when SAGD is used in very permeable and thin reservoirs, but may not have a significant effect on thicker reservoirs with lower permeability.

For any other case the DW Model should be used.

2.2.2 Discretized Wellbore Model

The discretized wellbore (DW) model is a fully coupled mechanistic wellbore model. It models fluid and heat flow in the wellbore and between a wellbore and a reservoir/overburden. Wellbore mass and energy conservation equations are solved together with reservoir equations for each wellbore section (perforation).

To be able to solve the wellbore and reservoir equations together, some steps have to be taken to translate the pipe flow equations into Darcy's law equations. Darcy's law equations are used in reservoir simulation for flow in porous media. This means that properties such as porosity, permeability, etc. must be assigned to the wellbore. For example, permeability may be evaluated by equating pipe flow and porous media velocity: The velocity equation in porous media in x- direction is given by:

$$v = -\frac{kk_r}{\mu}\frac{\partial\phi}{\partial x}$$

(Eq. 2-19)

where:

k : permeability

k_r : relative permeability

$\dfrac{\partial\phi}{\partial x}$: potential gradient

μ : oil viscosity

Velocity equation for homogeneous flow in a pipe is:

$$v^2 = \frac{r_w}{f\rho}\frac{\partial\phi}{\partial x}$$

(Eq. 2-20)

where:

r_w : wellbore radius

f : Fanning friction factor

ρ : mass density

Assuming that the relative permeability curves in a pipe are straight lines going from zero to one, $k_r = 1$ for a homogenous fluid and k_r equals saturation for multiphase flow. For laminar flow $f = 16/\mathrm{Re}$ and

$$\mathrm{Re} = \frac{2v\rho r_w}{\mu}$$

(Eq. 2-21)

Substituting these values into **Equation (2-20)** gives permeability in a laminar mode as

$$\frac{r_w^2}{8}$$

(Eq. 2-22)

The permeability expression for turbulent flow is more complex and depends on the friction factor, fluid viscosity and density. Permeability for turbulent flow is deduced from **Equations (2-19)** and **(2-20)**:

$$k = \mu\left[\frac{r_w}{f\rho}\frac{\partial x}{\partial\phi}\right]^{1/2}\frac{\partial\phi}{\partial x}$$

(Eq. 2-23)

Permeability is updated at each time step and its value depends on the flow pattern and fluid composition. Potential gradient $\dfrac{\partial\phi}{\partial x}$ is the sum of frictional, gravity and viscous forces.

Injection or production with respect to heavy oil or tar sands reservoirs may be strongly affected by wellbore hydraulics when the driving forces in the reservoir has magnitude similar to the magnitude of the frictional forces in the wellbore. Therefore, one of the major functions of a DW model is describing reasonably well the frictional pressure drop in a wellbore.

Friction factor for turbulent, single-phase flow is calculated from Colebrook's equation as:

$$\frac{1}{\sqrt{f}} = 4\ln\frac{1}{2\varepsilon} + 3.48 - 4\ln\left[1 + \frac{9.35}{2\varepsilon\operatorname{Re}\sqrt{f}}\right]$$ **(Eq. 2-24)**

where:

ε : relative roughness.

When two phase fluid (liquid-gas) is present in the wellbore, liquid hold-up must also be considered in the friction pressure drop calculation. Liquid hold-up represents a slip between gas and liquid phase. Its magnitude depends on the flow regime, i.e. the amount of each phase present as well as phase velocities. Liquid hold-up R_g is deduced from Bankoff's correlation:

$$\frac{1}{Y} = 1 - \frac{\rho_l}{\rho_g}\left[1 - \frac{K}{R_g}\right]$$ **(Eq. 2-25)**

The correlation parameter K is a function of Reynolds number, Froude number and a flowing mass void fraction Y. K may attain values from 0.185 to one. Gas phase mobility is altered to account for the difference in liquid and gas phase velocities, i.e. gas relative permeability is augmented by the ratio of gas saturation and void fraction R_g. This operation relates the liquid hold-up calculated from pipe flow equations to saturation needed in flow equations in porous media.

Wellbore hydraulics may be used in wells with co-current upward or horizontal flow due to the chosen correlation for the liquid hold-up. In dual stream wells, flow through tubing and annulus must be considered. Tubing flow is handled similarly to wellbore flow. For laminar flow the annulus permeability is calculated as:

$$k_a = \frac{1}{8}\left[r_a^2 + r_t^2\frac{r_a^2 - r_t^2}{\ln\frac{r_a}{r_t}}\right]$$ **(Eq. 2-26)**

where:

r_a : annulus radius

r_t : tubing radius.

Velocity and permeability for turbulent flow is calculated with the proper hydraulic diameter for annulus. The same correlations as mentioned above are used to calculate the friction pressure drop and slip between gas and liquid phase. Correct area and hydraulic diameter is applied wherever necessary.

Only conductive heat transfer is allowed between tubing and annulus along the tubing length. Fluid is allowed to flow to the annulus at the end of the tubing. The same equations as mentioned above are used, but the equivalent drainage radius is calculated as

$$r_T = r_t \exp\left[\frac{\alpha^2}{\alpha^2 - 1}\ln\alpha - \frac{1}{2}\right]$$
(Eq. 2-27)

where:

$$\alpha = \frac{r_a}{r_t}$$

Fluid and energy flow between a wellbore section and a reservoir grid block is handled the same way as between individual reservoir grid blocks. Peaceman's equation is used to calculate transmissibilities (well indices) between wellbore sections and the reservoir.

$$T_j = \frac{2\pi\Delta x \bar{k}}{\ln\dfrac{r_o}{r_k}}\left(\frac{k_{rj}}{\mu_j r_j}\right)$$
(Eq. 2-28)

where:

r_k : wellbore or annulus radius

$k = \sqrt{k_x k_y}$

The equivalent drainage radius r is obtained from

$$r_o = 0.28 \frac{\left[\left(k_z/k_y\right)^{1/2}\Delta y^2 + \left(k_y/k_z\right)^{1/2}\Delta z^2\right]^{1/2}}{\left(k_z/k_y\right)^{1/4} + \left(k_y/k_z\right)^{1/4}}$$
(Eq. 2-29)

The flow energy term consists of convective and conductive flow. Convective heat transfer uses the same phase transmissibilities T_j as the component flow equations. Conductive transmissibility is expressed as:

$$K_o = \frac{2\pi x \kappa}{\ln\dfrac{r_T}{r_k}}$$
(Eq. 2-30)

with equivalent drainage radius

$$r_T = 0.14\sqrt{\Delta y^2 + \Delta z^2}$$

The inflow and outflow of fluid through each perforation change properties in each wellbore section because all wellbore conservation equations are solved implicitly. Therefore, the DW model is able to correctly handle backflow (crossflow) between reservoir and wellbore.

The initial conditions in the wellbore will determine the short behavior of a reservoir in the vicinity of a well and dictate the length of a transient state. When initial pressure, temperature and composition differ considerably from conditions at which fluid is injected or produced, the period of transient behavior may be extended to several days. Simulation of the transient behavior does not affect long term physical results for most of the processes used in EOR simulation. However, transients may be important in cyclic processes where the cycle duration is on the same order of magnitude as the transient period. The transient period is generally longer for injectors. It will increase when low mobility fluid is injected or when low mobility fluid is originally in the wellbore. Simulation of wellbore transients is necessary in well test analysis.

The effect of wellbore transients on numerical performance is larger in heavy oils or bitumen reservoirs than in conventional oil reservoirs due to very low oil mobility. It also seems to be more pronounced in injectors than producers. In addition, attempts to simulate the transient period will change the overall numerical performance compared to the sink/source approach where pseudo-steady state is assumed. High pressure, temperature or saturation changes occur due to small wellbore volume. Even in an implicit simulator the time step size will be fairly small (10e-3 to 10e-4 days, probably smaller for high rates). For example, the worst scenario is injecting steam into a wellbore containing cold oil, which may be the case after primary production. Thus, the well type may change instantaneously, but the condition in the discretized part of the well will take time to change.

When transient behavior is not requested, STARS does automatic pseudo-steady state initialization in the discretized wellbore at the beginning of simulation and every time the operating conditions are changed. Operating conditions such as pressure, rate compositions etc. are taken into consideration during pseudo-steady state initialization.

CHAPTER III
EXPERIMENT

3 EXPERIMENT

This chapter consists of four sections. First section of this chapter gives description of experimental model 1. Second section of this chapter gives description of experimental model 2. Third section gives detailed description of numerical model used to simulated SAGD process. Fourth section provides dimensional analysis of experimental model 1and numerical model.

3.1 Description of Experimental Model 1

The experimental setup is shown in **Figure 3-1**. The setup is basically a rectangular steel box with dimensions length, width and height equal to 27×29×50 cm as shown in **Figure 3-2**. The box was filled with a mixture of oil and sand to imitate the reservoir. Dried unconsolidated sand was used for simulation of the reservoir rock. Sand was bought from "Norstone", Røyneberg, Sola kommune, Stavanger, 4052. Average size of sand grains was 0-4 mm. Heavy oil was used for the simulation of reservoir oil. The composition of oil was obtained by High Temperature Gas Chromatography and presented in **Table 3-1**.

Table 3-1: Heavy oil composition

Component	Weight%	Component	Weight%	Component	Weight %	Component	Weight %
C1-C14	<0.01	C36	1,75	C58	0,72	C80	0,29
C15	0,97	C37	1,63	C59	0,74	C81	0,38
C16	0,63	C38	1,37	C60	0,60	C82	0,37
C17	0,73	C39	1,36	C61	0,80	C83	0,42
C18	1,23	C40	1,14	C62	0,59	C84	0,31
C19	1,56	C41	1,66	C63	0,73	C85	0,46
C20	2,21	C42	0,64	C64	0,58	C86	0,31
C21	2,67	C43	1,11	C65	0,60	C87	0,31
C22	3,15	C44	0,91	C66	0,60	C88	0,30
C23	2,99	C45	1,01	C67	0,58	C89	0,44
C24	3,11	C46	0,90	C68	0,55	C90	0,28
C25	3,86	C47	0,91	C69	0,52	C91	0,29
C26	3,39	C48	0,91	C70	0,50	C92	0,28
C27	4,00	C49	0,90	C71	0,50	C93	0,29
C28	3,50	C50	0,72	C72	0,50	C94	0,29
C29	4,00	C51	0,83	C73	0,48	C95	0,28
C30	3,50	C52	0,67	C74	0,31	C96	0,29
C31	3,50	C53	0,83	C75	0,46	C97	0,28
C32	2,50	C54	0,86	C76	0,43	C98	0,29
C33	2,64	C55	0,74	C77	0,43	C99	0,26
C34	2,00	C56	0,80	C78	0,45	C100+	4,81
C35	2,11	C57	0,74	C79	0,46		

Distilled water was used for steam generation. Chemicals IKM LB-456 N are added in the water as inhibiting additives for the steam generator to avoid corrosion. Chemicals IKM LB-456 N are supplied by Industrikemikalier AS Mitco, Norway (Industrikjemikalier AS Mitco 2008)[27].
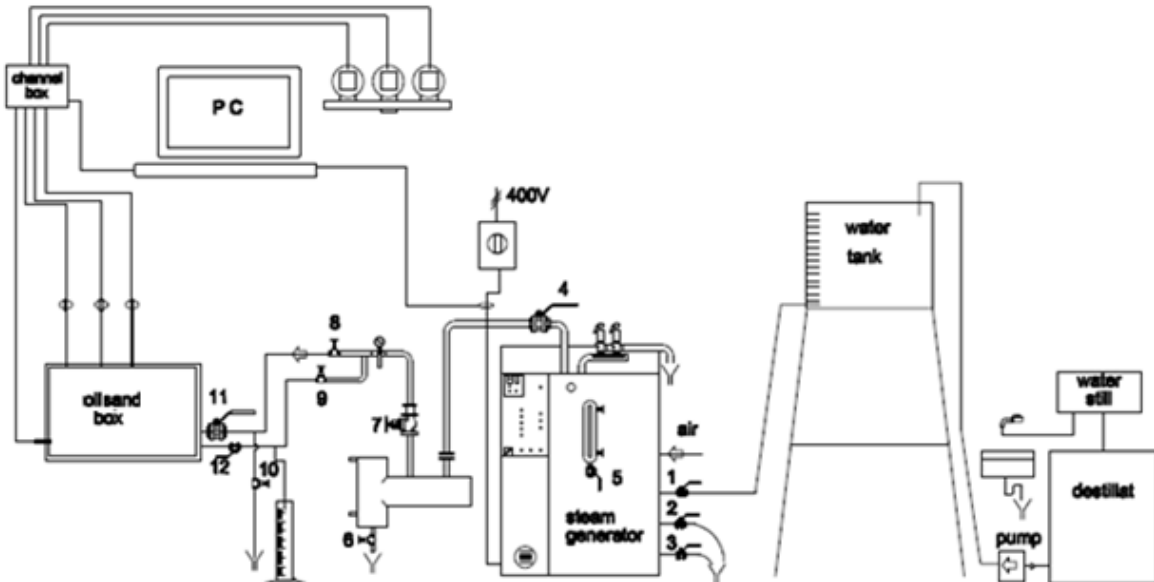
1 – Water power generator valve	7 – Control valve (open/close)
2 – Discharge valve for vapor from steam generator	8 – Steam flow rate control valve
3 – Discharge valve for water from steam generator	9 – Bypass valve to heat tubing
4 – Outlet valve from steam generator to oil sand box	10 – Bypass valve to discharge steam
5 – Valve, indicating water level in steam generator	11 – Injection well inlet valve
6 – Valve to remove condensate	12 – Production valve

Figure 3-1: Experimental setup

Figure 3-2: Oil sand model 1 reservoir setup
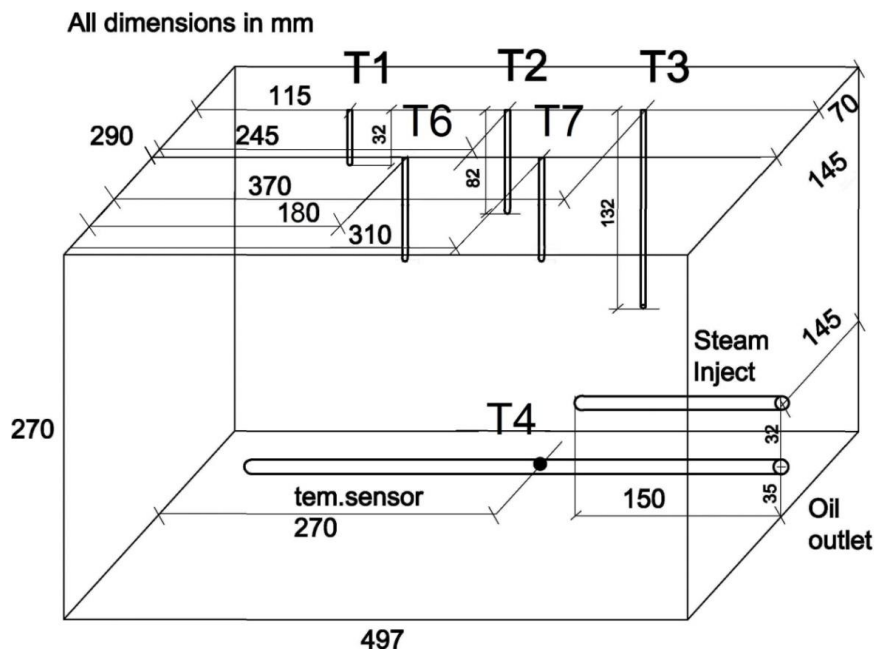
Temperature sensors are inserted from the top of the box. These are designed with a flexibility build in, in order to be able to change the depth. Two wells are placed horizontally from a side of the box simulating the actual SAGD wells' construction. The side where the wells are inserted has the advantage that it is possible to use the whole length of the simulated reservoir (box) as a symmetrical half of the reservoir. The production well is located 3.5 cm above the bottom of the box; the distance between production and injection well is about 3 cm. The model reservoir is filled with an oil sand mixture and has a height of about 11 cm giving a total volume of oil-sand of about 16 liters. To prepare this mixture, 15.4 liters of sand and 6.5 liters of oil were used. Oil sand in the box is distributed as uniformly as possible to minimize the heterogeneity in this reservoir model with same thickness. A teflon plate is installed above the oil sand and serves as an impermeable overburden. After the above initial preparation is done, the box is closed by a steel lid with silicon gasket. The lid has holes to be able to insert the sensors (sensors 1, 2, 3, 6 and 7) as shown in **Figure 3-2**; sensors could be placed at different depths. Sensors have been put in right order and fixed at a certain height (determined depth of sensors in oil sand for experiment). The sensors are located in one half of the box, because it was assumed that steam propagates symmetrically in the oil sand reservoir. Sensor 7 and 6 are located on the central line of the box, the same as production and injection wells. Sensor 7 is closer to the wells, sensor 6 is more remote. Sensor 1, 2, and 3 are located on the parallel line which is displaced 7.5 cm from the central line. Sensors 1, 2 and 3 are placed in such way that they create staggered order with sensors 7 and 6. The oil sand box is equipped with a ventilation system. In the lid of the box there is a pipe removing steam and CO_2, which break through the overburden due to imperfect isolation. The pipe is located opposite to the injection well.

A steam generator is used to produce steam for injection in the oil sand. Generator HT 48 STEAMBOX AS is used. Specification of the steam generator is given in the **Table 3-2**. The steam generator is connected to a distilled water tank which is connected to the steam water inlet. The water is treated with chemicals IKM LB-456 N in concentration 1ml of chemicals per 10 liters of distilled water, to adjust the pH of the water to a value between 8 and 10. This treatment is necessary to avoid or reduce corrosion of equipment in the steam generator.

Table 3-2: Steam generator specification

Parameter	Value
Model	HT 36/48 STEAMBOX AS
Maximum pressure of produced steam	18 bar
Maximum temperature of produced steam	210 deg C
Working volume of steam generator	58 liters
Power	48 kW
Mass flow rate of steam	62 kg/hr.

The experiment starts by injecting steam into the injection tube at constant rate. Average injection rate during the experiments is 1.8 g/s of generated steam. An oil-water mixture is produced from the production tube. The production well is heated up by an electric cable to reduce precipitation of the oil in the outlet production tube. At start up the steam is drained to

heat up the injection tube to a predetermined temperature (≈103 °C) monitored by sensor 5 and displayed on the monitor of the computer using "Labview 7.1 National Instrument", March 2004 edition. After the injection system and production tubes are heated up, experiments start by opening the valves leading to the inside of the simulated reservoir (into the box). Pressure of steam in the outlet of the steam generator is around 5 bars. During experiments, temperature of steam measured by sensor 5 is around 103 deg C. Estimated pressure of steam entering the oil sand reservoir equals atmospheric pressure by correlating steam temperature in **Table 3-3**. At the start, the condensed steam is firstly produced. Then the mixture of oil-water follows after approximately 1-2 min. The produced fluids are collected in measuring cylinders.

Table 3-3: Properties of saturated steam (Source: www.EngineeringToolbox.com)[46]

Absolute pressure	Boiling point	Specific volume (steam)	Density (steam)	Specific enthalpy of liquid water (sensible heat)		Specific enthalpy of steam (total heat)		Specific heat
(bar)	(°C)	(m3/kg)	(kg/m3)	(kJ/kg)	(kcal/kg)	(kJ/kg)	(kcal/kg)	(kJ/kg)
0,5	81,35	3,24	0,309	340,57	81,34	2645,99	631,98	1,9654
1	99,63	1,694	0,59	417,51	99,72	2675,43	639,02	2,0267
1,5	111,37	1,159	0,863	467,13	111,57	2693,36	643,3	2,0768
2,0	120,23	0,885	1,129	504,71	120,55	2706,29	646,39	2,1208
3,0	133,54	0,606	1,651	561,44	134,1	2724,66	650,77	2,1981
4,0	143,63	0,462	2,163	604,68	144,43	2737,63	653,87	2,2664
5,0	151,85	0,375	2,669	640,12	152,89	2747,54	656,24	2,3289
6,0	158,84	0,315	3,17	670,43	160,13	2755,46	658,13	2,3873
7,0	164,96	0,273	3,667	697,07	166,49	2761,98	659,69	2,4424
8,0	170,42	0,24	4,162	720,94	172,19	2767,46	661	2,4951
9,0	175,36	0,215	4,655	742,64	177,38	2772,13	662,11	2,5456
10,0	179,88	0,194	5,147	762,6	182,14	2776,16	663,07	2,5944
11,0	184,06	0,177	5,638	781,11	186,57	2779,66	663,91	2,6418
12,0	187,96	0,163	6,127	798,42	190,7	2782,73	664,64	2,6878
13,0	191,6	0,151	6,617	814,68	194,58	2785,42	665,29	2,7327
14,0	195,04	0,141	7,106	830,05	198,26	2787,79	665,85	2,7767
15,0	198,28	0,132	7,596	844,64	201,74	2789,88	666,35	2,8197
16,0	201,37	0,124	8,085	858,54	205,06	2791,73	666,79	2,8620
17,0	204,3	0,117	8,575	871,82	208,23	2793,37	667,18	2,9036
18,0	207,11	0,11	9,065	884,55	211,27	2794,81	667,53	2,9445
19,0	209,79	0,105	9,556	896,78	214,19	2796,09	667,83	2,9849
20,0	212,37	0,1	10,047	908,56	217,01	2797,21	668,1	3,0248
25,0	223,94	0,08	12,515	961,93	229,75	2800,91	668,99	3,2187
30,0	233,84	0,067	15,009	1008,3	240,84	2802,27	669,31	3,4069

After finishing the experiment, the collected fluids are separated, water discharged and oil returned to the box and remixed with the sand. Oil sand is mixed uniformly and cooled till next experiment. This is done to assure same quantity of oil at the start of the following experiment. However, this is done under the assumption that there is no loss of oil during the

production, which is a reasonable assumption when the minimum loss lies within the experimental uncertainty (20-30 ml).

3.2 Description of Experimental Model 2

During work with the master thesis, a new experimental installation was developed. It had a purpose to have better options for the quantitative analysis of the experimental data. During experimental runs with new installation some challenges were met, which are yet to be solved. Therefore, the results of the experiments in the model 2 are presented in qualitative manner only.

The photo of experimental model 2 is shown on **Figure 3-3**. Experimental model 2 has different oil sand model reservoir setup. The rest of experimental facility is the same, as shown in **Figure 3-1**. Model 2 reservoir has cylindrical shape, diameter equals 32.2 cm, width equal 10 cm. Injection and production wells are inserted at the bottom of the model, as shown in **Figure 3-4.**
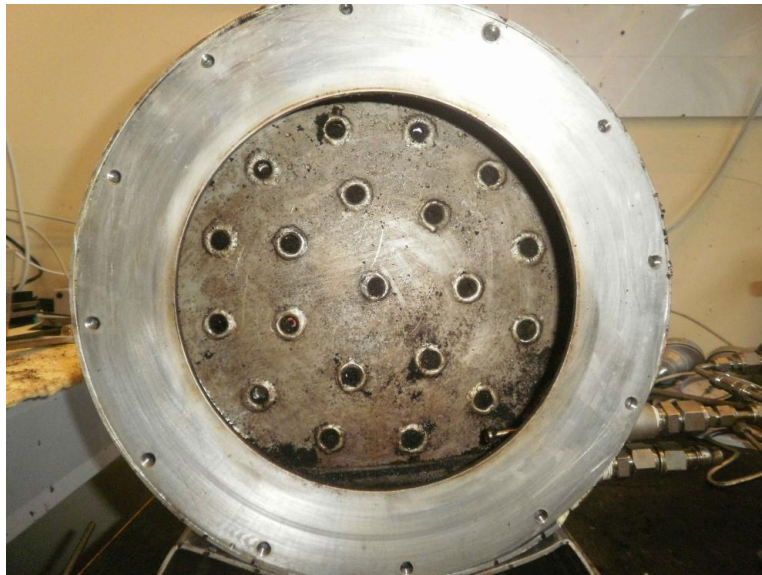
Figure 3-3: Oil sand model 2, common view

The model 2 reservoir filled with a similar mixture of the oil and sand as in the experimental model 1. For the mixture were used 7 liters of the sand and 2.1 liters of the oil. The oil sand in the model was distributed uniformly, as it possible within experimental uncertainty. The front side of the experimental setup is closed by steel lid with the glass after filling the setup with the oil sand mixture. The temperature sensors are inserted from the back side of cylindrical model. Distances from the injector point to the sensors are shown in **Figure 3-4**. Sensors have been put in the same order for all experiments, and have the same depth of 5cm, which equals to the middle of reservoir width, and in the same vertical plane of injection and production wells. The installation setup is constructed in the way that it might operate under pressure up to 6 bars.

Figure 3-4: Oil sand model 2, schematic setup

Procedure of experiments in the model 2 is similar to procedures of the previous model 1. The steam injected under pressure in the model reservoir through 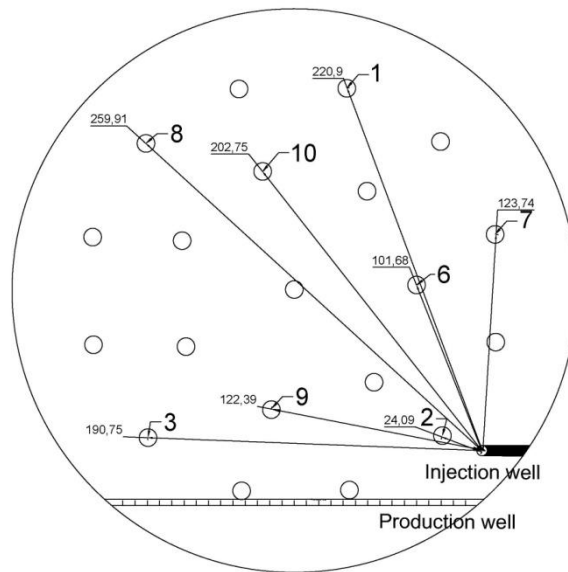the injector, and oil-water mixture is produced from the production well. Both injection and production lines equipped with the pressure gauges, which make possible to observe the pressure changes in the model reservoir during experiments. After finishing of the experiment, produced oil returned to the oil sand mixture, remixed and used in following experiment. Experimental history in model 2 has two sets, with 4 experiments in each. First experiment in each set has fresh oil sand mixture with zero water saturation. Following after first experiment have certain water saturation due to steam injection and limitations of complete removing of water from the oil sand mixture.

3.3 Description of Numerical Model

To generate the numerical model, the simulator STARS version 2009 was used. STARS is CMG's new generation advanced processes reservoir simulator and includes options such as chemical/polymer flooding, thermal applications, steam injection, horizontal wells, dual porosity/permeability, directional permeabilities, flexible grids, fireflood, and many more. STARS was developed to simulate steam flood, steam cycling, steam-with-additives, dry and wet combustion along with many types of chemical additive processes, using a wide range of grid and porosity models in both field and laboratory scale. (CMG STARS)[12]

WinProp was used to build the PVT compositional model. WinProp is CMG's equation of state (EOS) multiphase equilibrium and properties determination program. WinProp features techniques for characterizing the heavy end of a petroleum fluid, lumping of components, matching laboratory PVT data through regression, simulation of first and multiple contact

miscibility, phase diagrams generation, asphaltene and wax precipitation modelling, compositional grading calculations as well as process flow simulation. (CMG WinProp)[13]

3.3.1 Overview of the Model

The reservoir model is pseudo 3D; it contains only 2 grid blocks along the horizontal section. The numerical grid of 2D cross section in i-k plane is the main concern for observation and evaluation of most parameters. The model was built to simulate typical SAGD process. Dimensional analysis was performed to scale it to experimental model 1. Dimensionless number B_3 (Butler, 1991)[9] is used for scaling analysis. It was decided to use a compositional model of experimental oil, which was built using WinProp version 2009 with fluid data obtained after lab analysis of oil and PVTSim generated data. Rock-fluid and permeability data are based on studies done by Priyadi Y. [Thermal Recovery of Heavy oil by SAGD, 2009][39].

3.3.2   Gridding System

The Cartesian grid model has dimensions 40×2×25. Total amount of blocks is 2000. The model has length 500 meters, 40 m width spacing, and measures 25 meters in thickness. The 3D model is shown in **Figure 3-6**. The model reservoir is homogenous with single porosity equal to 34%, horizontal permeability (k_i=k_j) equal to 1.8 D, and vertical permeability equal to the horizontal permeability (homogeneous reservoir). Irreducible water saturation is 20%, and initial oil saturation is 80%. Initial oil in place is 136000 m^3 for the half element of symmetry. Initial reservoir pressure equals 800 kPa, and temperature equals 21 deg C. The density and viscosity of the oil is approximately 987 kg/m^3 and 92600 cp respectively. Top of reservoir is situated 300 m below surface. The production well is situated at the bottom of the reservoir. Well spacing between injector and producer is 5 meters. Simulation starts in 2008-01-01 and finishes 2019-12-31. Temperature propagation is shown for several dates in **Figure 3-5**.
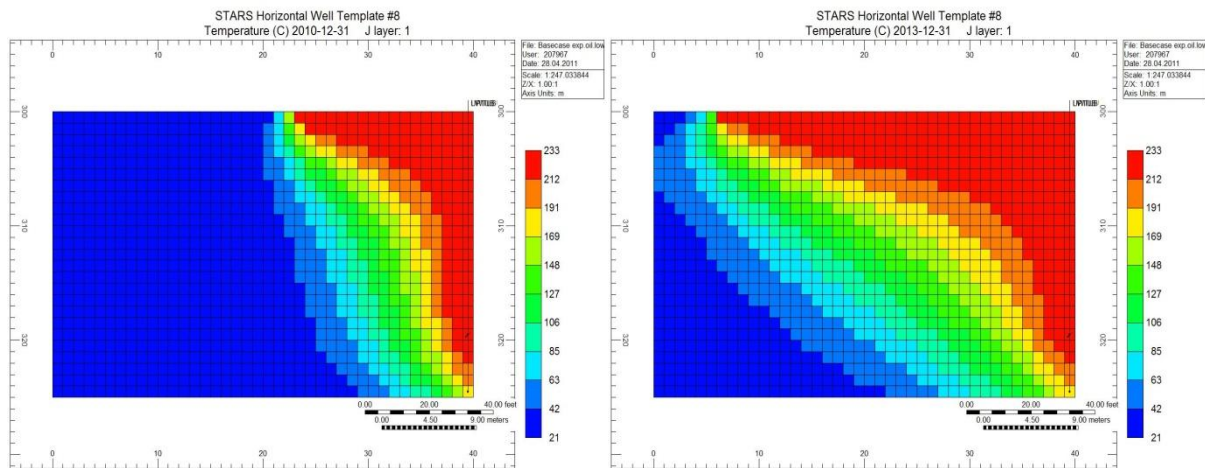

Figure 3-5: Temperature profile for base case model after 3 and 6 years respectively
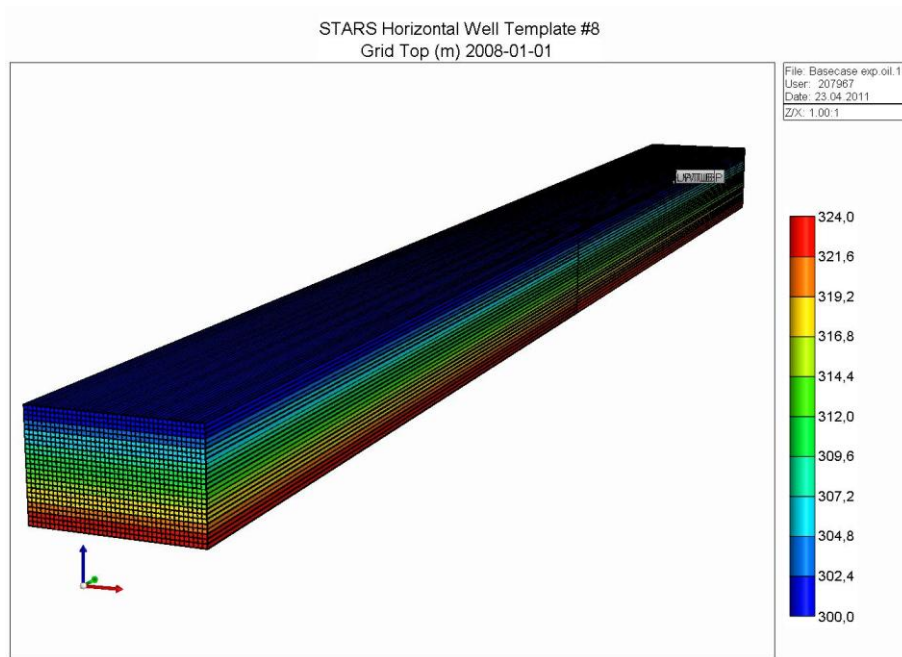
Figure 3-6: 3D Grid model view

3.3.3 Physical Fluid Properties

During this thesis the compositional model is used. WinProp is used to generate a PVT fluid model for the thermal simulator CMG's STARS. The WinProp generated data includes:

- Initial global compositional data;

- Liquid component densities, compressibility and thermal expansion coefficients;

- Liquid phase viscosity tables;

- Gas-liquid K-values.

Gas-liquid K-value tables (CMG WinProp)[13]

The Gas-Liquid K-Value Table option is used to generate gas-liquid K-values for hydrocarbon components and optionally for a water component as well. Hydrocarbon and light gas components are all assumed to be oleic. That is, the K-value is defined as the gas phase mole fraction of the component divided by the oil phase mole fraction of the component. If water is present as a component in the system, it is defined as an aqueous component, and the gas-liquid K-value is defined as the gas phase mole fraction of water divided by the aqueous phase mole fraction of water. In this case, the aqueous phase mole fraction of water is assumed to be equal to one. K-values are calculated using a two-phase negative flash which allows generation of K-values outside of the two-phase region. There are limits in pressure and temperature beyond which the negative flash will be unable to converge. These limits normally lie quite far from the two-phase boundary, except near the critical point of the mixture. K-values which lie outside the range of convergence of the

negative flash are estimated by linear extrapolation. Values which have been extrapolated are marked in the tables with the notation "<extrap.>".

Limits for generating K-values in the compositional model for this thesis lie in the temperature range of 0-380 deg C and pressure range of 10-3810 kPa. Water properties are not included in the generation in WinProp, but CMG STARS default values are used.

Cubic Equation of State (EOS)

In this thesis Peng Robinson (1978) EOS was used.

$$p = \frac{RT}{v-b} - \frac{a}{v^2 + vb - b^2}$$ (Eq. 3-1)

where:

R : universal gas constant

v : molar volume

$$a = a_c \alpha$$ (Eq. 3-2)

$$a_c = \Omega_a \frac{(RT_c)^2}{p_c}$$ (Eq. 3-3)

$$b = \Omega_b \frac{RT_c}{p_c}.$$ (Eq. 3-4)

For Peng Robinson, EOS coefficients Ω_a and Ω_b equal 0.45724 and 0.0778 respectively.

Parameter α defined by:

$$\alpha = \left\{ 1 + m \left[1 - \sqrt{\frac{T}{T_c}} \right] \right\}^2$$ (Eq. 3-5)

where:

$$m = 0.37464 + 1.54226\omega - 0.26992\omega^2$$ (Eq. 3-6)

ω : acentric factor.

Modification for hydrocarbons heavier than n-decane (PR 1978):

$$m = 0.379642 + 1.48503\omega - 0.164423\omega^2 + 0.016666\omega^3$$ (Eq. 3-7)

The compressibility factor $Z = pv/RT$ can be expressed as:

$$Z^3 + (B-1)Z^2 + (A - 3B^2 - 2B)Z - (AB - B^2 - B^3) = 0$$ (Eq. 3-8)

where:

$$A = \frac{ap}{(RT)^2}$$ (Eq. 3-9)

$$B = \frac{bp}{RT}$$ (Eq. 3-10)

For mixtures, the parameters a and b are defined using the following mixing rule:

$$a = \sum_i x_i S_i$$ (Eq. 3-11)

$$S_i = \sqrt{a_i} \sum_j x_j (1 - d_{ij}) \sqrt{a_j}$$ (Eq. 3-12)

$$b = \sum_i x_i b_i$$ (Eq. 3-13)

where:

d_{ij} : empirically determined interaction coefficient.

Compositional data

Oil composition is obtained by lab analysis and presented as component weight percent, given in **Table 3-1**. The lumping procedure in the WinProp simulator was used to convert all real oil components into a few numbers of pseudo-components. Prats (1986)[38] recommended that it is necessary to have minimum four pseudo-components to accurately simulate thermal processes and recovery mechanisms in the steamflooding of heavy oil. In this thesis experimental oil composition is lumped into three pseudo-components, and one water component is used. Generated oil component properties are given in **Table 3-4**.

Table 3-4: Component properties table

Components	Mole fraction	Critical pressure, (kPa)	Critical temperature, (deg C)	Molecular weight, (kg/gmole)
C15 - C20	0.0733	1581.42	541.1	0.2509
C21 - C45	0.595	673.27	546.66	0.3929
C46 - C70	0.3317	268.07	1016.47	0.8305

Physical fluid properties such as density, fluid critical properties, compressibility, enthalpy and viscosity are generated in WinProp as well, and shown in **Table 3-5**.

Table 3-5: Physical fluid properties table

Components/Properties	Units	C15 - C20	C21 - C45	C46 - C70
Mass density	kg/m^3	813.92	897.384	1095.43
Liquid compressibility	1/kPa	1.467e-006	1.399e-006	1.146e-006
1st Thermal expansion coefficient	1/C	0.0005007	0.0005369	0.0004711
2nd Thermal expansion coefficient	1/(C*C)	1.398e-006	9.236e-007	2.806e-007
Pressure-temperature cross term for density	1/(kPa*C)	2.332e-007	2.788e-009	1.319e-009

Liquid densities are obtained by ideal mixing of pure-component densities with phase composition

$$\frac{1}{\rho_w} = \sum_{i=1}^{n_c} \frac{w_i}{\rho_{wi}}$$ **(Eq. 3-14)**

$$\frac{1}{\rho_o} = \sum_{i=1}^{n_c} \frac{x_i}{\rho_{oi}}$$ **(Eq. 3-15)**

Densities ρ_w and ρ_o are inverses of phase molar volumes. Component densities ρ_{wi} and ρ_{oi} are inverses of the corresponding partial molar volume and should be regarded as the pure component contribution to the phase volume. (CMG STARS)[12]
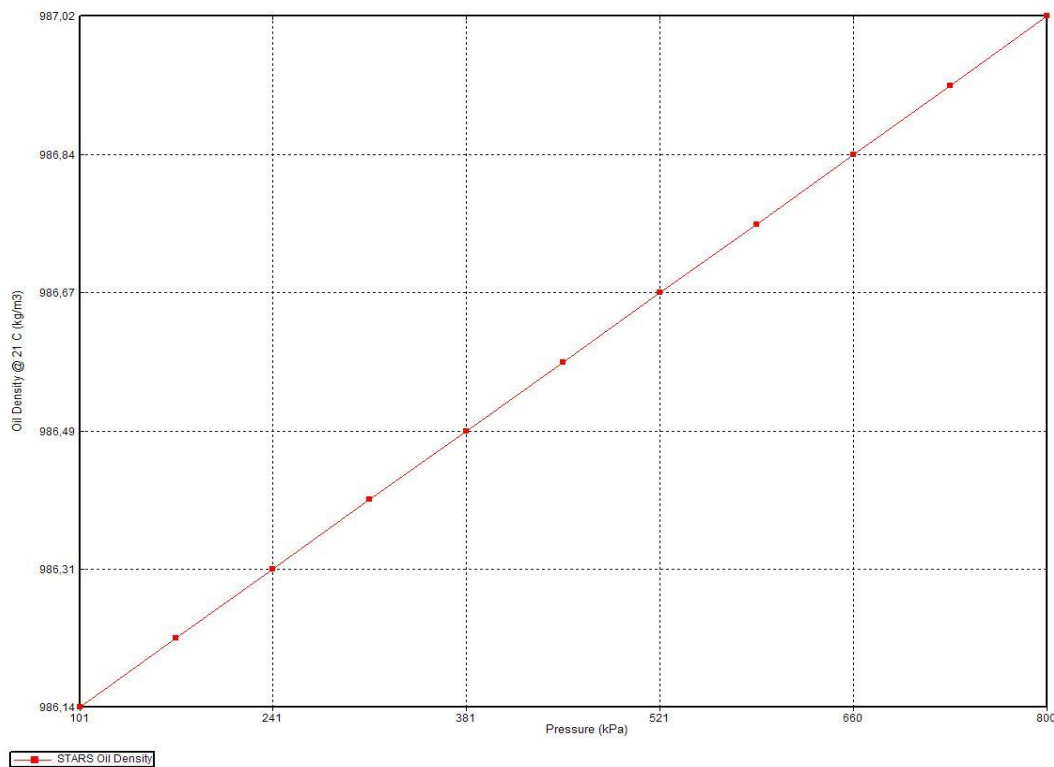

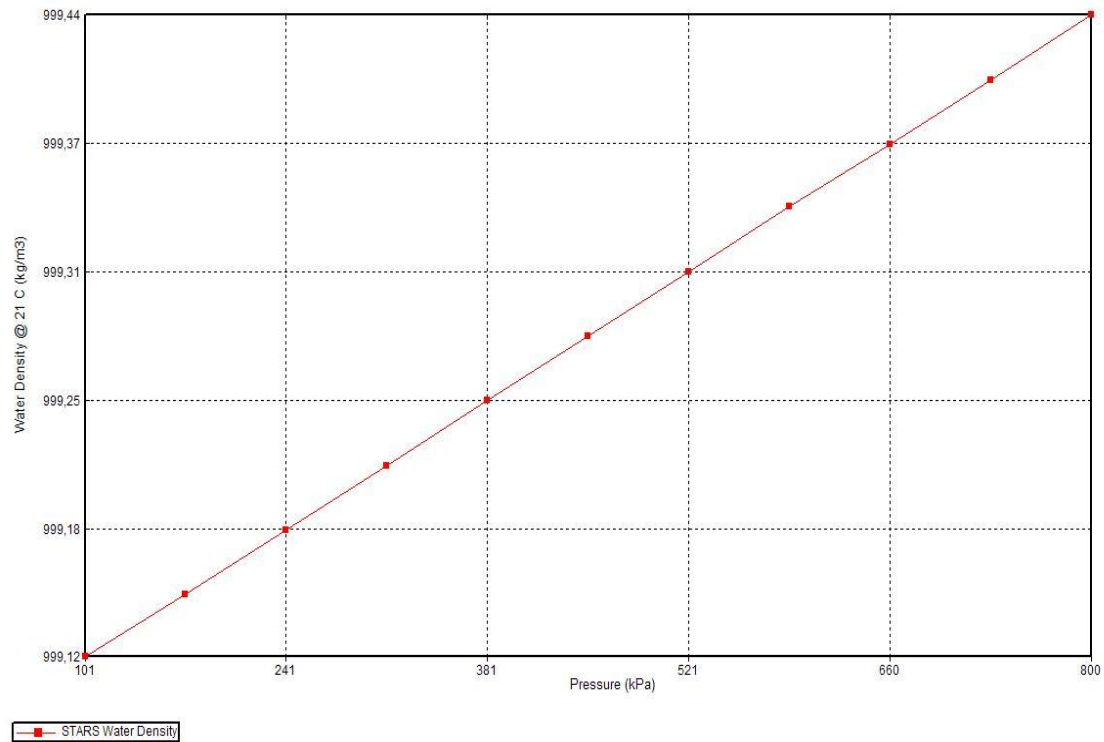**Figure 3-7: Oil density vs pressure at 21 deg C**

Figure 3-8: Water density vs pressure at 21 deg C

3.3.4 Oil Viscosity Model

Generation of oil viscosity is based on the compositional model of oil. Tables of viscosity dependence on pressure and temperature are generated using "PVTSim". **Table 3-6** presents the data below.

Table 3-6: Oil viscosity table

Pressure, bar	Viscosity at, deg C		
	50	100	200
	Oil Viscosity, cP		
80	33537,8984	756,16	4,492
60	32359,2324	729,585	4,334
50	31760,9297	716,096	4,254
40	31152,5234	702,378	4,172
30	30528,6602	688,312	4,089
20	29879,6367	673,679	4,002
10	29183,0605		3,908
5	28796,4063		3,857

The oil component viscosity is generated by using the modified Pedersen correlation (1987) in WinProp CMG. The fluid viscosity table shows the viscosity dependence of each pseudo-component at all the used ranges of temperature, shown in **Table 3-7**.

Table 3-7: Components liquid viscosity at different temperatures

Temperature, deg C	Liquid viscosity, cp		
	C15 - C20	C21 - C45	C46 - C70
0	11.088	46.127	5.6669e+015
21.053	4.8092	14.35	5.467e+012
42.105	2.5745	5.9562	2.4955e+010
63.158	1.6002	3.0384	3.5808e+008
84.211	1.1076	1.8009	1.2127e+007
105.263	0.82928	1.1927	789640
126.316	0.65792	0.85855	85159
147.368	0.54513	0.65858	13626
168.421	0.46685	0.53058	2979
189.474	0.41014	0.44414	836.17
210.526	0.36761	0.38313	287.27
231.579	0.33472	0.33843	116.39
252.632	0.3136	0.30417	53.951
273.684	0.2872	0.27809	28.059
294.737	0.25988	0.25869	15.92
315.789	0.24168	0.23894	9.998
336.842	0.22609	0.22162	6.7284
357.895	0.21197	0.20634	4.7916
378.947	0.19884	0.19258	3.5799
400	0.18631	0.17997	2.7862

Pedersen Viscosity model

The Pedersen viscosity correlation uses the principle of corresponding states to calculate the viscosity of a component or mixture, knowing the viscosity of a reference substance at the same conditions of reduced pressure and temperature. The deviation from simple corresponding states is accounted for by a "rotational coupling coefficient," α. The viscosity of the mixture is calculated according to **Equation 3-16**:

$$\frac{\mu_{mix}(P,T)}{\mu_o(P_o,T_o)} = \left(\frac{T_{c,mix}}{T_{c,o}}\right)^{-1/6} \left(\frac{P_{c,mix}}{P_{c,o}}\right)^{2/3} \left(\frac{MW_{mix}}{MW_o}\right)^{1/2} \left(\frac{\alpha_{mix}}{\alpha_o}\right) \qquad \textbf{(Eq. 3-16)}$$

where:

μ : viscosity

T_c : critical temperature

P_c : critical pressure

MW : molecular weight

α : rotational coupling coefficient.

The subscript "mix" refers to the mixture property, and the subscript "o" refers to the reference substance property. The reference substance for the Pedersen model is methane. The mixture critical temperature and pressure are calculated using mixing rules that are functions of the component critical temperatures and pressures and mole fractions. The molecular weight of the mixture is determined from:

$$MW_{mix} = b_1 \left(MW_w^{b_2} - MW_n^{b_2} \right) + MW_n \qquad \textbf{(Eq. 3-17)}$$

where:

MW_w : weight fraction averaged molecular weight

MW_n : mole fraction averaged molecular weight.

The rotational coupling coefficient is calculated as follows:

$$\alpha = 1 + b_3 \rho_o^{b_4} MW^{b_5} \qquad \textbf{(Eq. 3-18)}$$

where:

ρ_o : reduced density of the reference fluid.

Pedersen *et al.* used methane as the reference fluid. The authors used a BWR-equation in the form suggested by McCarty to evaluate the density of methane (after Gabitto and Barrufet, 2003)[20]. This density is evaluated at reference pressure and temperature:

$$\rho_o = \frac{\rho_o \left(\dfrac{PP_{c,o}}{P_{c,mix}}, \dfrac{TT_{c,o}}{T_{c,mix}} \right)}{\rho_{co}} \qquad \textbf{(Eq. 3-19)}$$

Pressures and temperature at which the reference viscosity is estimated:

$$P_o = \frac{PP_{c,o}}{P_{c,mix}} \frac{\alpha_o}{\alpha_{mix}} \qquad \textbf{(Eq. 3-20)}$$

$$T_o = \frac{TT_{c,o}}{T_{c,mix}} \frac{\alpha_o}{\alpha_{mix}} \qquad \textbf{(Eq. 3-21)}$$

The oil phase viscosity is obtained by a logarithmic mixing rule:

$$\ln(\mu_o) = \sum_{i=1}^{n_c} x_i \ln \left(\mu_{oi} \right) \qquad \textbf{(Eq. 3-22)}$$

The viscosity of a mixture calculated using the Pedersen model depends strongly on the critical pressures, critical temperatures and molecular weights of the components and on the coefficients b_i shown in the **Equations (3-17)** and **(3-18)**.

A plot of generated oil viscosity is shown on **Figure 3-9**. The dependence of water viscosity on temperature was taken as default values used in CMG STARS and shown on **Figure 3-10**.
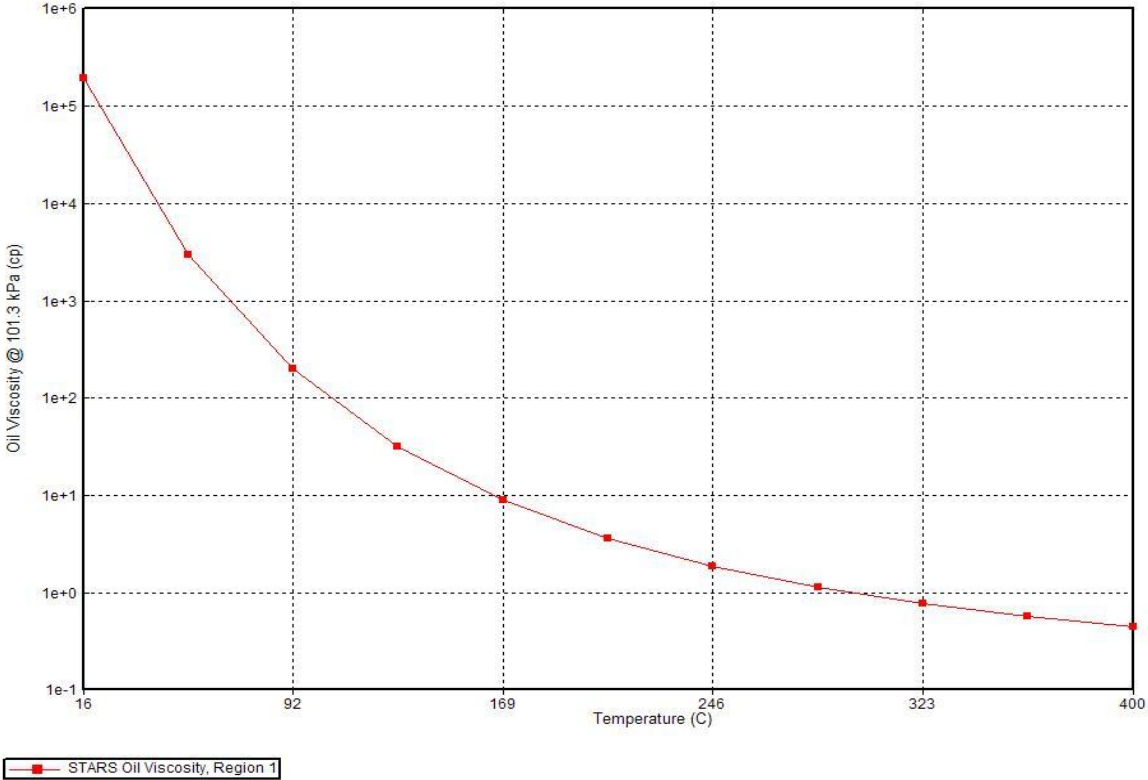

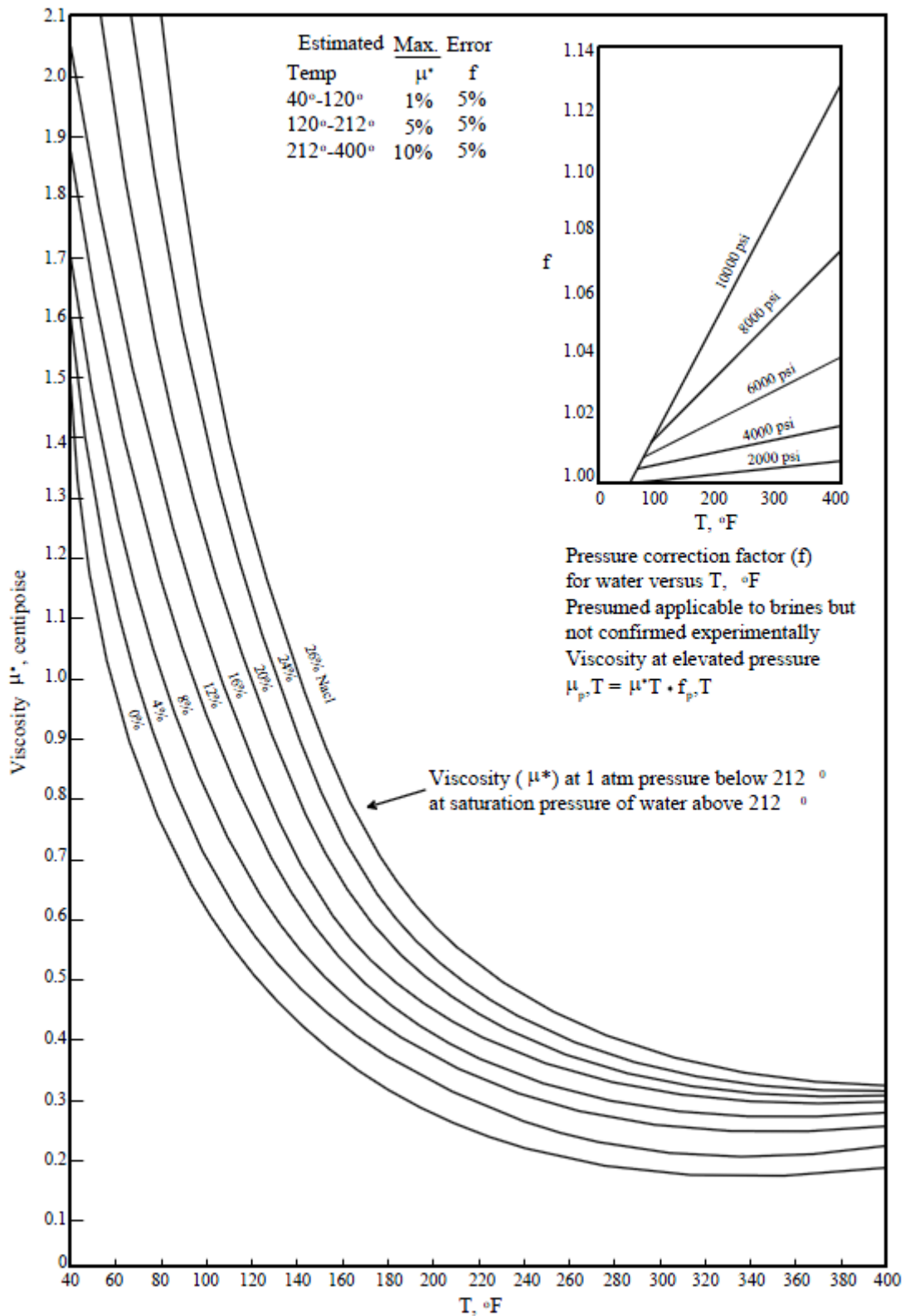**Figure 3-9: Oil viscosity vs temperature**

Figure 3-10: Water viscosity (salinity dependence) vs temperature (Source: CMG's STARS Guide)[12]

3.3.5 Rock Properties

Rock-fluid and permeability data used in the model are generated by Priyadi (2008)[39]. In general, the rock and fluid properties are based on the ADOE/AEUB Athabasca McMurray case study.

Rock type

To specify rock type properties we were need to choose wettability type and a method for Evaluating 3 phase KRO.

The following wettability type was chosen: Water Wet. This is the most commonly chosen wettability and is the default. This option assumes that the water phase is next to the rock and oil being the middle phase. The three-phase relative permeability calculation is:

a) Obtain k_{rw} and k_{row} from the Saturation water table (SWT), as a function of S_w

b) $k_{rocw} = k_{row}(S_w = S_{wc})$

c) Obtain k_{rg} and k_{rog} from the Saturation liquid table (SLT), as a function of S_g

d) $k_{ro} = k_{rocw} \cdot \left[\left(k_{row} / k_{rocw} + k_{rw} \right) \left(k_{rog} / k_{rocw} + k_{rg} \right) - k_{rw} - k_{rg} \right]$ **(Eq. 3-23)**

e) k_{rw} and k_{rg} are the same as the two-phase values.

Stone's second model was chosen as the method for evaluating 3-phase KRO. The relative permeability of water in the three-phase system is equal to the water relative permeability in the two-phase water-oil system, and is a function only of S_w. The relative permeability of gas in the three-phase system is equal to the gas relative permeability in the two- phase liquid-gas system, and is a function only of S_g. The three-phase oil relative permeability is calculated using the modification of Aziz and Settari (1979)[1]. The calculation of three-phase oil relative permeability is (liquid also contains S_{wc} as default option):

$$S_{el} = \left[\left(S_w + S_o - S_{lc} \right) \right] \left[\left(1 - S_{gc} - S_{lc} \right) \right]$$

$$S_{ew} = \left[\left(S_w - S_{wc} \right) \right] \left[\left(1 - S_{orw} - S_{wc} \right) \right]$$

$$k_{rw} = k_{rw}(S_{ew})$$

$$k_{rg} = k_{rg}(S_{el})$$

$k_{ro} = k_{rocw} \cdot \left[\left(k_{row} / k_{rocw} + k_{rw} \right) \left(k_{rog} / k_{rocw} + k_{rg} \right) - k_{rw} - k_{rg} \right]$ **(Eq. 3-24)**

where:

$k_{rocw} = k_{row}(S_w = S_{wc}) = k_{rog}(S_g = 0)$ **(Eq. 3-25)**

Permeability relative profile for Stone's second model is shown in **Figure 3-9**.
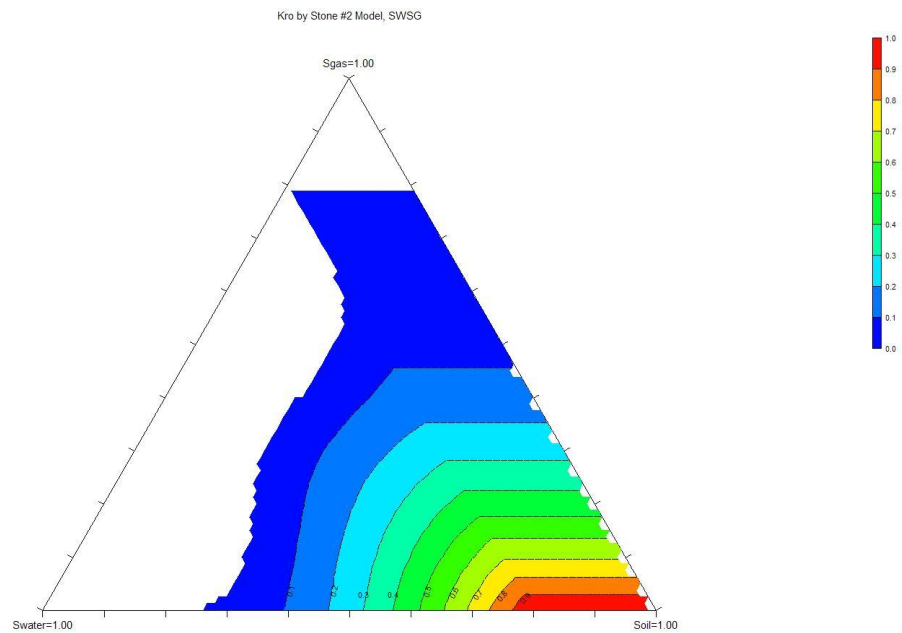

Figure 3-11: KRO by Stone's second model

Two-phase water-oil relative permeability as a function of water saturation is shown in **Table 3-8** and plotted in **Figure 3-12**. The smoothing method for table end-points is quadratic smoothing interpolation.

Table 3-8: Water-oil relative permeability table

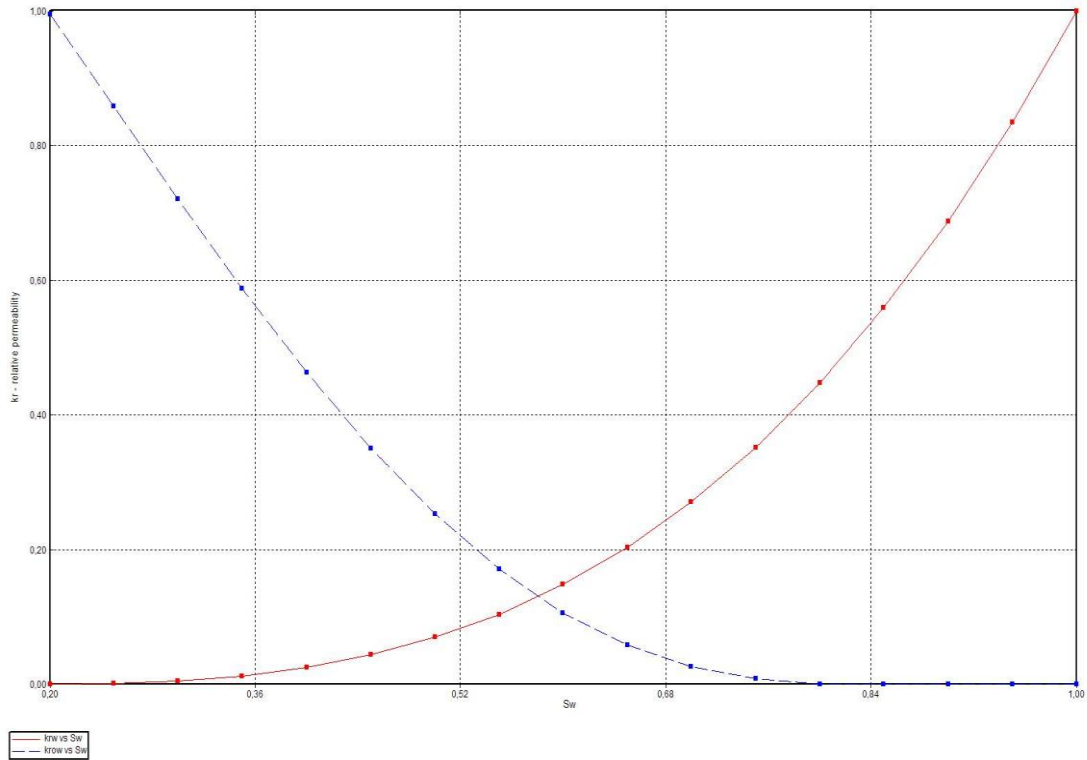| S_w	k_{rw}	k_{row}
0.2	0	0.9942
0.25	0.0014	0.8582
0.30	0.0052	0.7210
0.35	0.0129	0.588
0.4	0.0255	0.4634
0.45	0.0441	0.3509
0.5	0.0700	0.2529
0.55	0.1043	0.1713
0.6	0.1484	0.1067
0.65	0.2035	0.059
0.7	0.2708	0.0271
0.75	0.3517	0.0091
0.8	0.4473	0
0.85	0.5588	0
0.9	0.6874	0
0.95	0.8341	0
1	1	0

Figure 3-12: Water-oil relative permeability plot

Two-phase gas-oil relative permeability as a function of liquid saturation is shown in **Table 3-9** and plotted in **Figure 3-13**. The smoothing method for table end-points is quadratic smoothing interpolation.

Table 3-9: Liquid-gas relative permeability table

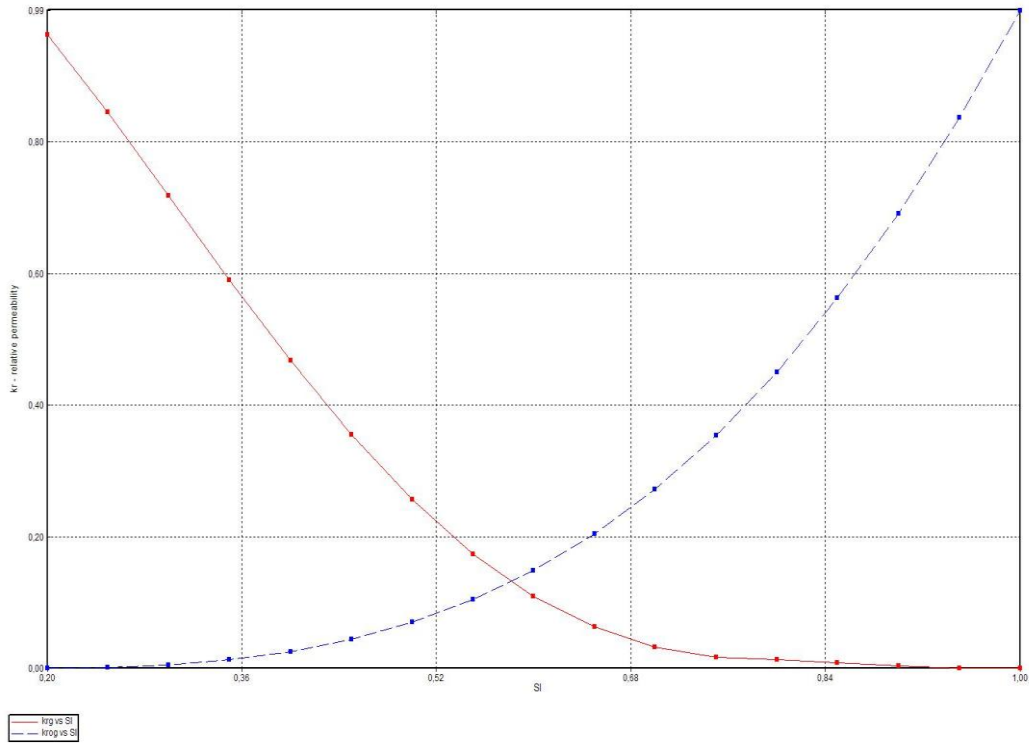| S_l	k_{rg}	k_{rog}
0.2	0.9567	0
0.25	0.84	0.0014
0.3	0.7143	0.0055
0.35	0.5872	0.0132
0.4	0.4652	0.0257
0.45	0.3531	0.0441
0.5	0.2549	0.0697
0.55	0.1731	0.1039
0.6	0.1090	0.1479
0.65	0.0626	0.2032
0.7	0.0330	0.2708
0.75	0.0176	0.3521
0.8	0.013	0.4481
0.85	0.0087	0.5596
0.9	0.0043	0.6873
0.95	0	0.8317
1	0	0.9942

Figure 3-13: Liquid-gas relative permeability plot

Rock compressibility and thermal rock properties

Compressibility of rock is temperature dependent. The value used in this model is 7E-6 1/kPa. Data is taken from a typical SAGD process field (Nasr et al., 2000)[35].

Thermal property data are taken from several sources (Deng (2005)[14], Nasr et al., (2000)[35], Prosper and CMG typical default values). A summary of the thermal properties of the reservoir is shown in **Table 3-10**.

Table 3-10: Thermal properties table

Volumetric Heat Capacity	2.35E+05	J/m^3·C
Thermal Conductivity of Reservoir rock	1.469E+05	J/m^3·C
Thermal Conductivity of Water	5.23E+04	J/m·day·C
Thermal Conductivity of Oil	1.24E+04	J/m·day·C
Thermal Conductivity of Gas	3.22E+03	J/m·day·C

To distinguish between reservoir formation and the overlying and underlying layers we assume that reservoir rock is sand enclosed by shale on top and bottom. Parameters specifying thermal properties of shale are given in **Table 3-11**.

Table 3-11: Overburden heat loss table

	Volumetric Heat Capacity (J/m³·C)	Thermal Conductivity (J/m·day·C)
Overburden	2.39E+06	1.486E+05
Underburden	2.39E+06	1.486E+05

3.3.6 Well Data

Wells are 500 m long and go through the entire reservoir. The horizontal producer is assigned in the grid blocks (45,1,25 to 45,2,25). The horizontal injector is situated 5 m above and is parallel to the producer through grid blocks (40,1,25 to 40,2,25). Zero skin factor in the perforation area is assumed. Wells are located at the side of the reservoir boundary, meaning that the well fraction is set to 0.5.

The geofactor is defined as a real number specifying the geometrical factor for the well element. In this case, the geofactor value is set 0.249 due to the symmetry element model with wells falling on the block center.
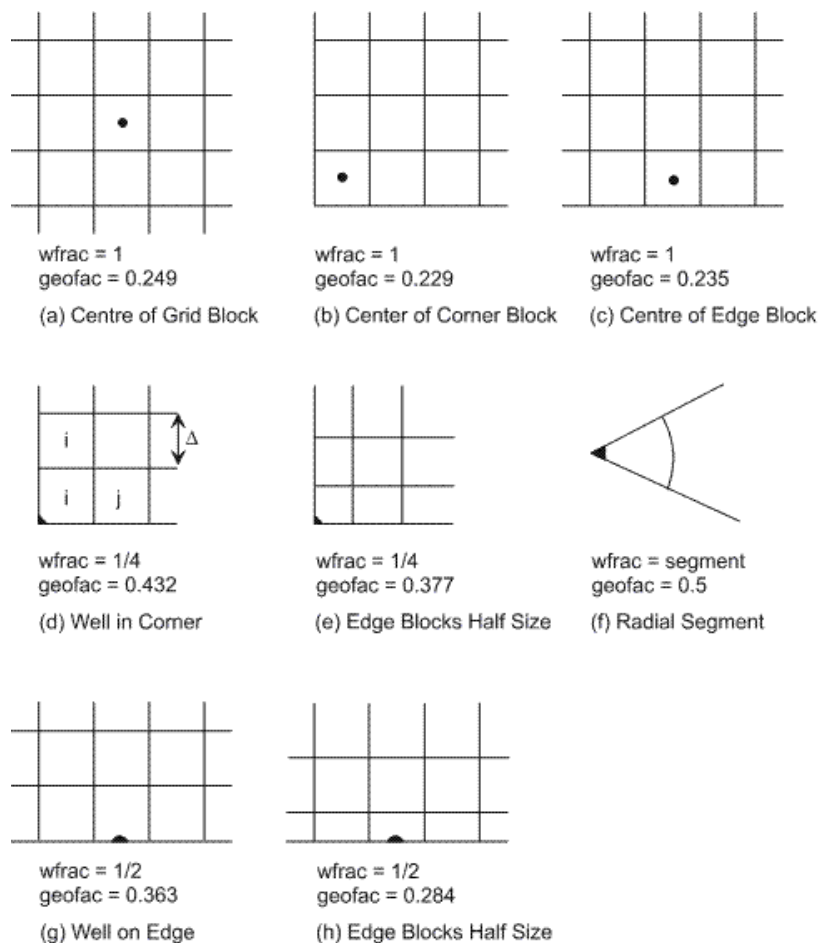

Figure 3-14: Well fraction and geometrical factor for various common geometries

The production well is constrained by minimum bottom hole pressure equal to 1200kPa and maximum surface liquid rate (STW) equal to 120 m3/day. The injection well has maximum bottom hole pressure 3000kPa and maximum surface liquid rate (STW) 120 m3/day. The injection fluid has the following parameters: temperature equal to 225 deg C, steam quality equal to 0.9.

3.4 Dimensional Analysis of Experimental and Numerical Models

The dimensionless similarity between the experimental model 1 and numerical model is based on the dimensionless parameters B_3 and $t^{'}$. Dimensionless time and parameter B_3 are given by **Equations 2-14** and **2-16**:

$$t' = \frac{t}{h}\sqrt{\frac{kg\alpha}{\phi\Delta S_O m v_S h}}$$

$$B_3 = \frac{t'}{F_O} = \sqrt{\frac{kgh}{\alpha\phi\Delta S_O m v_S}}$$

For the model experiment and numerical data the corresponding parameters are given in **Table 3-12**.

Table 3-12: Corresponding experimental and numerical model parameters

	Experimental model 1	Numerical model
$m^{(1)}$	3	3
$kg, m^3/d^2$	$151.2^{(2)}$	$0.135^{(3)}$
h, m	0.08	25
$\alpha, m^2/d$	0.017	0.147
$v_S, m^2/d$	$8.75^{(4)}$	$0.25^{(5)}$
ϕ	0.3	0.34
$\Delta S_O^{(6)}$	0.8-0.14=0.66	0.8-0.14=0.66
B_3	11.7	11.68

[1] To determine parameter m one needs to specify the viscosity at the steam temperature. This was not done with the experimental oil. For heavy crudes it is found that the parameter m should have a value of about 3 to 4 (Butler, 1991)[9].

[2] Corresponds to 2100 D. The value is obtained by correlation of the plot, obtained by Krumblein and Monk (1942)[32] for unconsolidated sands.

[3] Corresponds to 1.8 D. Was used as fitting parameter and corresponds to factor B_3.

[4] Estimated from **Figure 3-8** for $T_S = 103 \deg C$.

[5] Value from viscosity-temperature plot was used (**Figure 3-8**).

[6] Value of residual oil saturation equal to 0.14 used after the simulation run of the numerical model.

Scaling of temperature data from sensors in the experiment to simulated results is done by using the equation below:

$$\frac{T_{new} - T_{in}^{\exp}}{T_{steam}^{sim} - T_{in}^{sim}} = \frac{T_{old}^{\exp} - T_{in}^{\exp}}{T_{steam}^{\exp} - T_{in}^{\exp}}$$

(Eq. 3-26)

where:

T_{new} : scaled temperature in experiment

$T_{in}^{\exp}$: initial reservoir temperature in experiment (21 deg C)

$T_{steam}^{\exp}$: steam temperature in experiment (100 deg c)

$T_{old}^{\exp}$: temperature in experiment before scaling

T_{in}^{sim} : initial reservoir temperature in simulation (21 deg C)

T_{steam}^{sim} : steam temperature in simulation (233 deg C)

$$T_{new} = T_{in}^{\exp} + \frac{\left(T_{old}^{\exp} - T_{in}^{\exp}\right)\left(T_{steam}^{sim} - T_{in}^{sim}\right)}{\left(T_{steam}^{\exp} - T_{in}^{\exp}\right)} = 21 + \frac{\left(T_{old}^{\exp} - 21\right)\left(233 - 21\right)}{\left(100 - 21\right)}$$

CHAPTER IV
RESULTS AND DISCUSSION

4 RESULTS AND DISCUSSION

This chapter consists of four sections. First section of this chapter provides a comparison between analytical model and experimental model 1 SAGD process. Second section gives a analysis between experimental model 1 and numerical model. Third section of this chapter shows results of experimental model 2.

4.1 Analytical and Experimental (model 1) Comparison of SAGD Models

4.1.1 Position of Steam Chamber Interface

The geometry of the SAGD process is such that heated oil flow is approximately parallel to the interface that forms a boundary between the cold reservoir and the steam-saturated zone, known as the steam chamber. Consequently, by analytical solution it is assumed that the temperature inside the steam chamber is close to the steam temperature, and the oil saturation is approaching residual value. Thus, by calculating the position of the interface and observing its geometry one can roughly estimate the volume of oil recovered, which equals the volume of the steam chamber.

To calculate the position of the interface analytically **Equations 2-12** and **2-13** are applied. Parameters used in calculations are taken for experimental model 1 (**Table 3-12**). The results are providing original theory curves, which in the lower part of the interface move horizontally away from the production well. To avoid this effect the TANDRAIN assumption was used, where tangent lines to positions of interface were plotted and anchored to the production well. The set of curves for different time moments are shown in **Figure 4-1**. The X-axis presents horizontal distance from wells; the Y-axis presents vertical depth of reservoir with zero value at the surface.
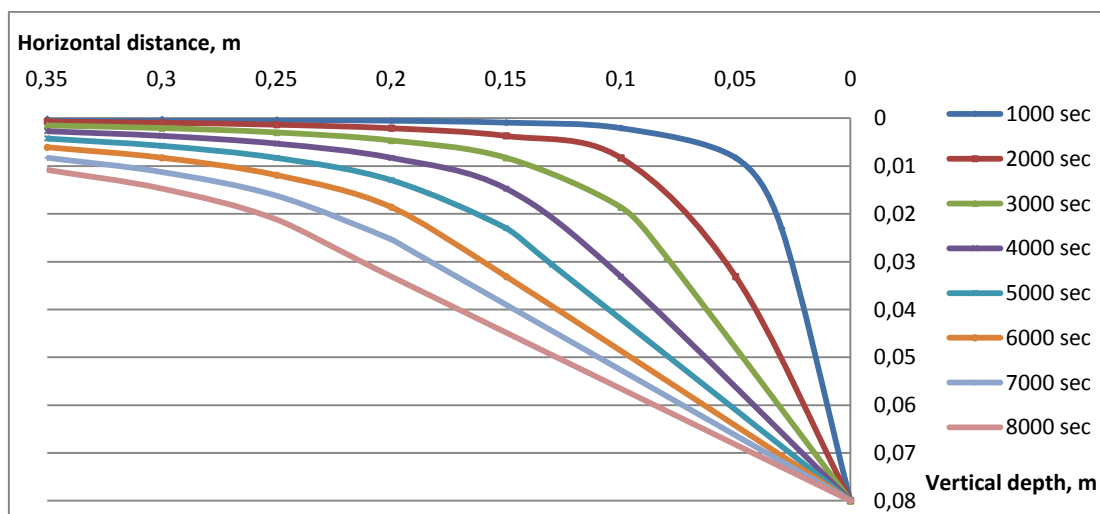

Figure 4-1: Calculated interface positions for a reservoir using TANDRAIN assumption

To plot temperature distribution in the reservoir model 1 the assumption is made that all sensors are situated on one line which is the repeating middle line (**Figure 4-2**). By this assumption all data are measured in one plane. Data are plotted in a cross section of the box as lines of equal temperature. Distances between sensors and injection point are measured along straight lines (**Table 4-1**).

Table 4-1: Distances from injection point to the sensors in experimental model 1

Sensors	Sensor 1	Sensor 2	Sensor 3	Sensor 6	Sensor 7
Distance from injection point, m	0,32	0,2	0,09	0,25	0,08

Steam is injected through a tube with length 13 cm. The injection tube is perforated all around the surface and along the entire length, except the 2 cm from each end. To simplify calculations the middle of the perforated part is chosen as injection source. Positions of sensors are determined relative to this injection source. For most of the sensors this simplification does not significantly affect the calculations. However, sensor 7 is more sensitive since it is situated close to one of the ends of the perforated pipe. Therefore, to be more accurate, the position of sensor 7 is measured relative to the closest end of the steam injection pipe.
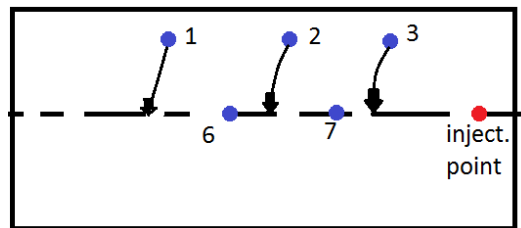

Figure 4-2: Imaginary shifting of all sensors to the vertical plane of the injector in the sand box

Figure 4-3 shows temperature propagation into the reservoir at different time intervals. The figure is constructed to follow different temperatures vertically and horizontally at specific times. As the injection time increases, temperature increases, following almost the same pattern. The injection point is taken at position (0 m; 0.04 m) and production well is taken at position (0 m; 0.08 m) on the graph. In general, the temperature increases vertically and then horizontally, following almost the same propagation trend.

Temperature distribution with time in experimental model 1 shows that the highest temperature is observed close to the injector and in the area above it. Fast temperature propagation is observed in the horizontal plane at the top of the reservoir. In remote areas of the reservoir, temperature profiles are almost parallel to each other having almost the same slope. During experiments the temperature inside the reservoir does not reach steam temperature. But at about 8000 sec. (2.22 hr) almost half of the oil sand volume has a temperature higher than 80 deg C.
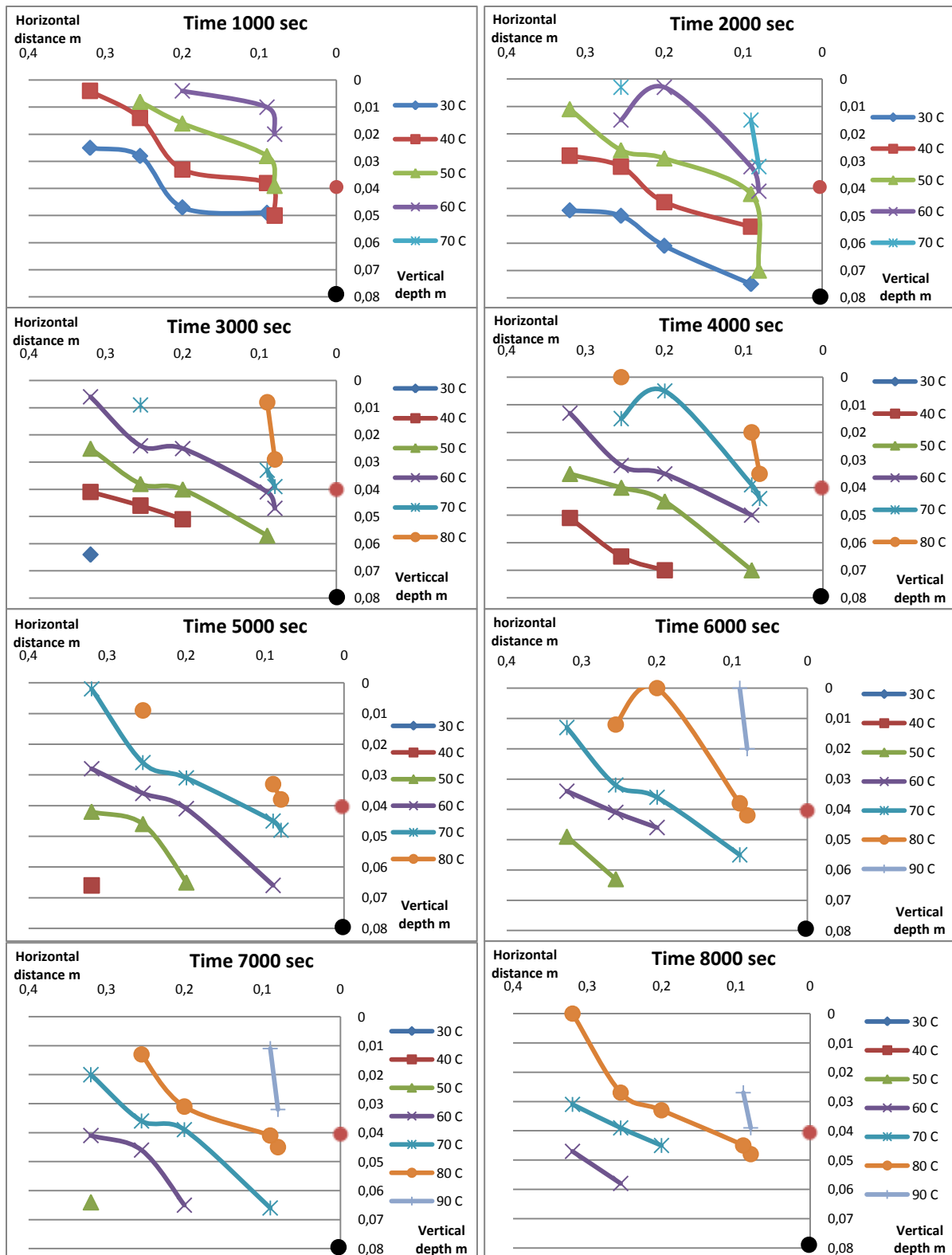
Figure 4-3: Temperature distribution in experimental model at different time intervals (red dot – injector placement, black dot – producer placement)

Data obtained in **Figure 4-3** along with **Equations 2-12** and **2-13** are used to analytically calculate the position of the interface using TANDRAIN curves, where the tangent lines of the interface position is extended to the production well (**Figure 4-4**). The black lines in the

graph are TANDRAIN curves. As can be seen it is reasonably in agreement with the experimental temperature propagation trend.
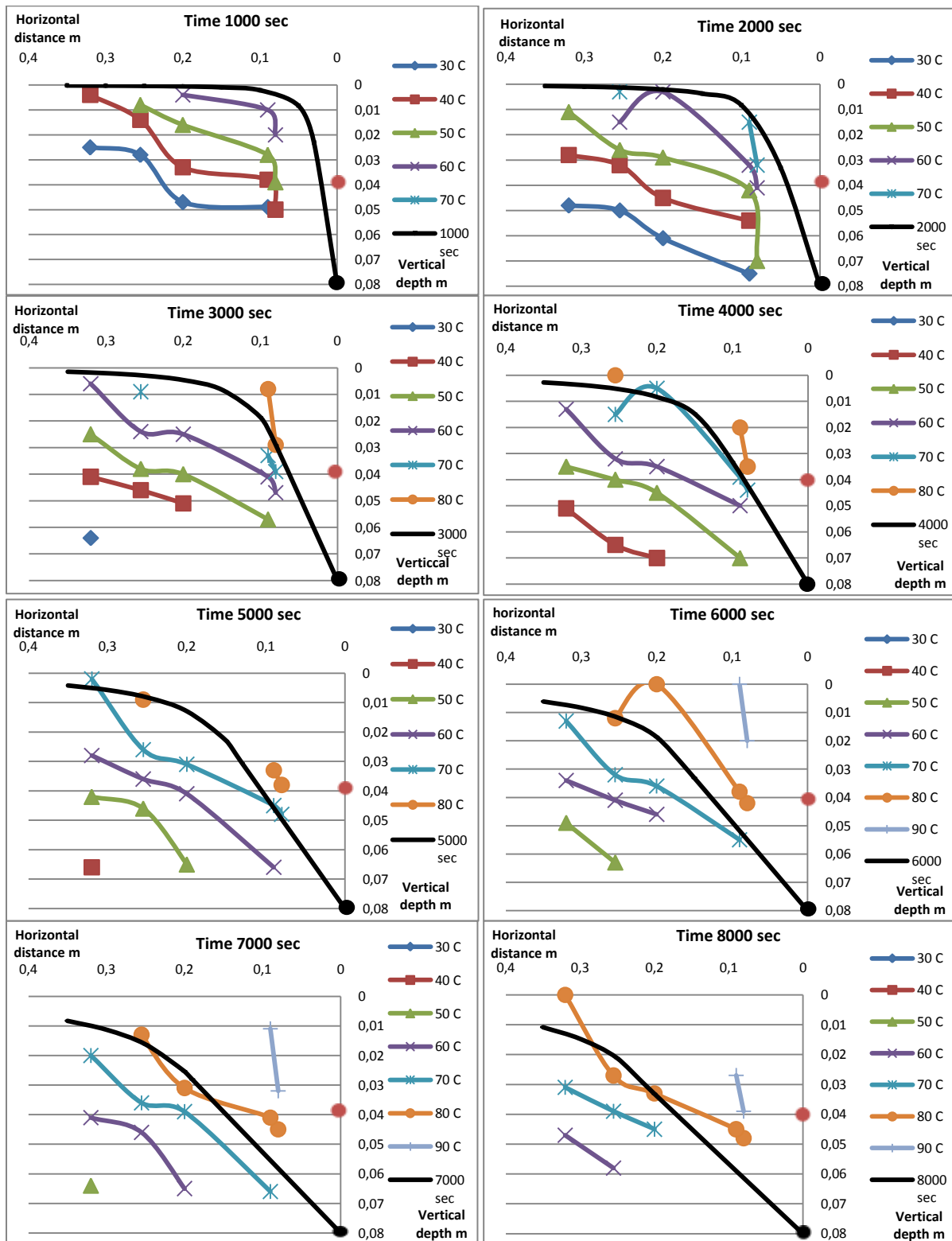
Figure 4-4: Comparison of analytical steam chamber interface curve and experimental temperature distribution in the vertical plane of injector (red dot – injector placement, black dot – producer placement)

Though experimental results have different magnitude of temperature compared to the analytical solution (black lines show steam chamber interface, meaning that the interface has almost the steam temperature), the trend is similar for both. The temperature difference is around 20-30 deg C.

Comparison shows that the steam chamber interface in the experimental model 1 is supposed to be in the range of temperatures between 70 and 80 deg C. This is contradicting the assumption made for the analytical solution that temperature inside of steam chamber is close to the steam temperature. The difference between values is about 20-30 deg C. Propagation of the steam chamber in experiments is slower due to non idealized conditions and some heat loss compared to the analytical solution. A heat transfer mechanism with heat loss as driving force of heat propagation is confirmed by another analysis of experimental data.

4.1.2 Analytical Model Approaches for Matching Experimental Temperature Data

Different approaches are followed in order to match the temperature data and suggest possible mechanisms. The different approaches are dependent on the directional flow of the heat. For example, at the start the steam chamber propagates to the top (overburden) and before moving along the overburden to the end of the model reservoir (box). Simultaneously the heat propagates at the different horizontal levels. As such the sensors would receive the heat transferred from the top and from horizontal injection.

The model approaches are: comparing the different temperatures that reach the sensors at the different locations and depths for heat transfer by conduction mechanism from overburden and heat transfer by conduction mechanism due to propagation from the steam injection point. The approaches provide the temperature distribution in space and time.

Approach 1 – Heat transfer by conduction mechanism from overburden

This approach is based on the assumption that steam propagates fast at the top reservoir, and conduction from surface down to the reservoir is the dominant mechanism of heat transfer (slab heating). For calculations of conduction heating it is assumed that the reservoir is a slab and that it is heated from one side (surface). In the calculation the equation of unsteady state conduction through the slab was used (Carslaw and Jaeger, 1959).

$$\frac{T_s - \overline{T_b}}{T_s - T_a} = \tau \frac{8}{\pi^2} \left(e^{-a_1 N_{Fo}} + \frac{1}{9} e^{-9 a_1 N_{Fo}} + \frac{1}{25} e^{-25 a_1 N_{Fo}} \right) \qquad \textbf{(Eq. 4-1)}$$

Where: τ = 1.1054 (fitting factor to match average temperature at the initial time)

a_1 = $(\pi/2)^2$

$N_{Fo} = \alpha t / s^2$

Recorded data of experiment 10 (1.5 cm depth of sensors) for a model 1 are used as surface temperature T_s of the overburden. The depth of the sensors is taken as the thickness of the

slab. Calculated results are compared with experimental data for different depths and results for 5cm depth are shown in **Figure 4-5**. Temperature distribution of sensors differs with space, depth and time. This approach gives a better fit for results from sensor 7 at all depths, for sensor 3 at all depths excluding 6.5 cm, and for sensor 2 at depths of 4 cm and 6.5 cm. In other cases an over estimation of the temperature is observed.
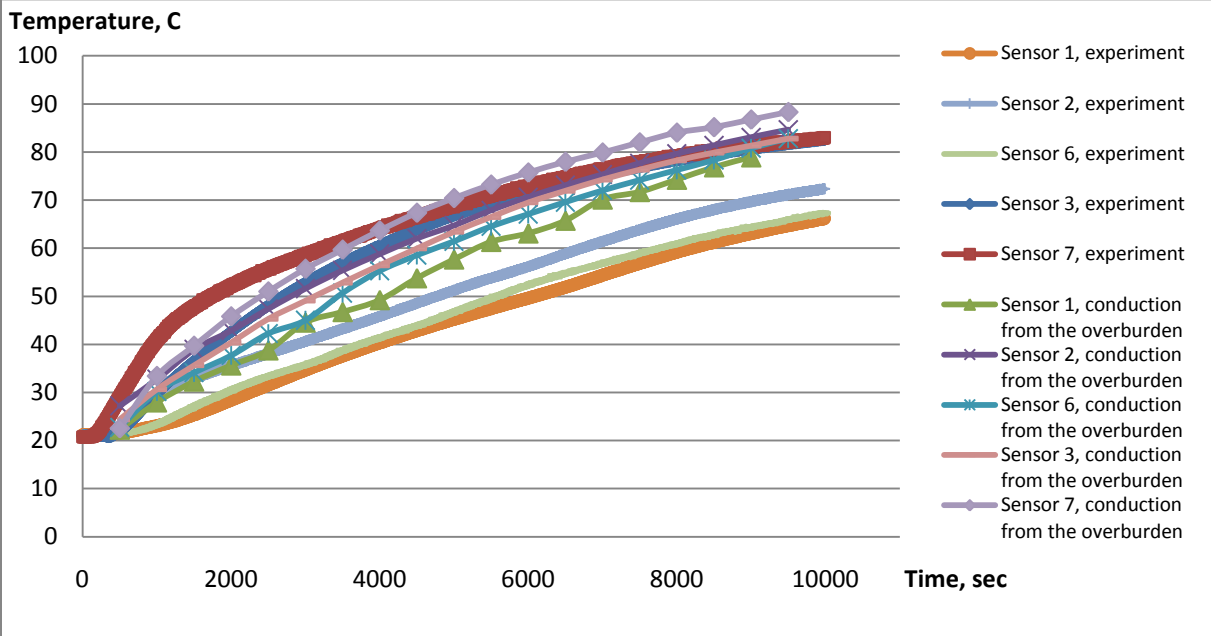

Figure 4-5: Comparison between temperature measurements as a function of time at 5 cm depth in the experiment 3 and estimated temperature by conduction from the overburden

Approach 2 – Heat transfer by conduction mechanism due to propagation from steam injection point

In this approach we assume that at zero time the steam rises above the injection well, creating a vertical radial front with temperature of steam. The steam front interface serves as heat source for further propagation. This approach assumes uniform heating at all depths which is simplistic and not realistic.

Calculated results in **Figure 4-6** show low temperature propagation compared to experimental data. The difference between experimental and estimated data is much larger at the top of the reservoir and decreases with depth. The fit between calculations and experiments are best for sensors 3 and 7.
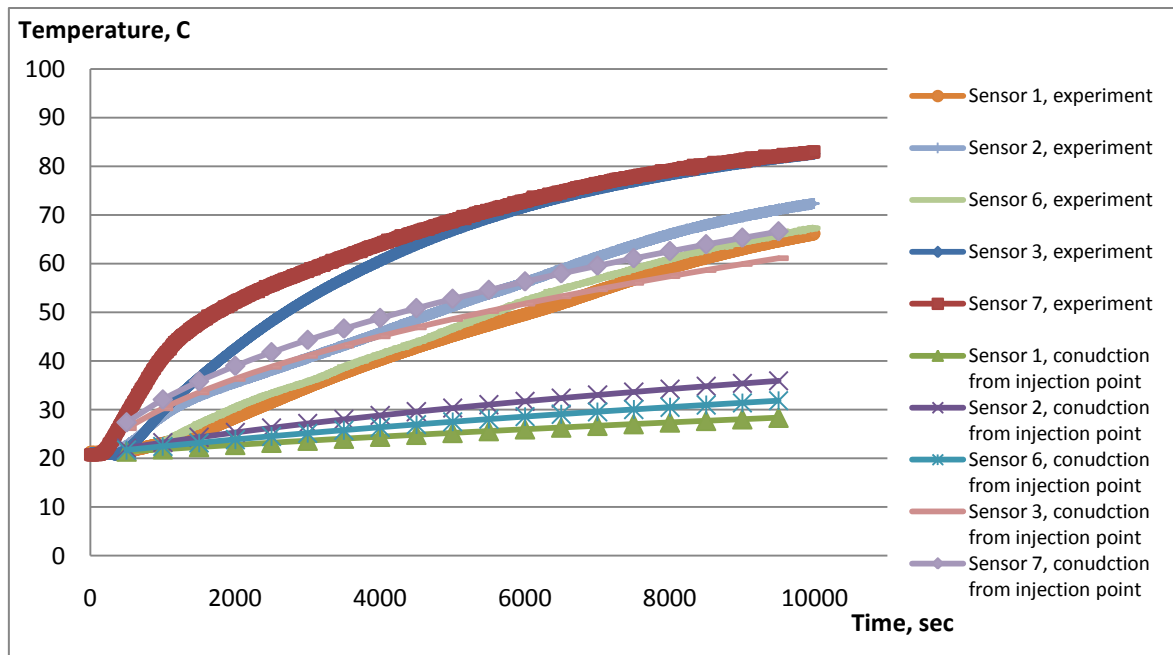
Figure 4-6: Comparison between temperature measurements as a function of time at 5 cm depth in the experiment 3 and estimated temperature by conduction from the injector point

Combining these results of heat transfer by conduction from overburden and heat transfer due to propagation from injection point, we may explain the over estimation of heat transfer from the overburden and under estimation of heat transfer from the injection point. Starting from sensor 3 and 7, they both are situated approximately at the same distance from the steam injection point. Analysis shows that in this area both mechanisms appear. Heat loss also occurs due to the relatively low temperature of fluids which flow to the production well. Calculation of the conduction heat transfer from the overburden over estimates the temperature distribution in general. However, in the case of sensors 3 and 7 the fit is good within experimental uncertainty. This is due to the significant heating occurring as a result of the conduction from the injection point, even if the calculation of this mechanism shows under estimation. Combining these two sources of heating together is likely to bring higher experimental temperature than what is recorded. However, heat loss in this area leads to a satisfying fit between estimated and experimental data.

The same explanation might be applied for areas further away from the steam source. The conduction mechanism of heating due to propagation from injection point alone results in an insignificant temperature rise (at 10000 sec the temperature is less than 40 deg C). Heat transfer by conduction from the overburden shows over estimation of the temperature in the area. The explanation is the same; the difference between conduction mechanisms of heating from both sources and experimental data occurs due to heat loss of produced fluids (Romanov and Hamouda, 2011)[41].

52

4.1.3 Analytical and Numerical Comparison of Steam Chamber Interface

Parameters of the numerical model can be taken to apply for the analytical solution. **Figure 4-7** shows temperature distribution within the reservoir at cross section in the i-k plane after two years of simulation. Parts of reservoir which have temperature of the steam are indicating the steam chamber interface. After 2 years the steam chamber reaches the overburden of the reservoir and starts growing laterally at the top of the model. Results of the analytical solution are presented in the same i-k plane for the reservoir model in **Figure 4-8**. Comparison shows very fast steam chamber growth compared to the numerical model. However the trend of propagation is similar for both results. At an early stage the numerical model has a delayed steam chamber rise due to absence of communication between wells. Only after creating connectivity the steam chamber is starting to rise. Propagation of the steam chamber occurs in a similar manner as analytical solution. The assumption of a vertical steam front at zero time in Butler's model is also confirming the time difference when comparing propagation. It will be discussed later that the numerical model has a time delay in temperature propagation compared to the experimental results.
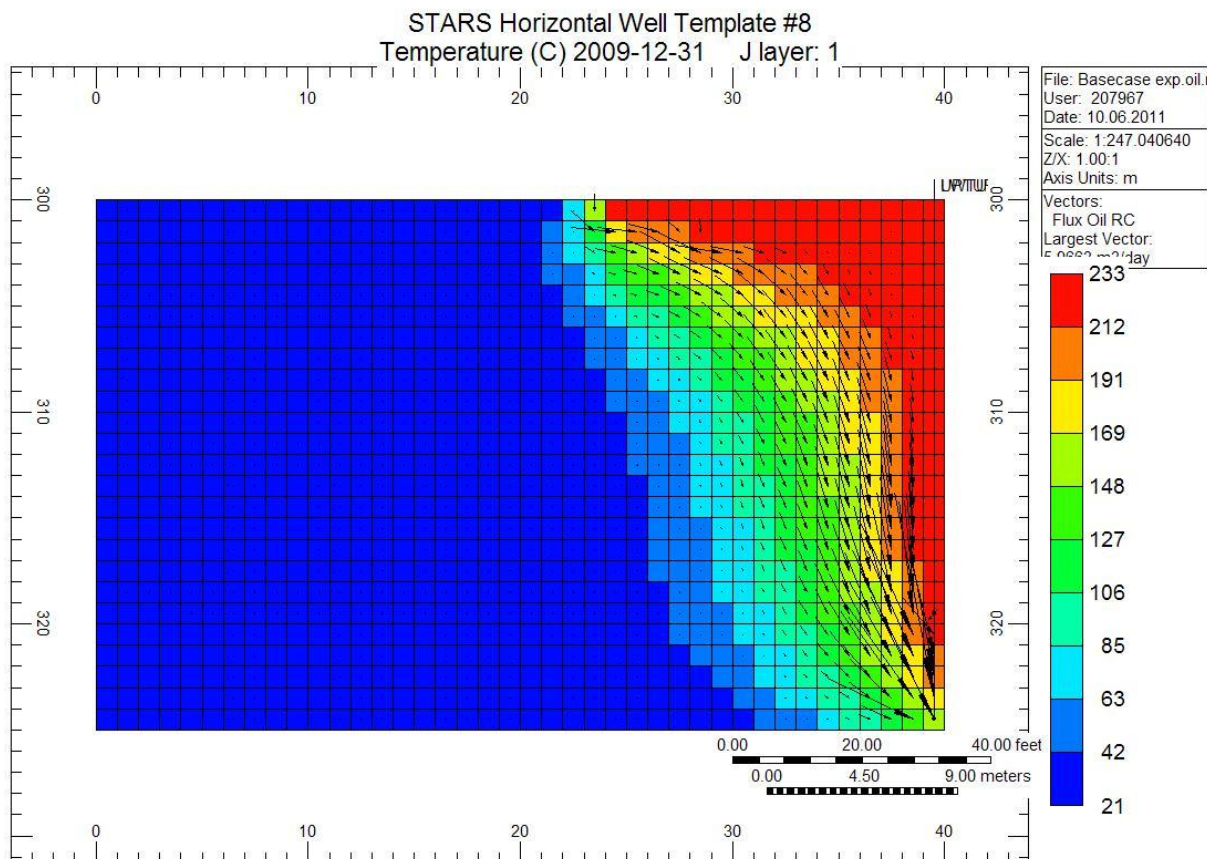
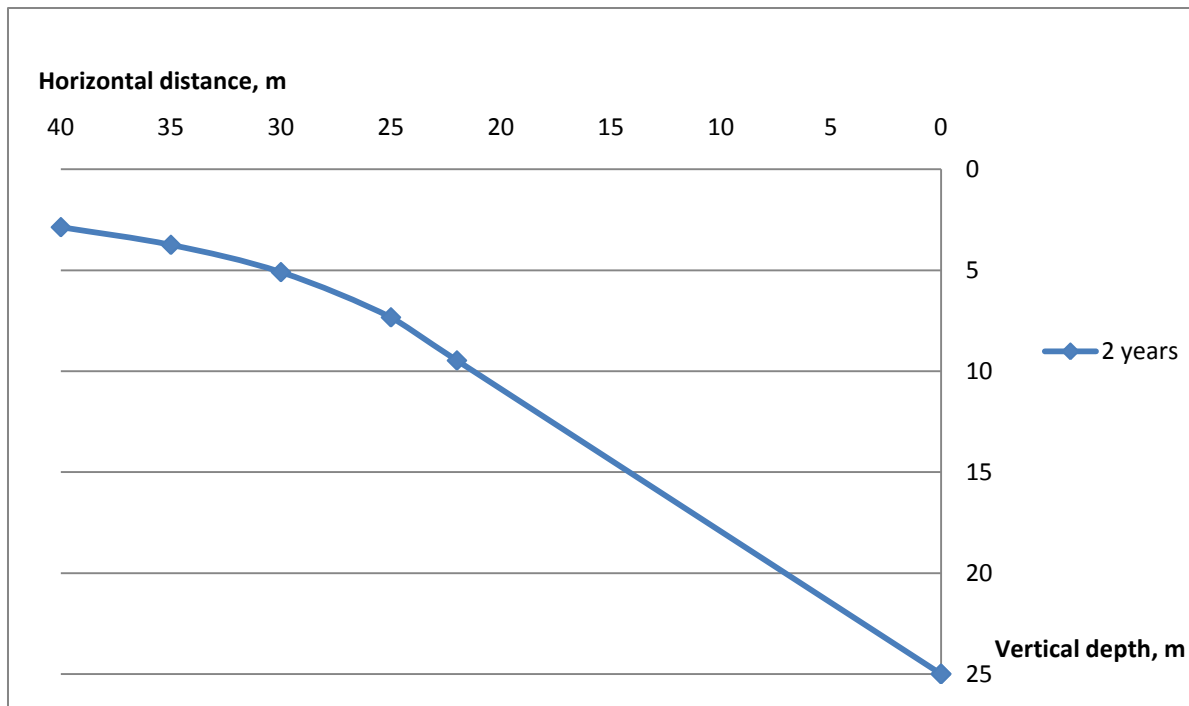**Figure 4-7: Temperature distribution in numerical model after 2 years**

Figure 4-8: Analytical interface curve for numerical model after 2 years

4.1.4. Temperature Gradients around Sensors in Experimental Model 1

Temperature gradient is used here in order to indicate the magnitude of the different heat transfer mechanisms. The following are the set of experiments (Model 1) performed in order to map the gradients. The sensors depth is selected based on their distance from the overburden (top of the experimental model). The steam is injected at a depth of 4 cm.

- Experiment 3 (5 cm depth of temperature sensors).
- Experiment 7 (6.5 cm depth of temperature sensors, maximum allowable depth of sensors)
- Experiment 9 (3 cm depth of temperature sensors)
- Experiment 10 (1.5 cm depth of temperature sensors)
- Experiment 11 (4 cm depth of temperature sensors).

Data from experiment 10 (1.5 cm depth) are used to determine the temperature distribution at the overburden of the experimental model box. The depth of 1.5 cm is the smallest depth that can be achieved due to the sensor configuration.

Temperature gradients versus depth for different sensors at different time intervals are estimated by **Equation 4-2**. This approach uses the assumption that at initial time steam is propagating fast to overburden and becomes as heating source.

54

$$grad T_{di} = \frac{T_s - T_{di}^t}{di}$$
(Eq. 4-2)

Where, T_{di}^t – temperature at certain depth di and at time t.

Figures 4-9 and **4-11** are constructed to map the temperature gradient in the experimental model as a function of the vertical and horizontal distances, respectively at different time intervals. In spite of the complexity of the different processes taking place, consistent temperature gradients are established within the reservoir. Similar processes are occurring throughout the whole reservoir, as seen in gradient profiles for the different sensors.

Sensor 1 is the most remote sensor from the injection point of the steam (0.32m). **Figure 4-9a** shows gradients along sensor 1 estimated from experimental temperature data. At 1000 sec, the gradients decrease with the depth. General trend is that at depths 3 and 5 cm gradients have highest values while at depth of 4 cm low gradient is indicated. The low gradient at 4 cm may be explained by the influence of the injector location, which is at 4 cm. Variation of the gradients changes with time for sensor 1 may indicate that it has not reached steady state.

Figure 4-9d shows the temperature gradients for sensor 6. The temperature gradients are between about 3 and 6 C/cm, ignoring the earlier time (1000 sec.) with small changes in the gradients as a function of depth, that reaches to minimum (between 3-3.5 C/cm) after 8000 sec. The gradient profiles are different from the gradient profile for both sensor 1 and 2. This may be explained based on that the sensor 6 lies in the same vertical plan as the injector, hence heats up the area around the sensor and reduce the gradient. It is rather interesting to see similar behavior of the trend for sensor 7. The gradients for sensor 7 are between about 1.5-5C/cm, indicating arrival to steady state situation faster than that for sensor 6. At 8000 sec the variation of the gradients with depth is between 1.5 and 3.5C/cm, at depth of 3 and 5 cm, respectively. The gradient trends for both sensors 6 and 7 are very much similar and both lie on almost the same vertical plan as that for the injector, which may support the given explanation on the variation of the gradients. However, in sensor 6, increasing time from 1000 to 3000 sec., as expected, a decrease in the gradients occur, after which (4000 sec.), the gradient increased to about 5.5C/cm which is larger than that estimated at 2000 sec. The gradients followed the expected trend above 4000 sec. This unexpected gradient increase after 3000 sec. may be explained by the large increase of temperature at the overburden from 67 to 78C as shown in **Figure 4-10**, which influenced the calculated gradients.

Sensor 3 is situated on periphery but close to injection point (0.09m). Temperature gradients along sensor 3, estimated from experimental data are shown in **Figure 4-9c**. It is clearly seen that profiles are consistent during entire experiment. First 3000 sec. gradients increase significantly from 3 to 4cm depth, and have smaller increase from 4 to 5cm depth. It is indicating that in early time and at higher depths heating from horizontal direction of injector is becoming more intensive than areas above which are mostly heated from the overburden. At later time gradient profiles have almost liner increase with the depth. It is a result of becoming closer to the steady state heating of this reservoir area.
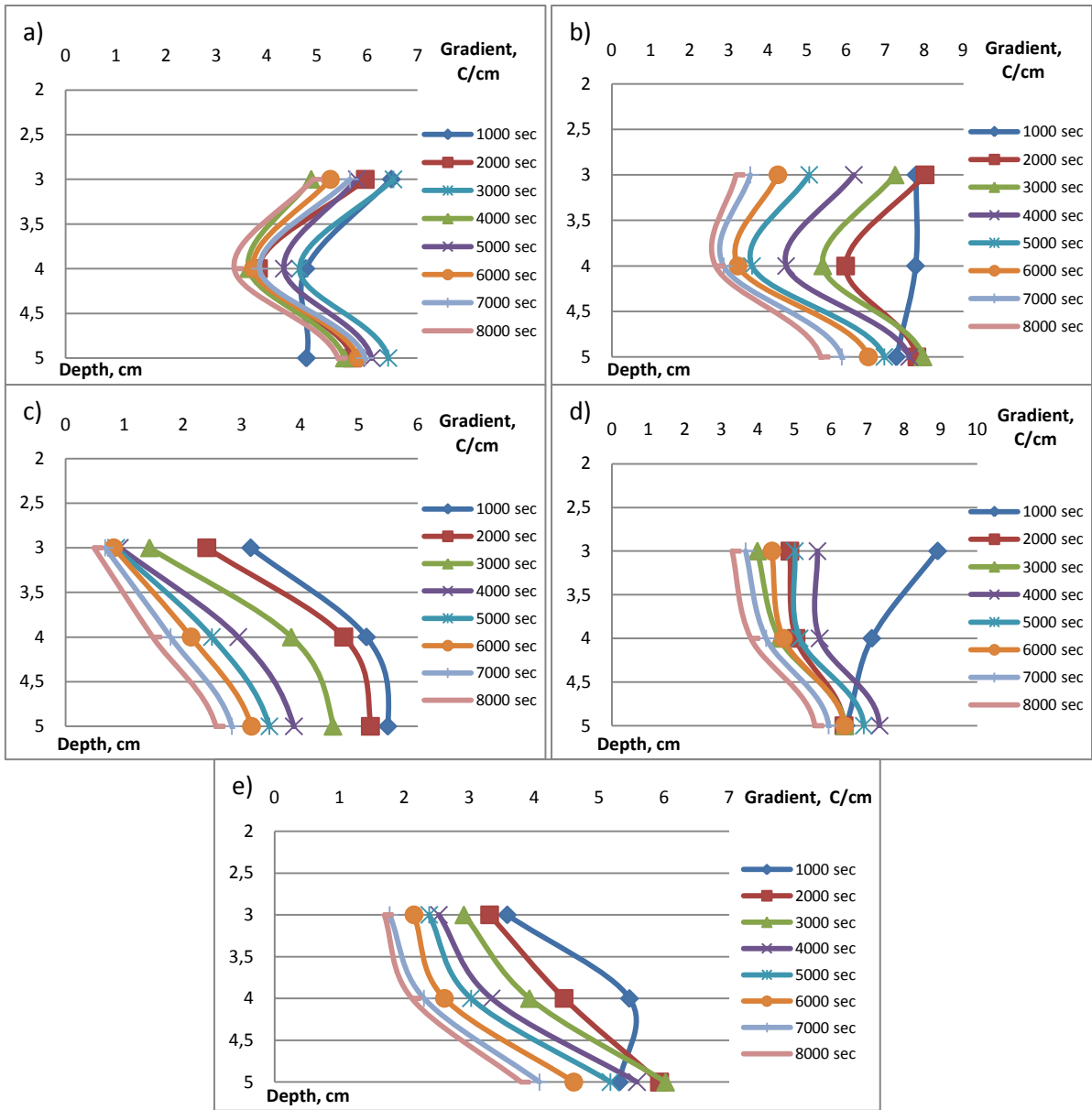
Figure 4-9: Temperature gradients around sensors at different time intervals, estimated from experimental data (a–sensor 1, b–sensor 2, c–sensor 3, d–sensor 6, e–sensor 7)
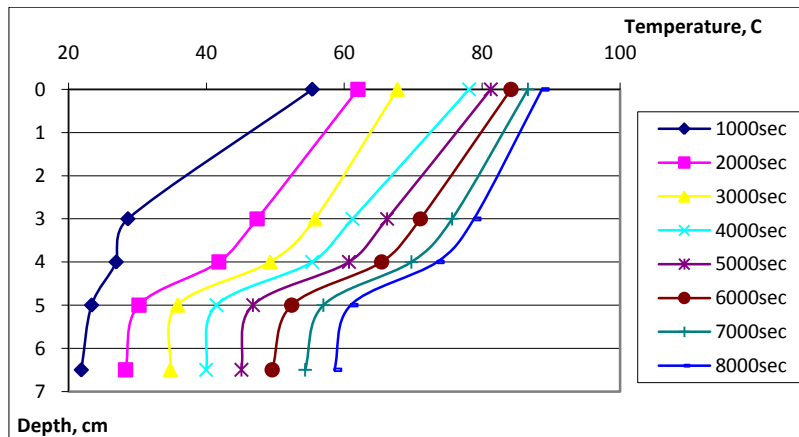

Figure 4-10: Temperature distribution along the sensor 6 as a function of time

Temperature gradients in horizontal direction (from injector plan) graph is constructed similar to that for the overburden. However it is assumed that the temperature at the vertical distance (from injector to the top) in the injection plan is the same as steam temperature. In other words the heat is conducted from the vertical plan above the injector.

$$gradT_{Di} = \frac{T_s - T_{Di}^t}{Di}$$

(Eq. 4-3)

Where T_{Di}^t – temperature at certain horizontal distance Di at time t.
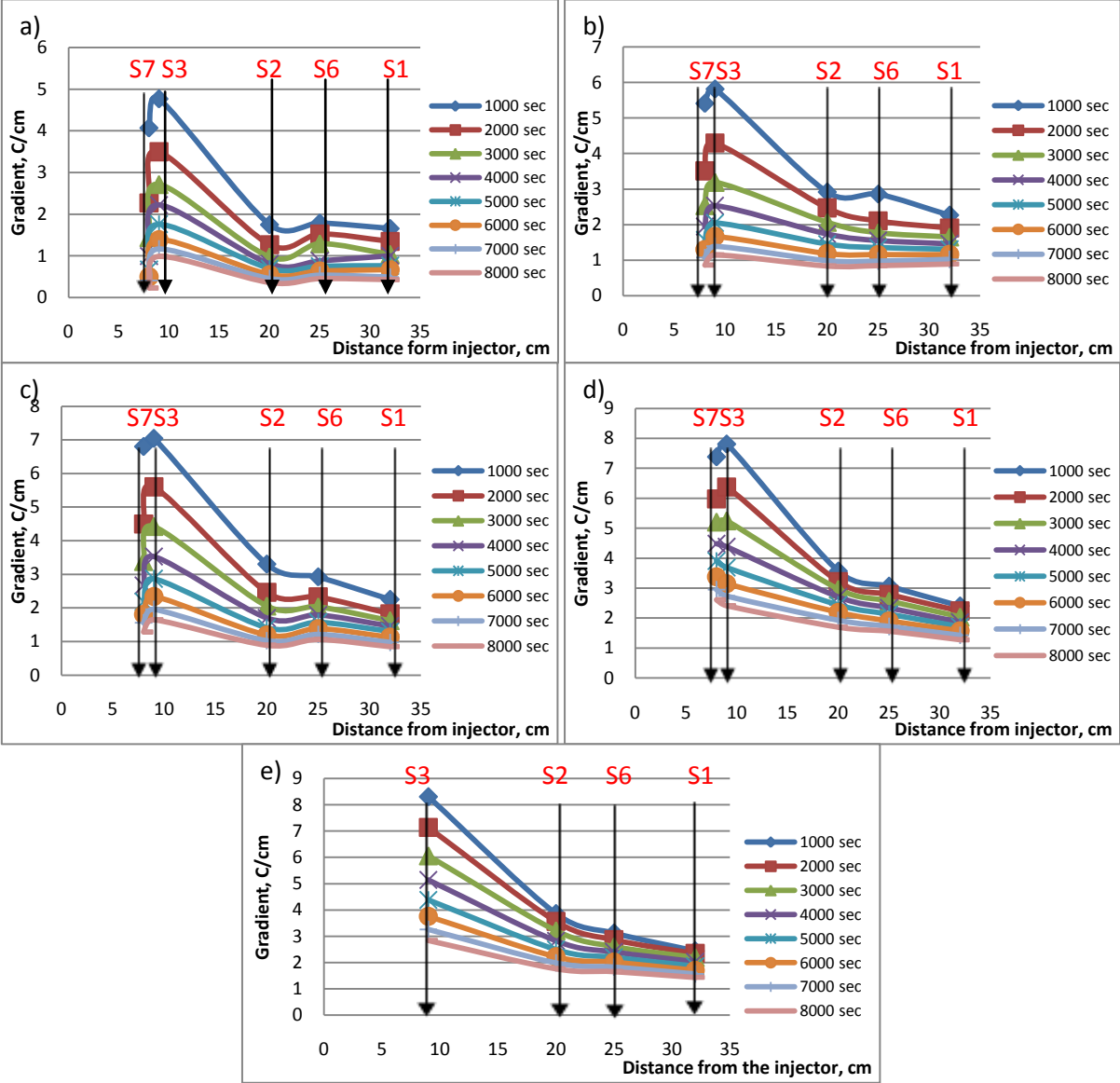
Figure 4-11: Temperature gradients estimated from experimental data at different distance from injector (distance measured from middle point of perforated part) as a function of time (a–depth 1.5cm, b–depth 3cm, c–depth 4cm, d–depth 5cm, e–depth 6.5cm)

Figure 4-11 demonstrates the change in the gradients with time. It is shown that above a distance of 20 cm, less change in the gradients at a given time. It is interesting to see that sensor 3 has higher temperature gradients than sensor 7, in spite of the fact that sensor 7 is located almost at the vertical plan at the end of the injector, that is to say slightly closer to the injector than sensor 3. This may be explained based on that the area of sensor 3 receives heat from overburden at earlier time than sensor 7, in addition sensor 7 receives heat from the injector, so the area of sensor 7 has higher temperature than sensor 3, hence less gradient.

In order to relate the calculated gradients with experimental results, **Figure 4-12** is constructed using Equation 4-1 at different depth (**Figure 4-12a**) and at different horizontal distance from the injector (**Figure 4-12b**). **Figure 4-12a** shows a comparison between theoretically calculated temperature gradients due to conduction and averaged gradient values of experiments for sensor 3 and 7. Averaged values of sensor 3 and 7 are taken, to represent this reservoir area, and they are situated almost at the same distance from the injector (but they are not in the same vertical plan), hereby can be taken as representative for close area of reservoir relative to injector.

Results show that at early time (2000, 4000 sec.) gradients estimated based on experimental data have lower values than that predicted based on conduction, where the overburden (top of the box) temperature is taken as the heating source. At later times (6000, 8000 sec.) experimental and theoretical results are in a good agreement. It may be explained that at the early stage of the experiment the proximal area gain heat due to convective heat transfer. In this time period the steam chamber is growing intensively around and above the injector. As the time increases steam chamber grows into the area of sensor 3 and 7, and conduction becomes the dominating heating mechanism inside of the steam chamber. Therefore a better agreement between the experimental based gradients and the calculated one. In case of the more remote areas, where sensors 1, 2 and 6 are placed, the convection has a stronger influence during the experimental time of 8000 sec. That is to say a closer agreement is expected to be obtained if the experimental time is sufficiently increased above 8000 sec., following the trend of the other sensors.

The temperature gradients in horizontal direction are shown in **Figure 4-12b**. In this graph the average values of temperature gradients at depths 3, 4, and 5 cm are taken, in order to compare theoretical calculated results with experimental data. Theoretical calculations over estimates temperature gradients with time, but with increasing distance from injection source, the difference in the gradients decreases. It also means that convection has strong influence on heating of the reservoir ahead of steam chamber interface, similar to that for the vertical graph **Figure 4-12a**.

The analysis of the temperature gradient indicates that convective heat transfer contributes to heat flow ahead of the chamber at the interface, as steam chamber propagates further, conductive heat transfer becomes more and more dominating mechanism. The analysis of temperature gradient from different heating sources shows that horizontal heating from injector is pronounced only at closest area. In rest of reservoir additionally created source of

heating at top of formation is dominating in heating of underlying layers (Romanov and Hamouda, 2011)[41].
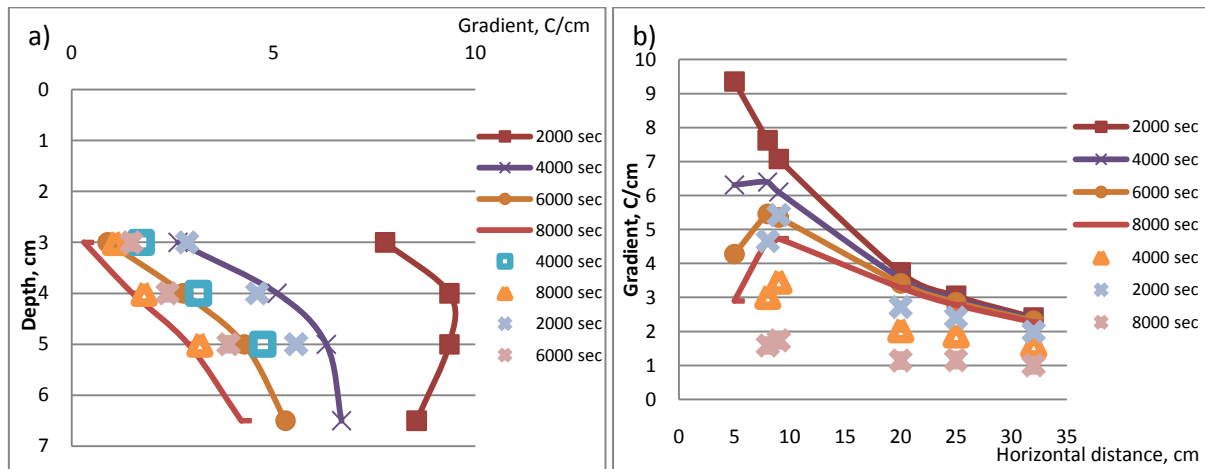

Figure 4-12: Comparison between estimated temperature gradients from experimental data and calculated by conduction heat transfer (a – gradient changes in vertical direction relative to overburden, b – gradient changes in horizontal direction relative to injector). Curves show estimated conductive heat transfer, dots are experimental results

4.2 Comparison of Experimental Model 1 and Numerical Model

Temperature distribution profiles for base case numerical model are shown in **Figure 4-13**.
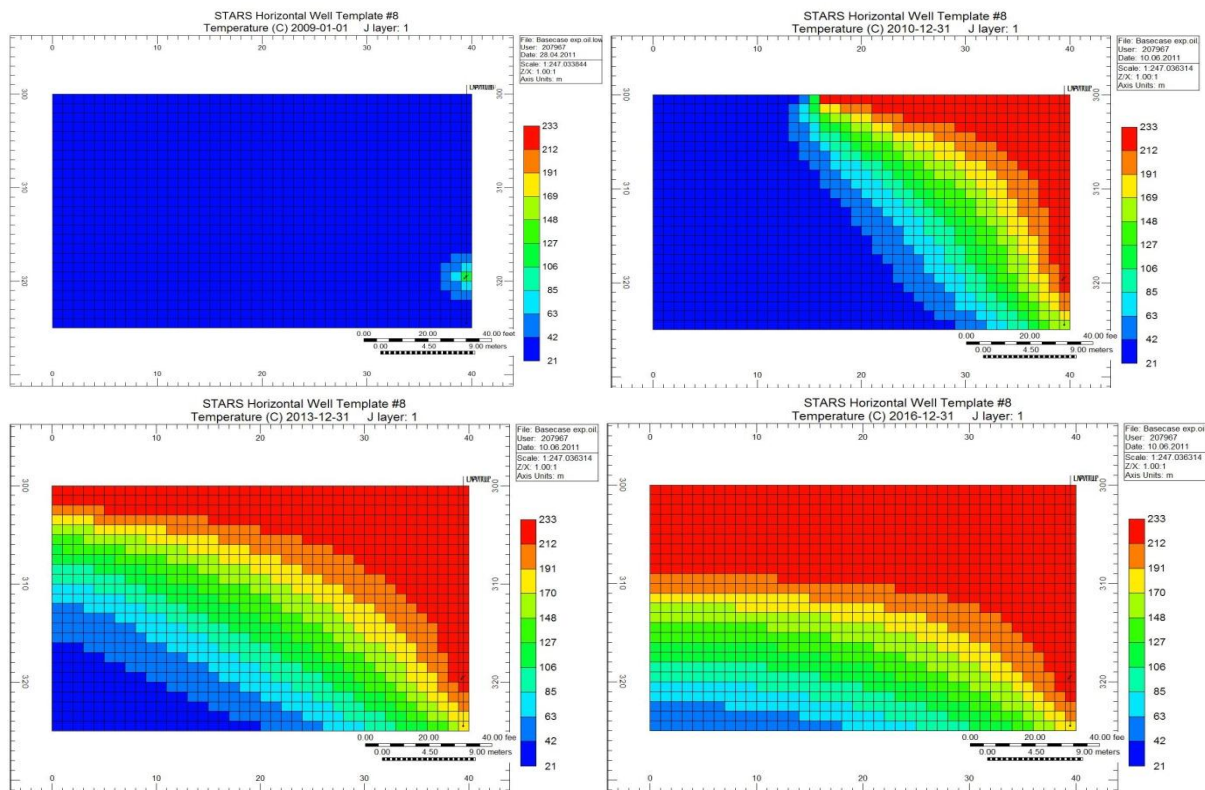
Figure 4-13: Temperature distribution after 1, 3, 6 and 9 years respectively

Steam chamber growth in the numerical model is similar to the experimental data trend. Steam first propagates fast in the vertical direction above the injector and then spreads at the top of the reservoir heating underlying layers. In the numerical model the angle of the steam chamber edge is more inclined relative to the horizontal compared to the experimental results. This might be explained by different relative thicknesses of the reservoirs. To quantitatively compare experimental and numerical models, dimensional similarity analysis should be performed.

4.2.1 Comparison of Temperature Distribution

In order to compare experimental and simulated temperature profiles for certain positions of sensors it is necessary to find dimensional location in the reservoir for both experimental and numerical case. Dimensionless distance between sensors and injection point in the experiment might be taken as the ratio of distance from sensor to steam injection point and length of model (0.5 m). To find equivalent positions of sensors in the simulation model, dimensionless distance should be used to find location of blocks in numerical model.

Table 4-2: Dimensionless positions of sensors in experimental and numerical models

Sensor	Experimental distance of sensors, m	Dimensionless distance	Coordinate i
Sensor 1	0.32	0.64	14
Sensor 2	0.20	0.4	26
Sensor 3	0.09	0.18	32
Sensor 6	0.25	0.5	20
Sensor 7	0.08	0.16	34

Coordinate k should be also specified depending on experimental depth. To find dimensionless depth of each experiment the ratio between sensors depth in experiment to entire depth of reservoir model (11 cm) is taken. Using dimensionless depth of experiments it is possible to find the corresponding coordinate k (depth) in the numerical model.

Table 4-3: Dimensionless depths of sensors in experimental and numerical models

Experiment Nr	Experimental depth of sensors, cm	Dimensionless depth	Coordinate k
Experiment 10	1.5	0.14	3
Experiment 9	3	0.27	7
Experiment 11	4	0.36	9
Experiment 3	5	0.45	11
Experiment 7	6.5	0.59	15

A correspondence between the time of experiment and the time in the simulated model is found by using dimensionless time from **Equation 2-14**. Parameters used in the equation for both experimental and numerical models are taken from dimensionless analysis, presented in **Table 4-4**.

Table 4-4: Corresponding time for experimental and numerical models

Time in experiment, t_{EXP}, sec		Dimensionless time, t'	Time in simulation, t_{NUM}, days	
sec	hours		days	years
1000	0.28	0.36	131	0.359
5000	1.39	1.8	655	1.79
10000	2.8	3.6	1310	3.59

Initial reservoir temperature is the same for both models and equal 21 deg C. Injected steam temperature is different due to different pressure in the experimental study (around atmospheric pressure) and numerical simulation (equals 30 bar). Temperatures of steam are 100 and 233 deg C for experimental and simulation models respectively. In order to compare results quantitatively, temperatures need to be scaled. Scaling of temperature data from experimental to simulated results is done by using **Equation 3-26**:

$$\frac{T_{new} - T_{in}^{exp}}{T_{steam}^{sim} - T_{in}^{sim}} = \frac{T_{old}^{exp} - T_{in}^{exp}}{T_{steam}^{exp} - T_{in}^{exp}}$$

Results are shown in **Figures 4-14** and **4-15**. At middle depth (5cm is the depth of sensors in the experiment) it can be seen that at early time experimental temperature rise occurs faster for all sensors. Numerical results have a delay in temperature growth in all parts of the reservoir. However, it is clearly seen that simulation results become similar to the experimental data earlier in areas closer to the steam injection point. Temperature growth at sensor 7 becomes similar for experimental and numerical results at time of simulation equal to 900 days (corresponding to 1.9 hours in experiment), and at sensor 3 at time equal to 1400 days (corresponding to 3 hours in experiment). Looking further away from the steam source it is observed that the time delay between experimental and numerical results are increasing with increasing distance from sensors to steam injection point. For example, results for sensor 2 at 1600 days of simulation show that experimental and numerical temperature propagation becomes similar and it might be predicted that at a later time temperature rise would be the same. Sensors 6 and 1 have quite high temperature differences even after 1600 days. Simulation results show that the temperature in the areas of these sensors starts to grow rapidly at a later time. One can assume that after a certain time, profiles of experimental and numerical temperature growth will be similar.

Results at lower depth (3cm is the depth of sensors in the experiment) are similar to those of the sensors at depth 5cm. For sensors 3 and 7 approximately the same time has to pass before experimental and numerical temperature data are similar. More remote sensors have increased time delay between numerical and simulated results.

This observation illustrates that the numerical model underestimates the temperature increase in the early stage of the SAGD process, the increase growing rapidly after some time and becoming identical to that of the experimental temperature propagation. In addition, time delay occurs not equally for the entire reservoir but it increases with lateral distance from

injector. It may be concluded that simulation results give more reliable data for areas closer to the steam injector and production well. For remote areas, simulation shows stronger under estimation of reservoir heating with time.
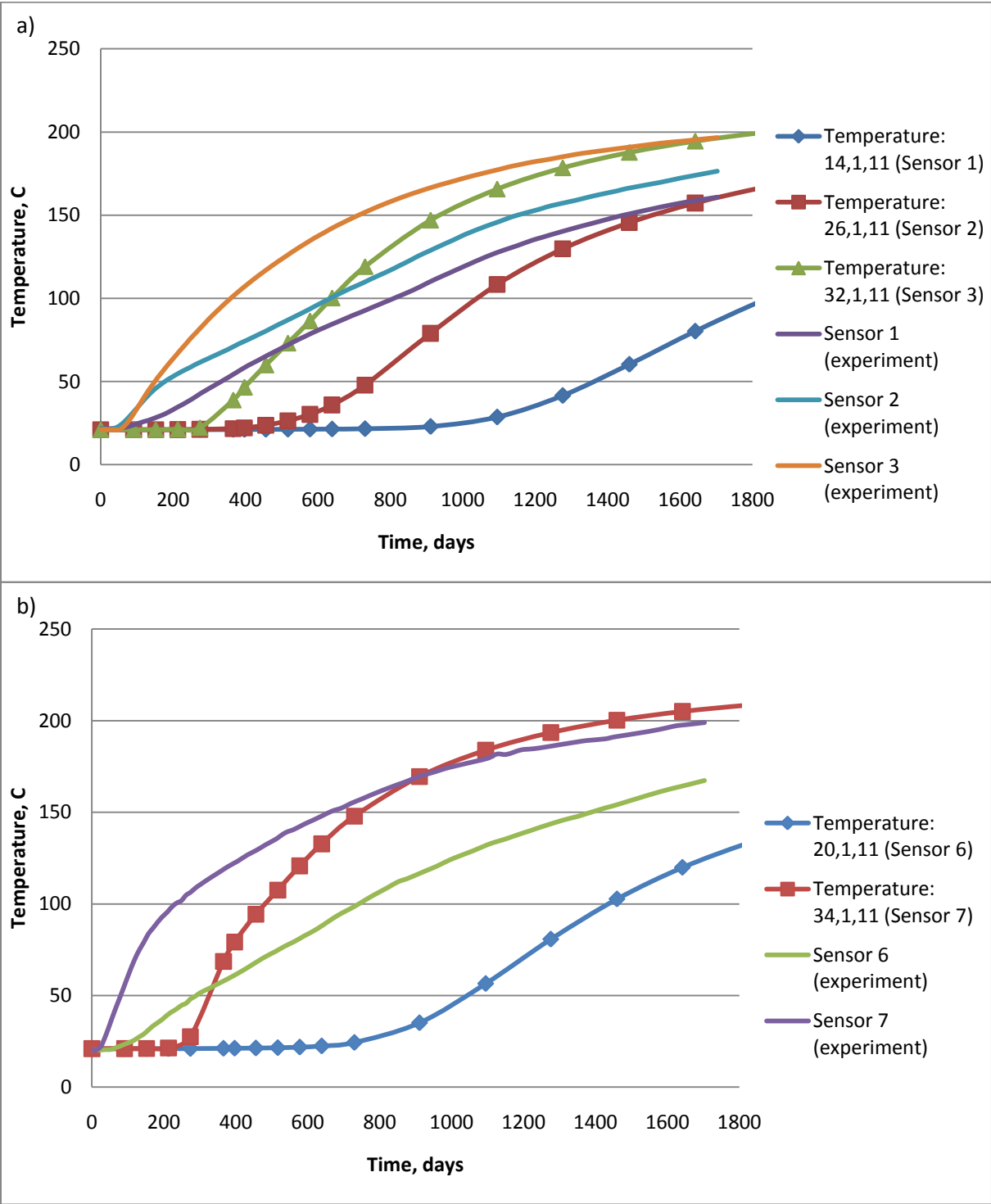

Figure 4-14: Simulation results with corresponding 5cm depth of sensors and scaled experimental results of temperature propagation in model 1 (a – Sensors 1, 2, 3; b – Sensor 6, 7)
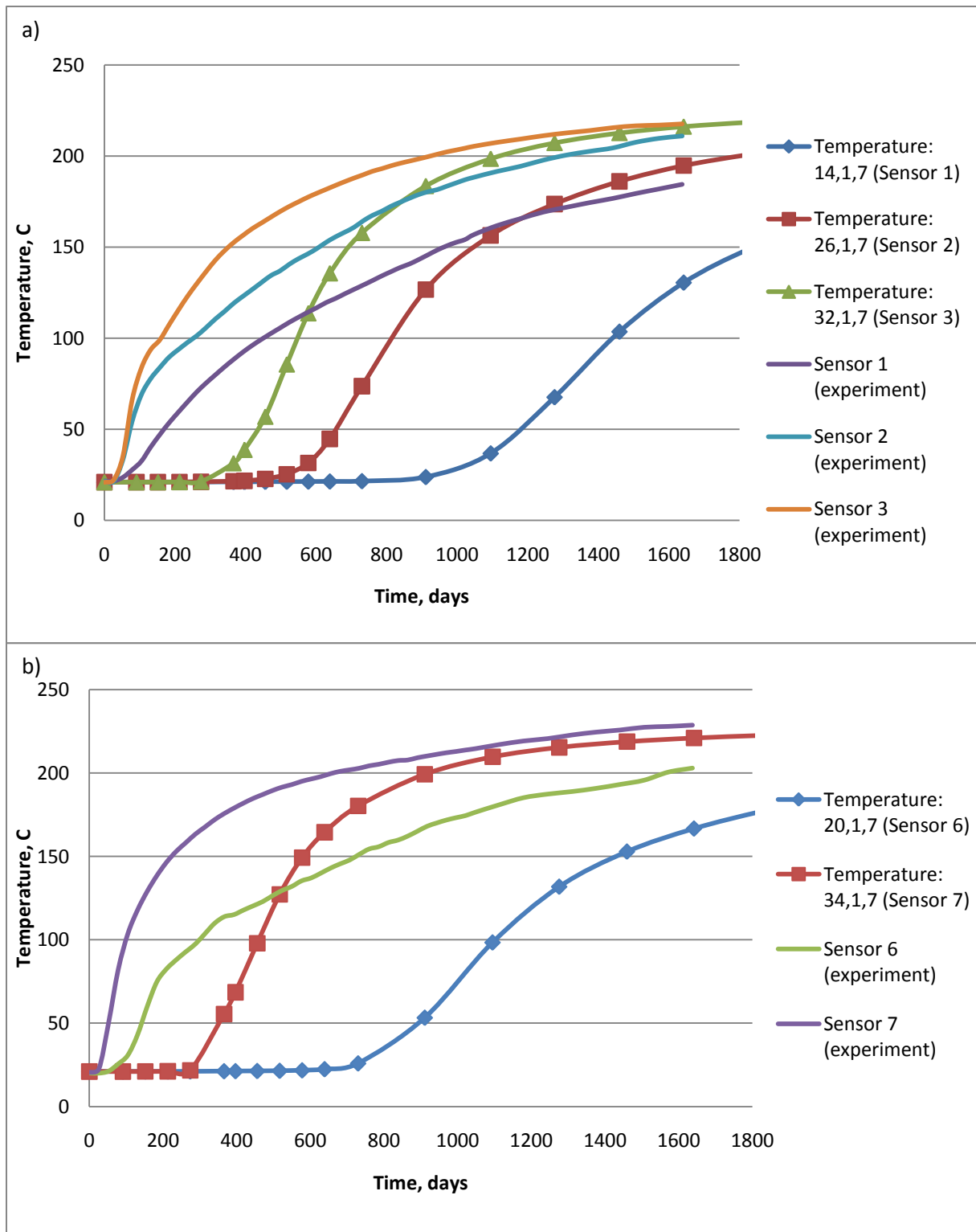
Figure 4-15: Simulation results with corresponding 3cm depth of sensors and scaled experimental results of temperature propagation in model 1 (a – Sensors 1, 2, 3; b – Sensor 6, 7)

4.2.2 Comparison of Recovery Estimation

Initial oil in place for the numerical model reservoir is 136000 m^3. To estimate recovery of the simulation run, cumulative oil production data can be taken from **Figure 4-16**.
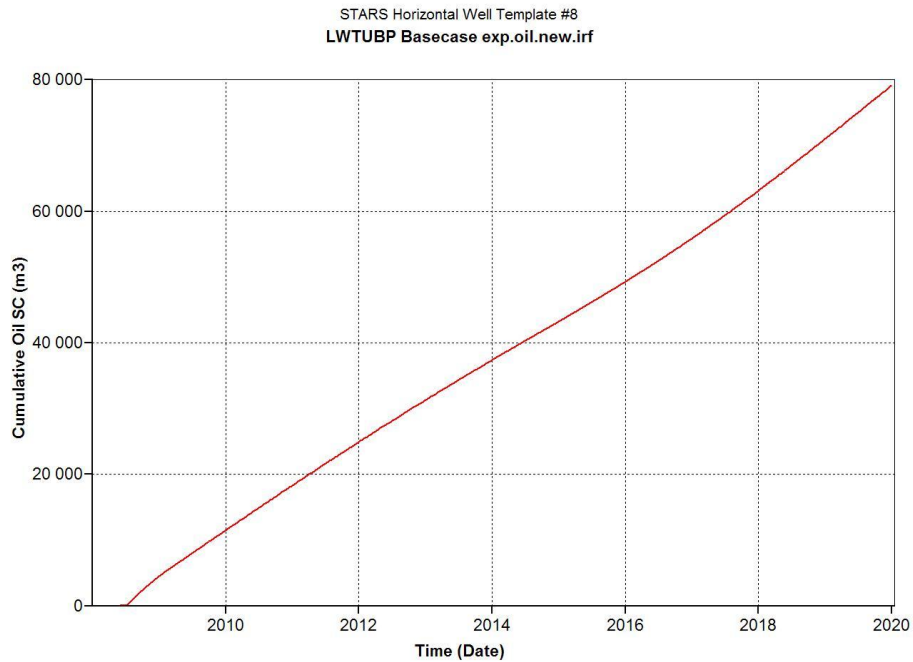
Figure 4-16: Cumulative oil produced in base case simulation

Average duration of experiments in model 1 is 200 min. Cumulative oil at 24-03-2012 (1574 days, corresponding to 200 min. of experiment time) is equal 27000 m^3 produced. Recovery then equals 0.198. This is in good agreement with the experimental results in which average recovery is equal to 0.2 after 200 min as shown in **Figure 4-17**. Dimensionless similarity is used to plot simulation results in the experimental time scale.
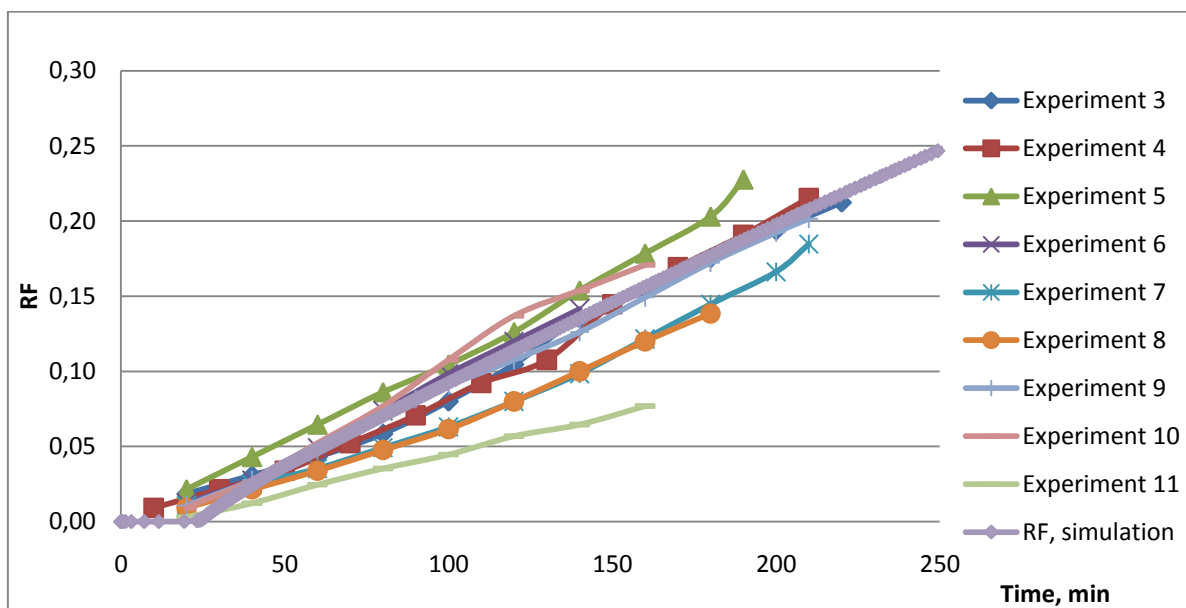
Figure 4-17: Oil recovery in experiments and simulation

Cumulative water/oil ratio is shown in **Figure 4-18** illustrating water consumption when producing a certain amount of oil. Comparison of experimental and simulated results shows that the amount of water used in the experimental study is corresponding to amount of used water in the simulated results. Cumulative water/oil ratio of the simulation is close to average results of water/oil ratio in the experimental study.
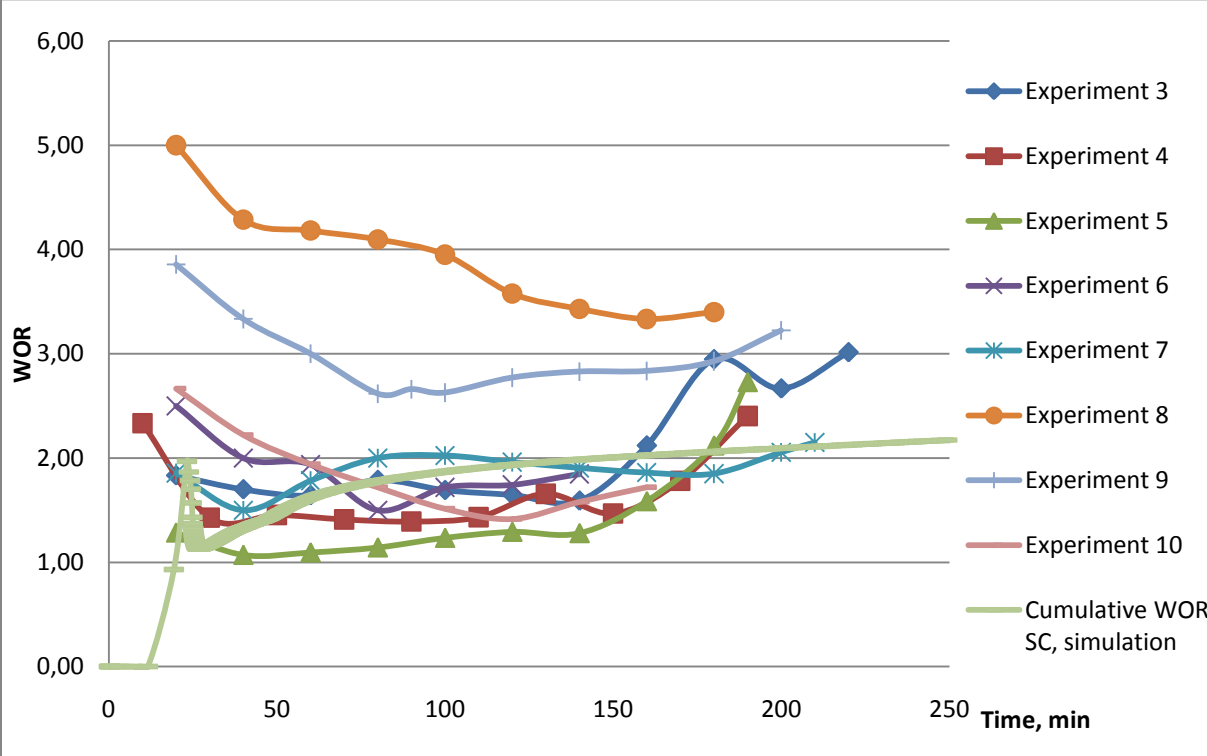
Figure 4-18: Cumulative water/oil ratio in experiments and simulation

4.3 Results of Experimental Setup Model 2

A new experimental installation is initially designed to give more flexibility to cover large areas for monitoring temperature propagation. However, due to delay in constructing the model and imperfect design and time constraint modification to the model could not be achieved. The results are not as quantitative results as aimed at. Therefore only qualitative conclusions are made based on results of experimental data this model.

4.3.1 Temperature Distribution in the Experimental Model 2

A limited number of experiments (8 experiments) are performed and shown in this thesis. Results of temperature propagation in each experiment show consistency in temperature rise for each sensor (except sensors 3 and 9 for most of experiments), as shown in **Figure 4-19 (experiment 10)**. Sensors 3 and 9 are located at the bottom of reservoir, close to production well. Sensor 9 located approximately at 12 cm from injector and sensor 3 located at 19cm from injector. It is observed during experiments that after breakthrough of the steam to the

production well, steam might propagates along the production well as in a fracture into the reservoir and brings high heat flux just above the production well, exactly in the areas of sensors 3 and 9. The temperature propagation in the areas recorded by sensors 3 and 9 is disturbing the clarity of the behavior of the rest of the sensors. Therefore the two sensors are eliminated from the **Figure 4-19**.
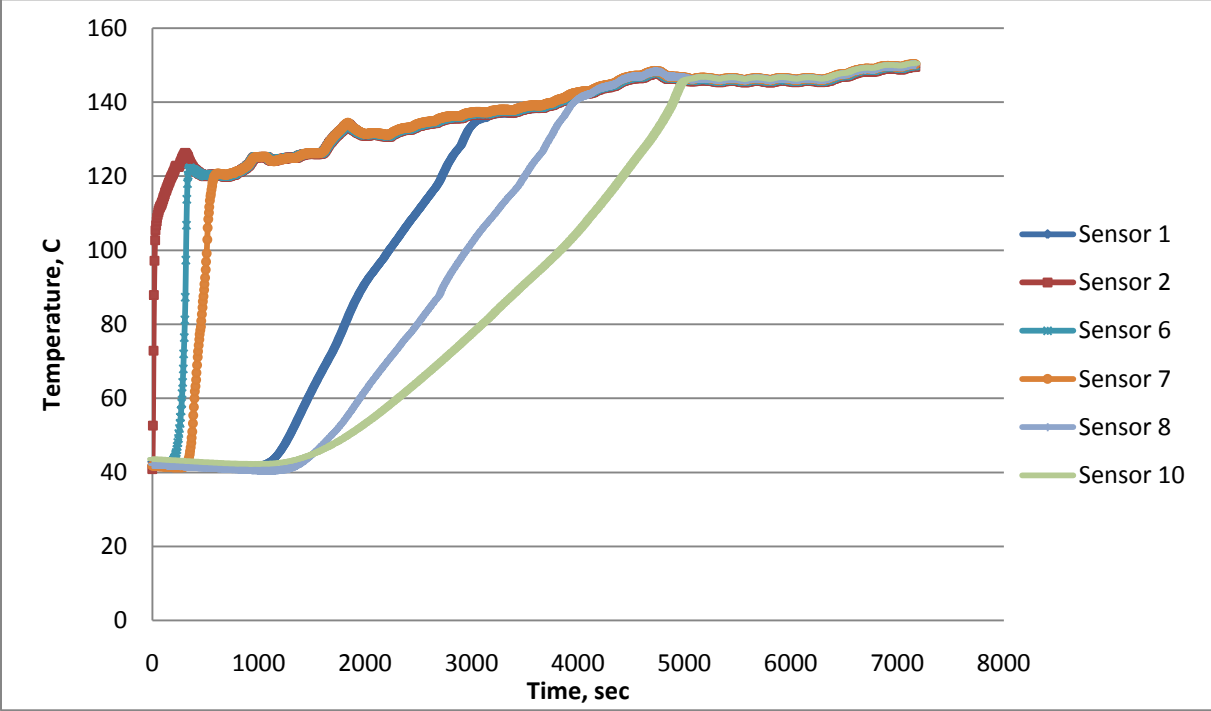
Figure 4-19: Temperature propagation in experiment 10 (model 2), both sensor 3 and sensor 9 are eliminated from the figure

Although temperature propagation in each individual experiment shows consistent results, large discrepancy are obtained when different experiments are compared, as shown in **Figure 4-20**, comparing sensor 1, as an example, in all experiments, which are divided into two sets, 4 experiments in each set. Several challenges are yet to be solved, which are the: inhomogenity of oil sand reservoir in the experimental setup model 2 within the single and different experiments. The pressure gauge that used to indicate the pressure inside the model is difficult to adjust to the same values in every experiment. The water content differs from one experiment to another which is affected by the pressure inside the model setup. All above challenges that experienced with the system as well as the time constraint made in difficult to solve all above challenges.

Though it is difficult to get quantitative results from the new system, mapping of temperature propagation from the positioned sensors and visual observation helped to confirm the proposed mechanism of steam chamber growth. Observation of temperature propagation with the time for each experiment in oil sand model 2 shows consistency for the experiments. **Figure 4-21** illustrates temperature changes in the reservoir with time in experiment 5. It can be clearly seen that steam propagates fast to the top of the reservoir, then spreads horizontally and heating the underlying layers. Heating of the reservoir from the additionally created

"source" at the top is more effective than heating in the horizontal direction from the injection point, as it might be seen that at 2000 sec. the temperature of the area of sensor 8 is much higher than at that for sensor 9 although sensor 8 has twice the distance to the injection source compared to sensor 9.
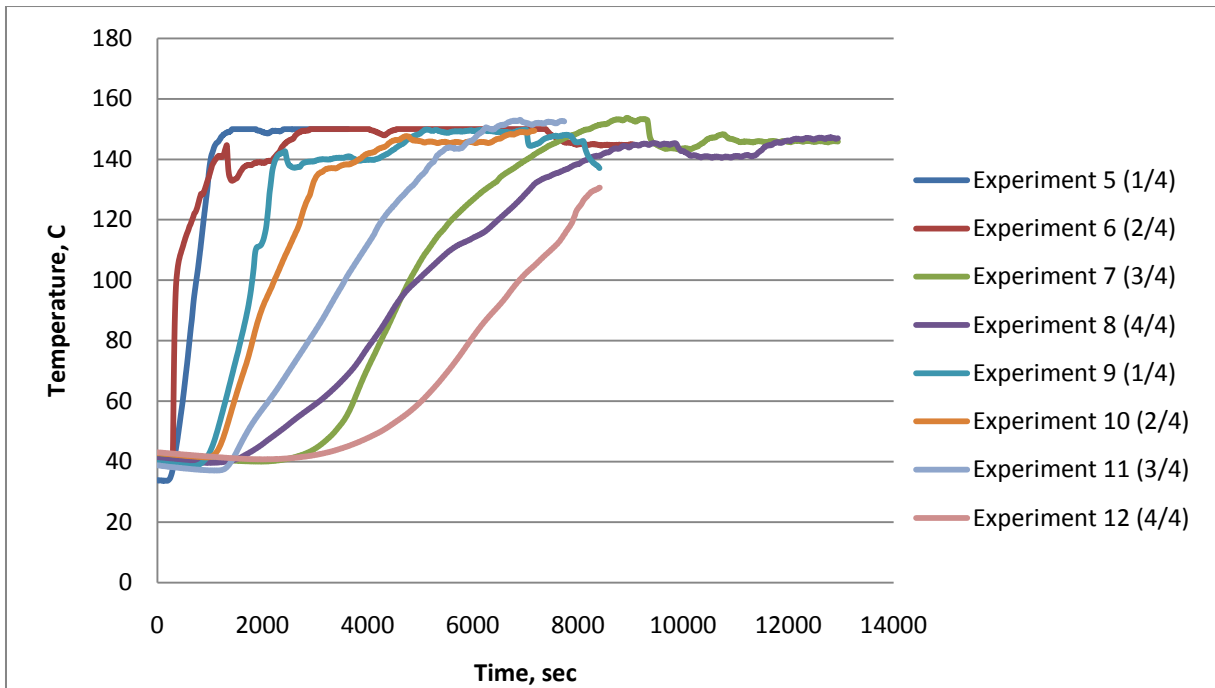

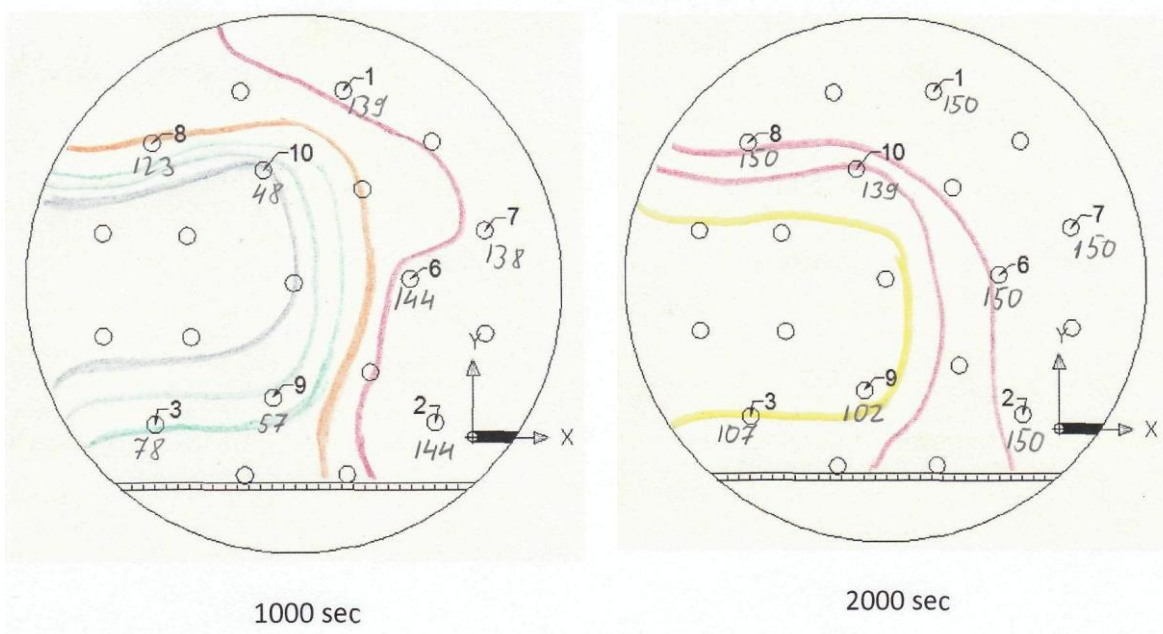**Figure 4-20: Temperature propagation with time at sensor 1 in all experiments**

Figure 4-21: Temperature distribution in experiment 5 at 1000 and 2000 sec., model 2

CHAPTER V

SUMMARY AND CONCLUSIONS

5.   SUMMARY AND CONCLUSIONS

This chapter contains summary and conclusions of the work done with experimental model 1, analytical model, numerical model and experimental model 2.

5.1 Summary

Analytical and Experimental Comparison of SAGD Models

- The geometry of the SAGD process is such that heated oil flows approximately parallel to the interface that forms a boundary between the cold reservoir and the steam-saturated zone, known as the steam chamber.
- Analytical solution of Butler's theory provides propagation of steam chamber interface, which is not realistic due to moving away of the lower part from the production well. To avoid this effect TANDRAIN assumption is used, where tangent lines plotted to the interface and anchored to the production well.
- Temperature distribution in the reservoir model 1 plotted with the assumption that all sensors are situated on one line, which is repeating middle vertical cross section of the reservoir.
- Temperature distribution with time in experimental model 1 shows that the highest temperature is observed close to the injector and in the area above it. Fast temperature propagation is observed in the horizontal plane at the top of the reservoir. In remote areas of the reservoir, temperature profiles are almost parallel to each other having almost the same slope. At about 8000 sec almost half of the oil sand volume has a temperature higher than 80 deg C.
- Comparison of analytical steam chamber interface curves and experimental temperature distribution in the model 1 shows similar trend for both, but magnitude of temperature is different and is around 20-30 deg C. Propagation of the steam chamber in experiments is slower due to non idealized conditions and some heat loss compared to the analytical solution.
- Different approaches are followed in order to match the temperature data and suggest possible mechanisms. The different approaches are dependent on the directional flow of the heat. At the start the steam chamber propagates to the top (overburden) and before moving along the overburden to the end of the model reservoir (box). The model approaches are: comparing the different temperatures that reach the sensors at the different locations and depths for heat transfer by conduction mechanism from overburden and heat transfer by conduction mechanism due to propagation from the steam injection point. The approaches provide the temperature distribution in space and time.

- Calculation of the conduction heat transfer from the overburden over estimates the temperature distribution in general. However, in the case of closest areas to the injector the temperature distribution fit better within experimental uncertainty. This is due to the the heat received from the steam injector. The better fit of the estimated temperature is due to balance between the gained temperature from the overburden and the injector source areas.
- Heat transfer by conduction from the overburden shows over estimation of the temperature in the remote areas of the reservoir. The explanation is the same as for areas close to the injector. The difference between estimated temperature based on conduction mechanisms from both sources and experimental data may be due to the balance between the insignificant temperature rise in surrounding areas and the heat loss from the flowing fluids in this area.
- Results of analytical solutions of Butler's theory and numerical modeling shows very fast steam chamber growth in the first compared to the second. However the trend of propagation is similar for both results. At an early stage the numerical model has a delayed steam chamber rise due to absence of communication between wells. Only after creating connectivity the steam chamber is starting to rise.
- Temperature gradient is used in order to indicate the magnitude of the different heat transfer mechanisms. Data from experiment 10 (1.5 cm depth) are used to determine the temperature distribution at the overburden of the experimental model box. The depth of 1.5 cm is the smallest depth that can be achieved due to the sensor configuration. The temperature gradients are constructed in the experimental model as a function of the vertical and horizontal distances, respectively at different time intervals. In spite of the complexity of the different processes taking place, consistent temperature gradients are established within the reservoir. Similar processes are occurring throughout the whole reservoir, as seen in gradient profiles for the different sensors.
- The analysis of the temperature gradient indicates that convective heat transfer contributes to heat flow ahead of the chamber at the interface, as steam chamber propagates further. The conductive heat transfer becomes more and more dominating mechanism. The analysis of temperature gradient from different heating sources shows that horizontal heating from injector is pronounced only at closest area. In rest of reservoir additionally created source of heating at top of formation is dominating in heating of underlying layers.

Experimental Model 1 and Numerical Model Comparison

- Steam chamber growth in the numerical model is similar to the experimental data trend. Steam first propagates fast in the vertical direction above the injector and then spreads at the top of the reservoir heating underlying layers. In the numerical model the angle of the steam chamber edge is more inclined relative to the horizontal compared to the experimental results. This might be explained by different relative thicknesses of the reservoirs.
- Quantitative comparison of experimental and numerical models if performed, using dimensional analysis. The dimensionless similarity between the experimental and numerical model is based on the dimensionless parameters B_3 and $t^{'}$.

- Results of comparison show that numerical model underestimates the temperature increase in the early stage of the SAGD process, the increase growing rapidly after some time and becoming identical to that of the experimental temperature propagation. In addition, time delay occurs not equally for the entire reservoir but it increases with lateral distance from injector. It may be concluded that simulation results give more reliable data for areas closer to the steam injector and production well. For remote areas, simulation shows stronger under estimation of reservoir heating with time.
- Comparison of the recovery estimation shows that numerical model is in good agreement with experimental results for average recovery.
- The amount of water used in the experimental study is proportional to the amount needed according to the simulated results. Cumulative water/oil ratio of the simulation is close to average results of water/oil ratio in the experimental study.

Results of the Experimental Model 2

- A new experimental installation is initially designed to give more flexibility to cover large areas for monitoring temperature propagation. However, due to delay in constructing the model and imperfect design and time constraint modification to the model could not be achieved. The results are not as quantitative results as aimed at. Therefore only qualitative conclusions are made based on results of experimental data this model.
- The temperature propagation in each individual experiment shows consistent results, but large discrepancy is obtained when different experiments are compared. Several challenges are yet to be solved, which are the: inhomogenity of oil sand reservoir in the experimental setup model 2 within the single and different experiments. The pressure gauge that used to indicate the pressure inside the model is difficult to adjust to the same values in every experiment. The water content differs from one experiment to another which is affected by the pressure inside the model setup.
- The observation of temperature propagation with the time for each experiment in oil sand model 2 shows consistency for all experiments. The steam propagates fast at the top of the reservoir, spreading horizontally. Heating of the reservoir from the additionally created source at the top is more effective than heating in the horizontal direction from the injection point.

5.2 Conclusions

1. Experimental study of temperature propagation shows that steam/temperature propagates fast to the top of the reservoir and then spreads horizontally away from the vertical injection plane. The top of the reservoir becomes an additional heating source for underlying layers.
2. Butler's theory calculation for steam chamber interface propagation shown to over predict rates of temperature growth compared to experimental measurements. However, the propagation trend of the analytical solution is very similar to the experimental results.
3. Approaches with different heating sources, created in the reservoir give explanation of mechanisms of heat transfer in different areas of the reservoir. Area close to the injector gain heat from the overburden and from the injector source areas. For areas further away from steam source conduction heating from the overburden dominates, and conduction heating from injector source insignificant.
4. The analysis of the experimental temperature gradient for different sensors indicates that convective heat transfer contributes to the heat flow ahead of the steam chamber at the interface. As the steam chamber develops further into the reservoir, conductive heat transfer becomes more dominating.
5. Numerical simulation scaled to the experimental study shows a similar trend of steam chamber growth. This is observed during experiments. Analysis of numerical results shows that simulator gives better fit to the experimental data at areas closer to injection well. With increasing horizontal distance from well pair results show higher deviation from experimental measurements.
6. Comparison of recovery estimation and water consumption between numerical and experimental model shows good agreement. Numerical model provide reliable results of simulation of these parameters.
7. Results of the experimental model 2 confirm our proposed mechanism of steam chamber growth during SAGD process. Continuous steam injection creates additional heating "source" at the top of reservoir, which in remote area is dominating source for the heating of the underlying layers.

REFERENCES

1. Aziz, K., Settari, A.: "Petroleum Reservoir Simulation," Applied Science Publishers, New York & London, p. 476, 1979.

2. Baker, R., Fong, C., Li, T., Bowes, C., Toews, M.: "Practical Considerations of Reservoir Heterogeneities on SAGD Projects", paper SPE 117525, presented at the 2008 SPE International Thermal Operations and Heavy Oil Symposium, Calgary, Alberta, Canada, October 20-23, 2008.

3. Butler, R. M., Petela, G.: "Theoretical Estimation of Breakthrough Time and Instantaneous Shape of Steam Front During Vertical Steamflooding", AOSTRA, Journal of Research, Volume 5, Number 4, pp. 359-381, Fall 1989.

4. Butler, R. M., Stephens, D. J.: "The Gravity Drainage on Steam Heated Heavy Oil to Parallel Horizontal Wells", Jour. Of Canadian. Pet. Tech., April-June 1981. pp 90-96.

5. Butler, R. M.: "Rise of Interfering Steam Chambers", Jour. Of Canadian. Pet. Tech., Paper 87-03-07, June 1987.

6. Butler, R. M.: "SAGD Comes of AGE!", Jour. Of Canadian. Pet. Tech., Volume 37, No.7, July, 1998.

7. Butler, R. M.: "Some Recent Development in SAGD", Jour. Of Canadian. Pet. Tech., Volume 40, No.1, January, 2001.

8. Butler, R. M.: "Steam-assisted Gravity Drainage: Concept, Development and Future", Jour. Of Canadian. Pet. Tech., Volume 33, No. 2, February, 1994.

9. Butler, R.M.: "Thermal Recovery of Oil and Bitumen", Prentice Hall Publishing Company, New Jersey, 1991.

10. Canadian Centre for Energy Information, www.centreforenergy.com, 2011.

11. Clark, B.: "Heavy Oil", Working Document of the NPC Global Oil and Gas Study, Made Available July 18, 2007.

12. CMG STARS User's Guide Advanced Process and Thermal Reservoir Simulator, Version 2009, Computer Modelling Group Ltd., Calgary, Alberta, Canada, 2009.

13. CMG WinProp User's Guide Phase Property Program, Version 2009, Computer Modelling Group Ltd., Calgary, Alberta, Canada, 2009.

14. Deng, X.:"Recovery Performance and Economics of Steam/Propane Hybrid Process", Alberta Research Council, SPE/PS-CIM/CHOA 97760, paper presented at the 2005 SPE International Thermal Operations and Heavy Oil Symposium, Calgary, Alberta, November 1-3, 2005.

15. Edmunds, N. R., Gittins, S. D.: "Effective Application of Steam Assisted Gravity Drainage of Bitumen to Long Horizontal Well Pairs", Jour. Of Canadian. Pet. Tech., Volume 32, No. 6, June, 1993.

16. Edmunds, N. R., Kovalsky, J. A., Gittins, S. D., Pennacchioli, E. D.: "Review of Phase A Steam-Assisted Gravity-Drainage Test", paper SPE 21529 presented at the 1991 SPE Intl. Thermal Operations Symposium, Bakersfiled, February 7-8, 1991.

17. Egermann, P., Renard, G., Delamaide, E.: "SAGD Performance Optimization through Numerical Simulations: Methodology and Field Case Example", paper SPE 69690 presented at the SPE International Thermal Operations and Heavy Oil Symposium, Porlamar, Margarita Island, Venezuela, March 12-14, 2001.

18. Farouq-Ali, S. M.: "Is there life After SAGD?", Distinguished Authors Series, Jour. Of Canadian. Pet. Tech., June, 1997.

19. Flint, L.: Bitumen Recovery Technology, A Review of Long Term R&D Opportunities, Lenef Consulting, 1/31/05 (BRT), NRCAN, Natural Resources Canada, 2005.

20. Gabitto, J., Barrufet, M.: "Experimental and Theoretical Determination of Heavy oil Viscosity Under Reservoir Conditions", Final Progress Report, Texas A&M University, 2003.

21. Gates, I.D., Chakrabarty, N.: "Optimization of Steam-Assisted Gravity Drainage in McMurray Reservoir", paper 2005-193 presented at the Petroleum Society's 6th Canadian International Petroleum Conference (56th Annual Technical Meeting), Calgary, AB, June 7-9, 2005.

22. Good, W. K., Scott, J. D., Luhning, R. W.: "Review And Assessment of Steam Assisted Gravity Drainage (SAGD) Applications in Canada", proceeding of the 14th World Petroleum congress in 1994, published by John Wiley & Sons. pp 417-426, 1994..

23. Government of Alberta, Energy, "Oil Sands Glossary" http://www.energy.alberta.ca/OilSands/1708.asp, 2011.

24. Green, D. W., Willhite, G. P.: "Enhanced Oil Recovery" Henry L. Doherty Memorial Fund of AIME, Society of Petroleum engineers, Richardson, Texas, 1998.

25. http://www.heavyoilinfo.com/blog-posts/worldwide-heavy-oil-reserves-by-country/

26. Ibatullin, T., Zolotukhin, A. B.: "Optimization of Solvent-Based Enhancements of Steam Assisted Gravity Drainage", presented at 15th European Symposium of Improved Oil Recovery, Paris, France, April 27-29, 2009.

27. Industrikjemikalier AS Mitco. 2008. *www.pib.no/Printx.aspx?Ctrls/HmsPageCtrl&di=1053* (accessed 29 April 2008)

28. Ito, Y., Ipek, G.: "Steam-Fingering Phenomenon During SAGD Process", SPE/PS-CIM/CHOA 97729 PS2005-324, paper presented at the 2005 SPE International Thermal Operations and Heavy Oil Symposium, Calgary, Alberta, Canada, November 1-3, 2005.

29. Ito, Y., Suzuki, S.: "Numerical Simulation of the SAGD Process in the Hangingstone Oil Sand Reservoir", presented at the 47th Annual Technical Meeting, June 10-12, 1996 Calgary, Alberta, Jour. Of Canadian. Pet. Tech., September Volume 38, No.9, pp 27-35, 1999.

30. Kamath, V. A., Sinha, S., Hatzignatiou, D. G.,: "Simulation Study of Steam-Assisted Gravity Drainage Process in Ugnu Tar Sand Reservoir", paper SPE 26075, presented at the 1993 Western Regional Meeting, Anchorage, Alaska, USA, May 26-28, 1993.

31. Kisman, K. E., Yeung, K. C.: "Numerical Study og the SAGD Process in the Burnt Lake Oil Sands Lease", paper SPE 30276 presented at the SPE International Heavy Oil Symposium, Calgary, AB, June 19-21, 1995.

32. Krumbein, W. C., Monk, G. D.: "Permeability as a function of the Size Parameters of Unconsolidated Sand", paper SPE-943153, presented at Los-Angeles Meeting, October 1942.

33. McCormack, M.: "Mapping of the McMurray Formation for SAGD", Jour. Of Canadian. Pet. Tech., Volume. 40, No. 8, August 2001.

34. Miller, K. A.: "Heavy Oil and Bitumen – not Glamorous, but Often Profitable", Jour. Of Canadian. Pet. Tech., Volume 33, No. 4, April 1994.

35. Nasr, T. N., Law, D. H-S., Good, W. K.: "Field Scale Numerical Simulation of SAGD Process With Top-Water Thief Zone", paper presented at the Canadian International Petroleum Conference, June 4-8, 2000. (in press with the Jour. Of Can. Pet. Tech., August, 2003.)

36. NEB *Canada's Oil Sands Opportunities and Challenges to 2015: An Update*. National Energy Board of Canada. (Retrieved 2006-10-30)

37. Ong, T.S., Butler, R. M.: "Wellbore Flow Resistance in Steam-Assisted Gravity Drainage", Jour. Of Canadian. Pet. Tech., Volume. 29, No. 6, pp. 49-55, November-December, 1990.

38. Prats, M.: "Thermal Recovery", Monograph Henry L. Doherty Series, SPE, Dallas, 7, 14-15, Texas, 1986.

39. Priyadi, Y., "Thermal Recovery of Heavy Oil by SAGD", Master's thesis, University of Stavanger, June, 2008.

40. Reis, J-C.: "A Steam-assisted Gravity Drainage Model for Tar Sands: Linear Geometry", Jour. Of Canadian Pet. Tech., 31, No. 10, pp. 14-20, 1992.

41. Romanov, A., Hamouda, A. A.: "Heavy Oil Recovery by Steam Injection, Mapping of Temperature Distribution in Light of Heat Transfer Mechanisms", paper was prepared for a presentation presented at the SPE Asia Pacific Oil and Gas Conference and Exhibition held in Jakarta, Indonesia, September 20-22, 2011.

42. Shin, H., Polikar, M.: "Review of Reservoir Parameters to Optimize SAGD and Fast-SAGD Operating Conditions", Jour. Of Canadian. Pet. Tech., Volume 46, No. 1. January, 2007.

43. Singhal, A. K., Ito, Y., Kasraie, M.: "Screening and Design Criteria for Steam Assisted Gravity Drainage (SAGD) Projects", SPE 50410, SPE Int. Conf. on Hor. Well Tec., Calgary, Canada, November, 1998.

44. Syncrude Canada ltd, "Oil Sands history" http://www.syncrude.ca/users/folder.asp?FolderID=5657, 2010.

45. Taber, J. J., Martin, F. D., and Seright, R. S.: "EOR Screening Criteria Revisited", paper SPE 35385 presented at the 1996 SPE Improved Oil Recovery Symposium, Tulsa , OK, April 21-24, 1996.

46. The Engineering Toolbox website, www.EngineeringToolbox.com, 2011.

APPENDIX
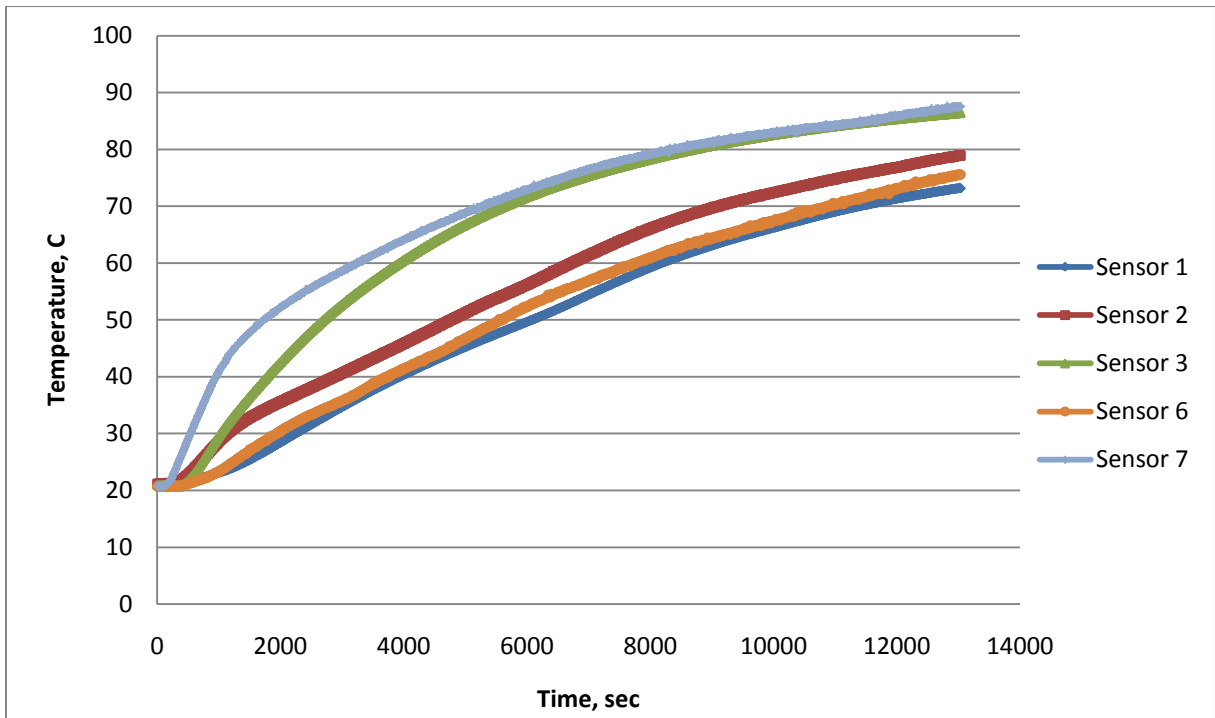
Figure 1: Temperature propagation in experiment 3 (5 cm depth of sensors), model 1
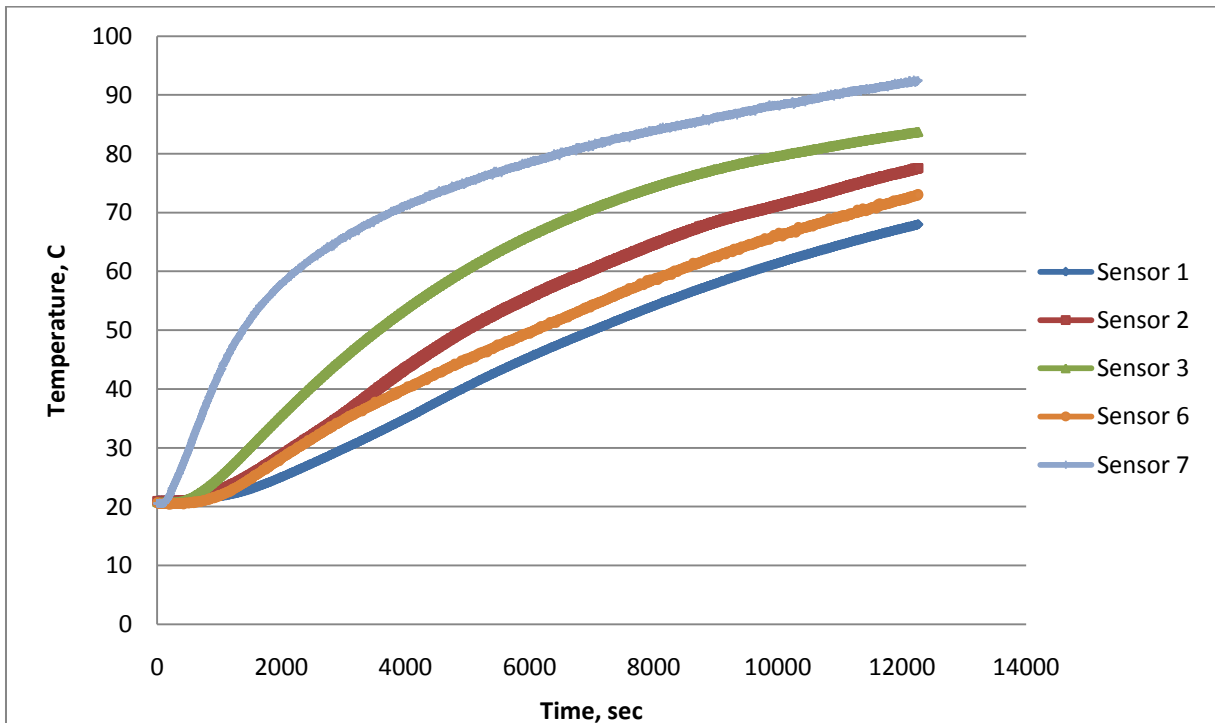
Figure 2: Temperature propagation in experiment 7 (6.5 cm depth of sensors), model 1
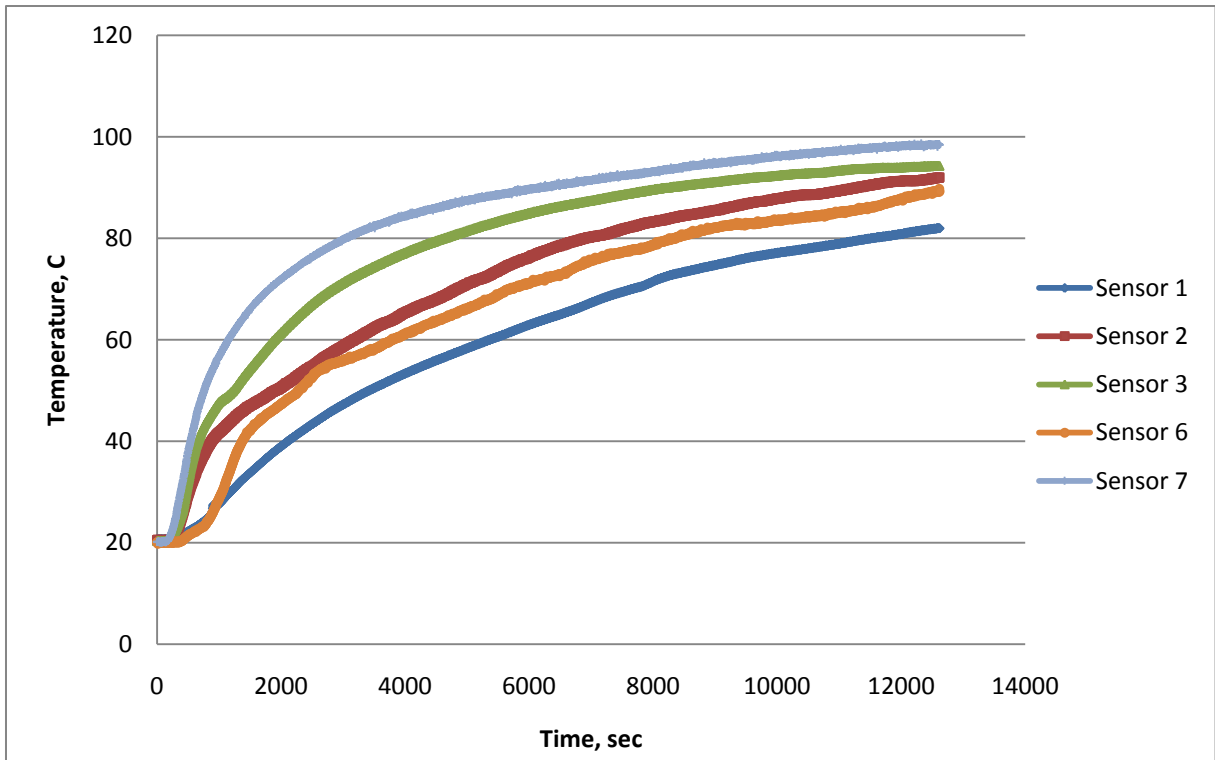
Figure 3: Temperature propagation in experiment 9 (3 cm depth of sensors), model 1
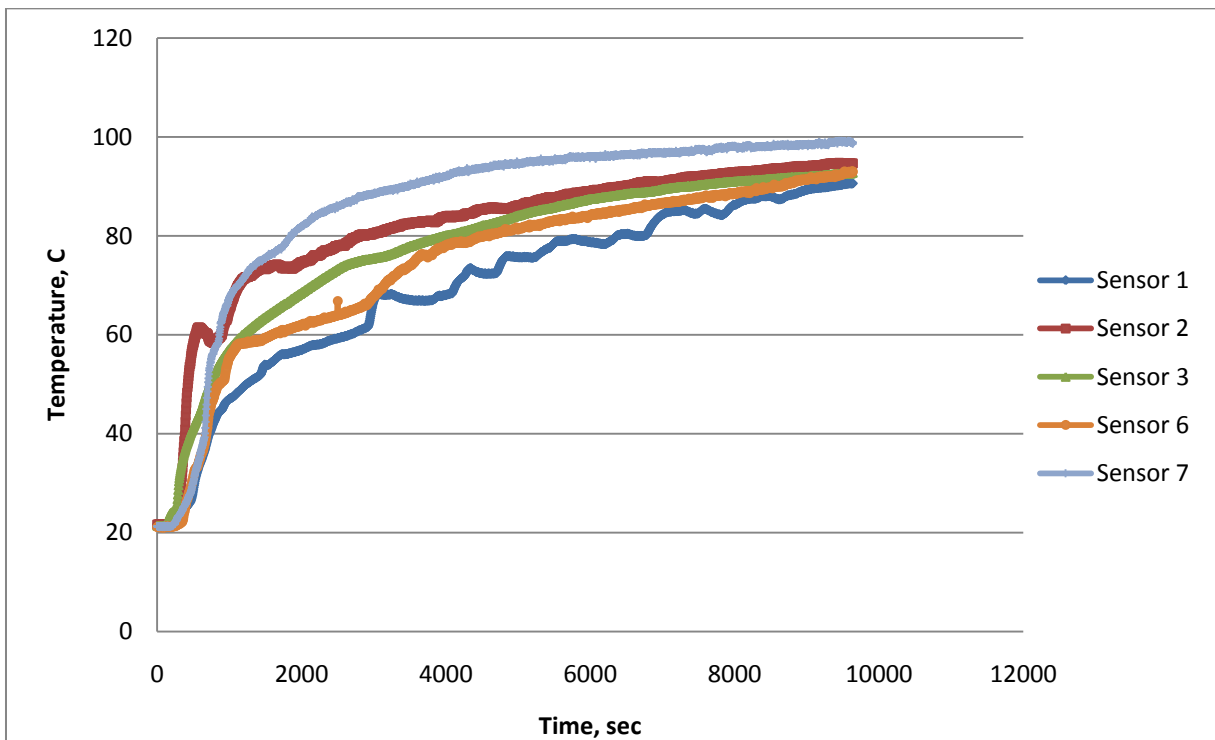
Figure 4: Temperature propagation in experiment 10 (1.5 cm depth of sensors), model 1
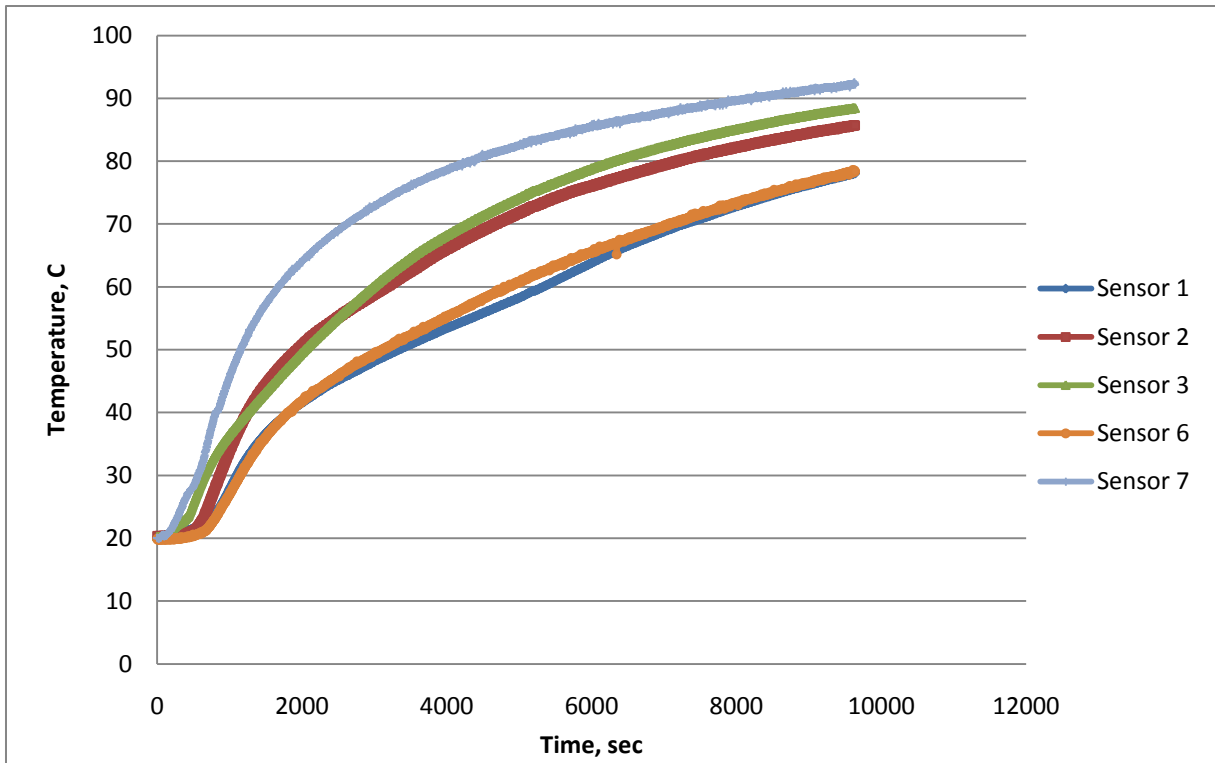
Figure 5: Temperature propagation in experiment 11 (4 cm depth of sensors), model 1
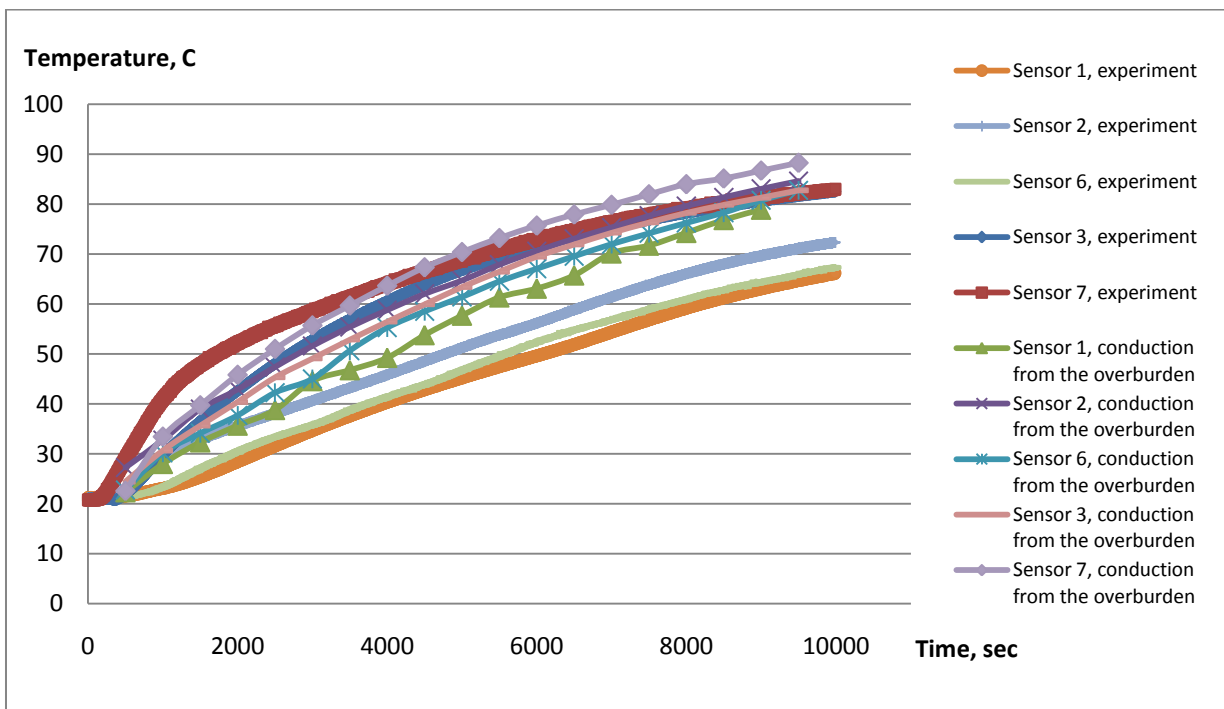
Figure 6: Comparison between temperature measurements as a function of time at 5 cm depth in the experiment 3 and estimated temperature by conduction from the overburden
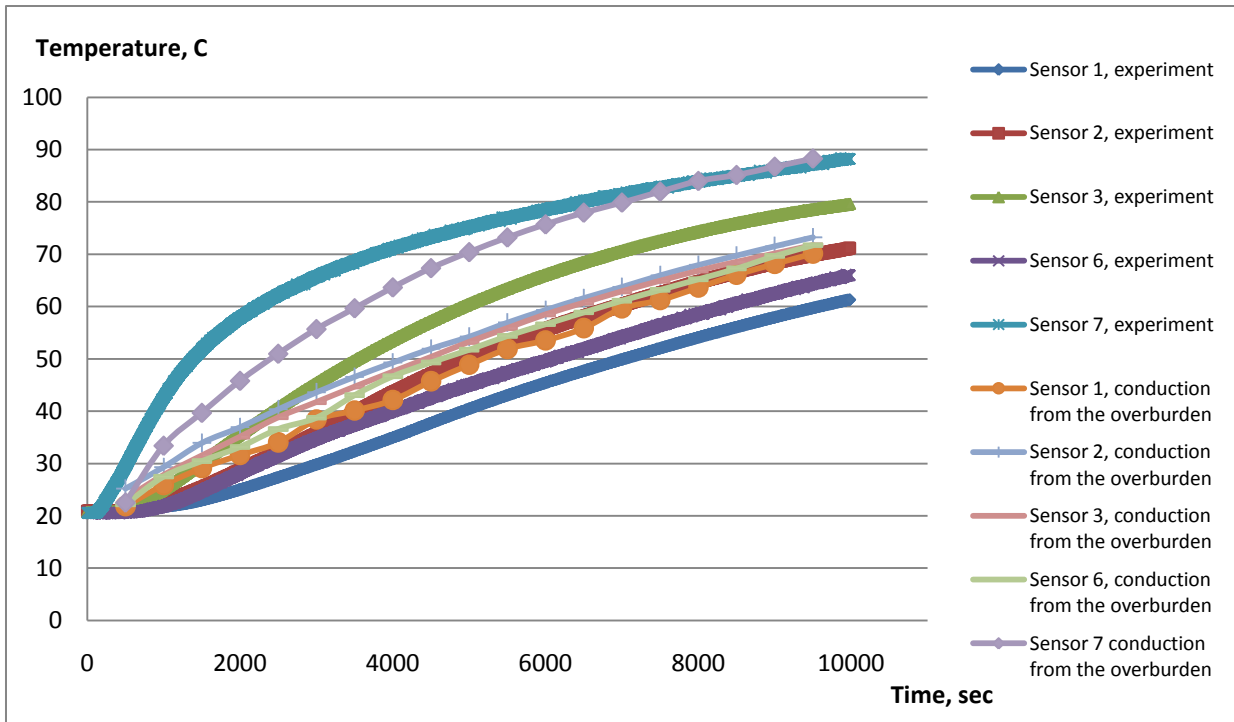
Figure 7: Comparison between temperature measurements as a function of time at 6.5 cm depth in the experiment 7 and estimated temperature by conduction from the overburden
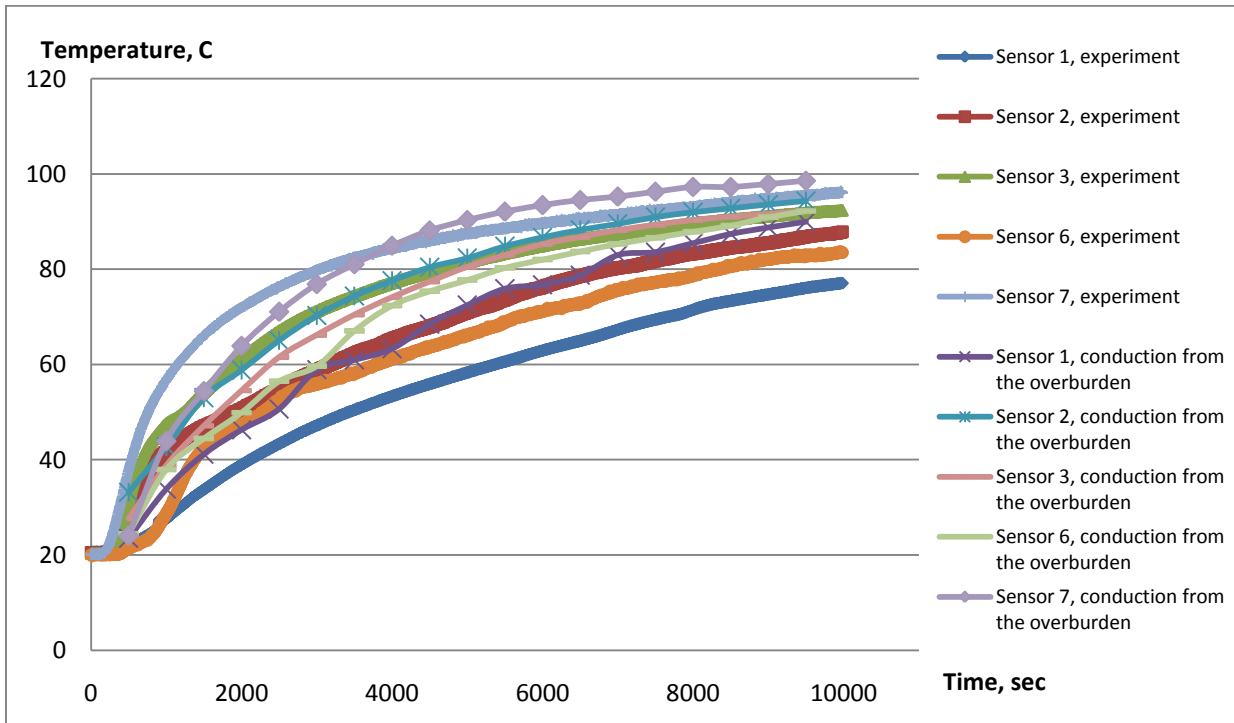
Figure 8: Comparison between temperature measurements as a function of time at 3 cm depth in the experiment 9 and estimated temperature by conduction from the overburden
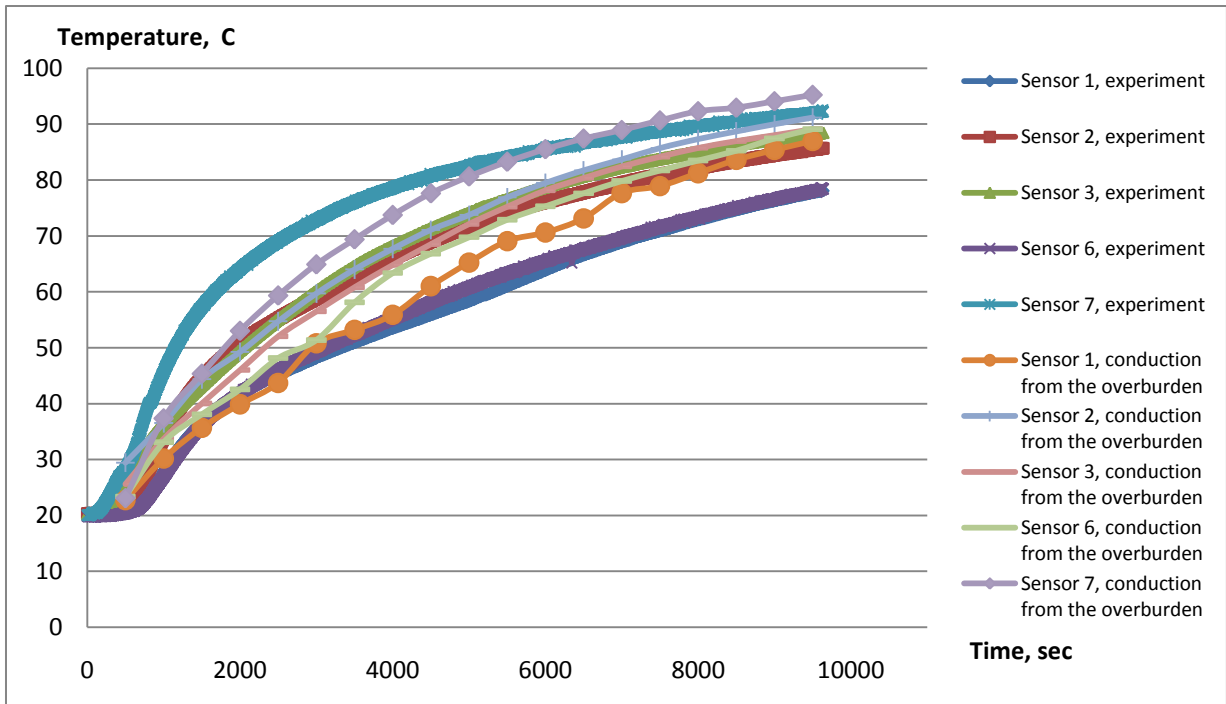
Figure 9: Comparison between temperature measurements as a function of time at 4 cm depth in the experiment 11 and estimated temperature by conduction from overburden
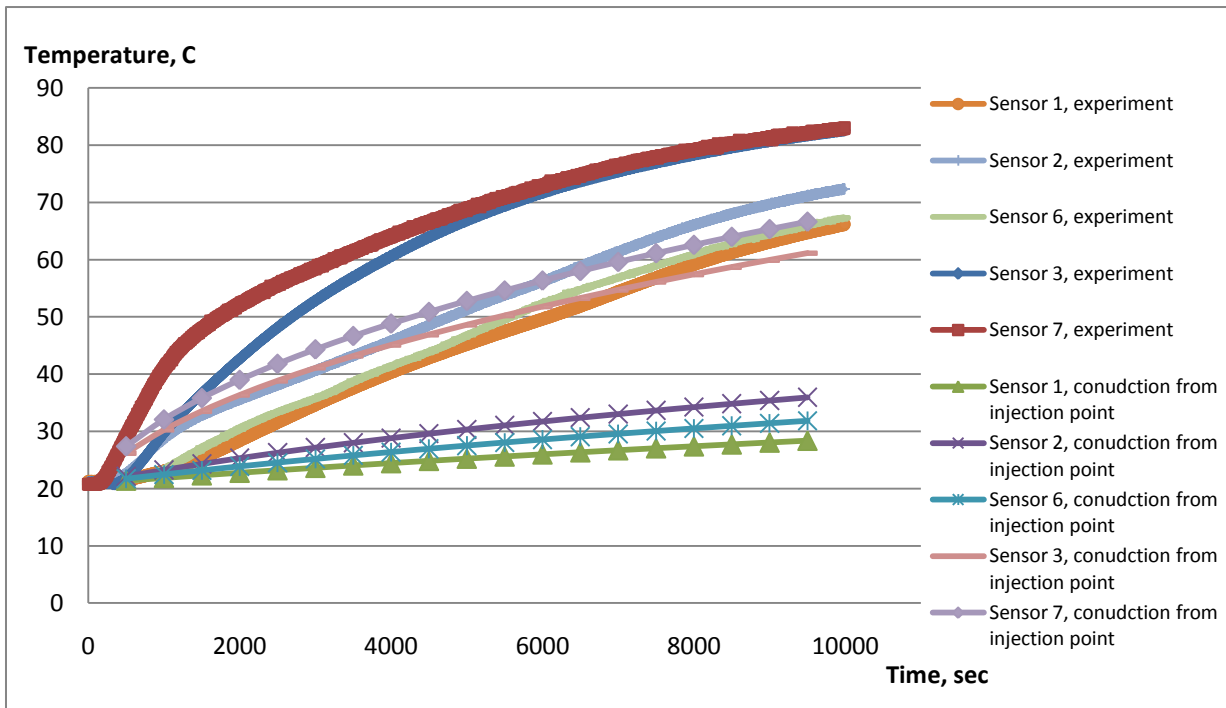
Figure 10: Comparison between temperature measurements as a function of time at 5 cm depth in the experiment 3 and estimated temperature by conduction from injection point
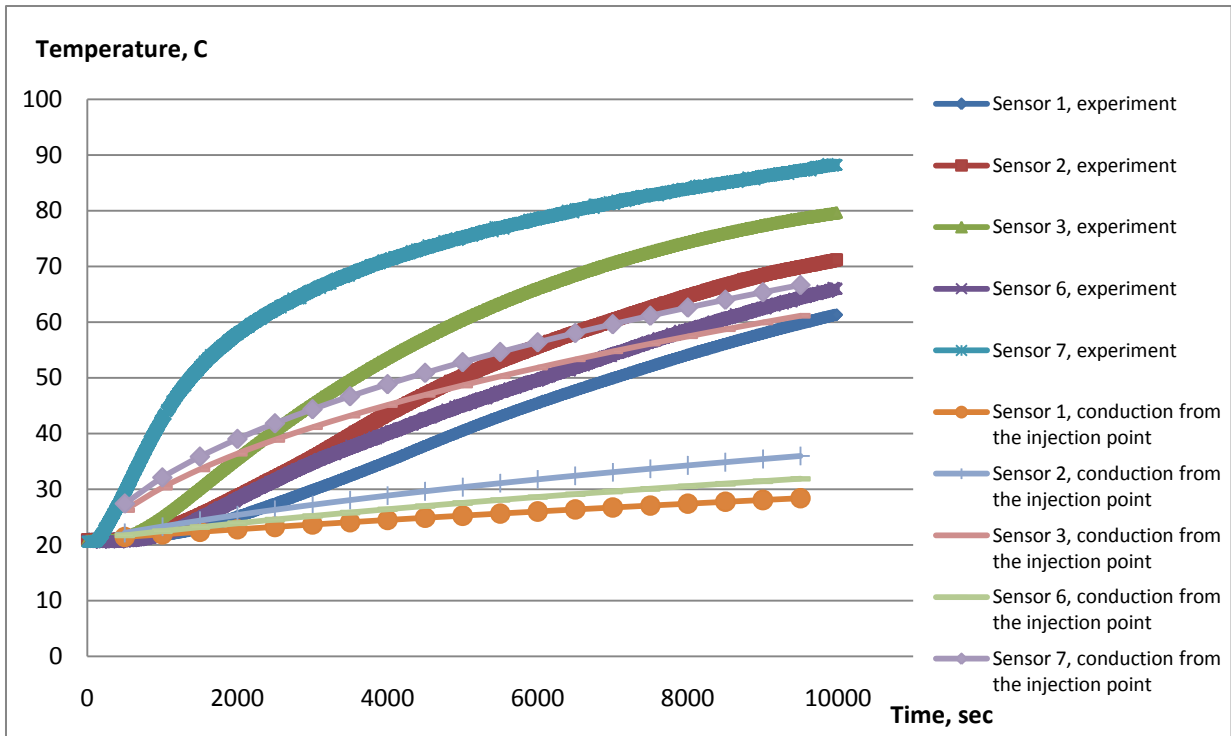
Figure 11: Comparison between temperature measurements as a function of time at 6.5 cm depth in the experiment 7 and estimated temperature by conduction from injection point
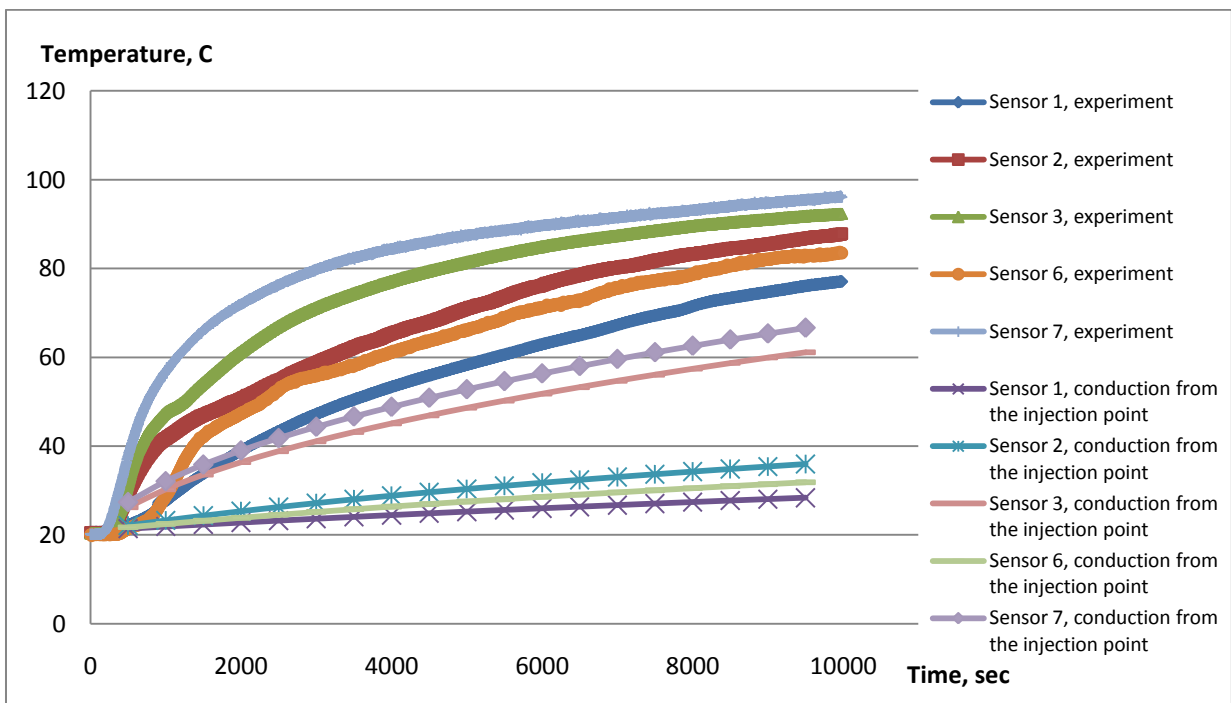
Figure 12: Comparison between temperature measurements as a function of time at 3 cm depth in the experiment 9 and estimated temperature by conduction from injection point
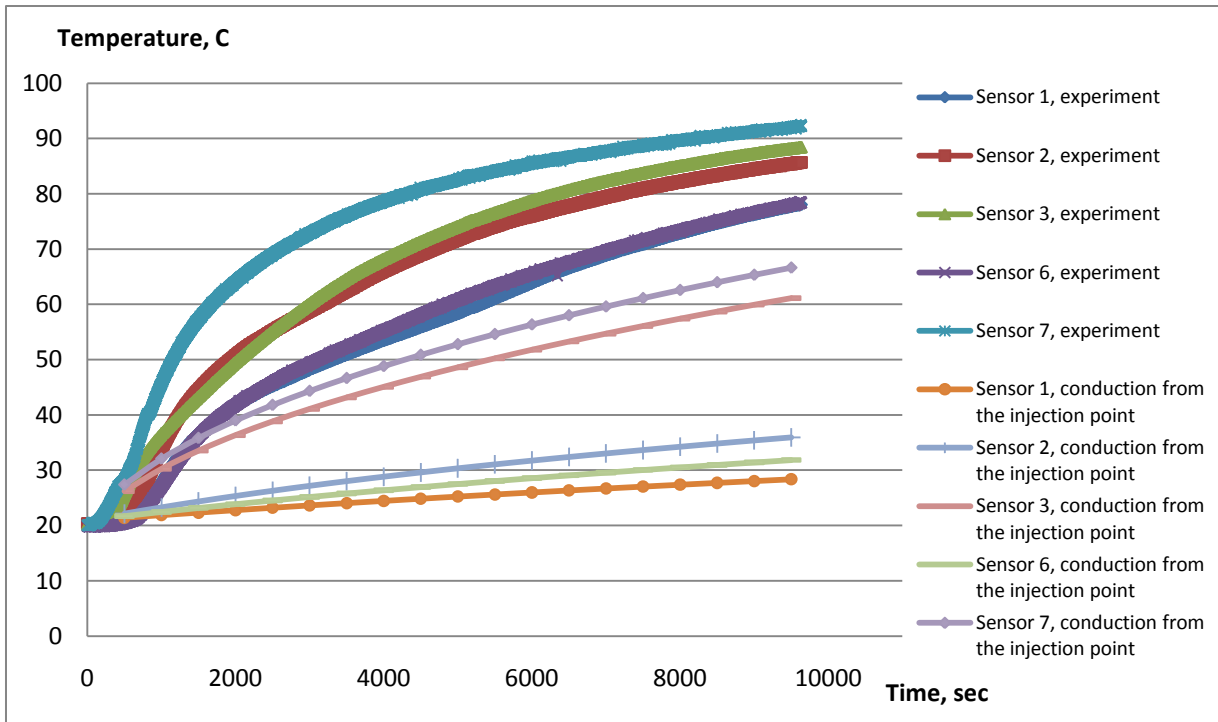
Figure 13: Comparison between temperature measurements as a function of time at 4 cm depth in the experiment 11 and estimated temperature by conduction from injection point
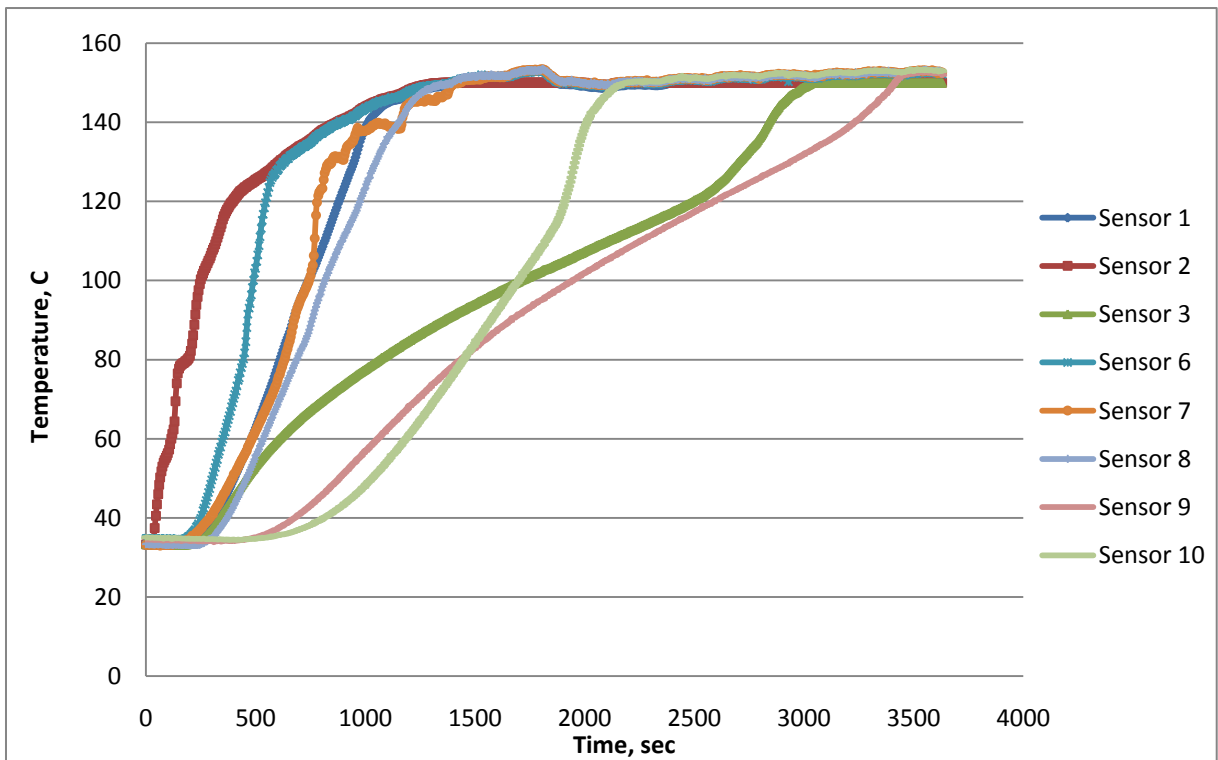
Figure 14: Temperature propagation in experiment 5, model 2
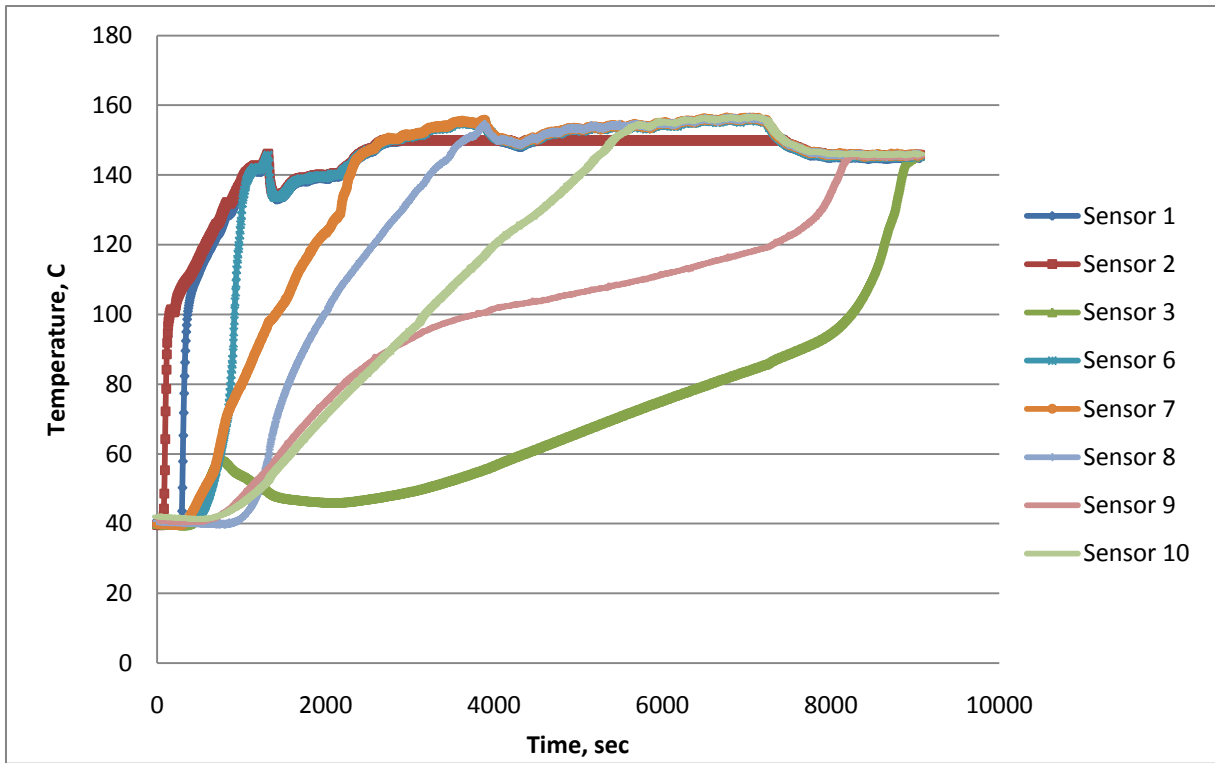
Figure 15: Temperature propagation in experiment 6, model 2
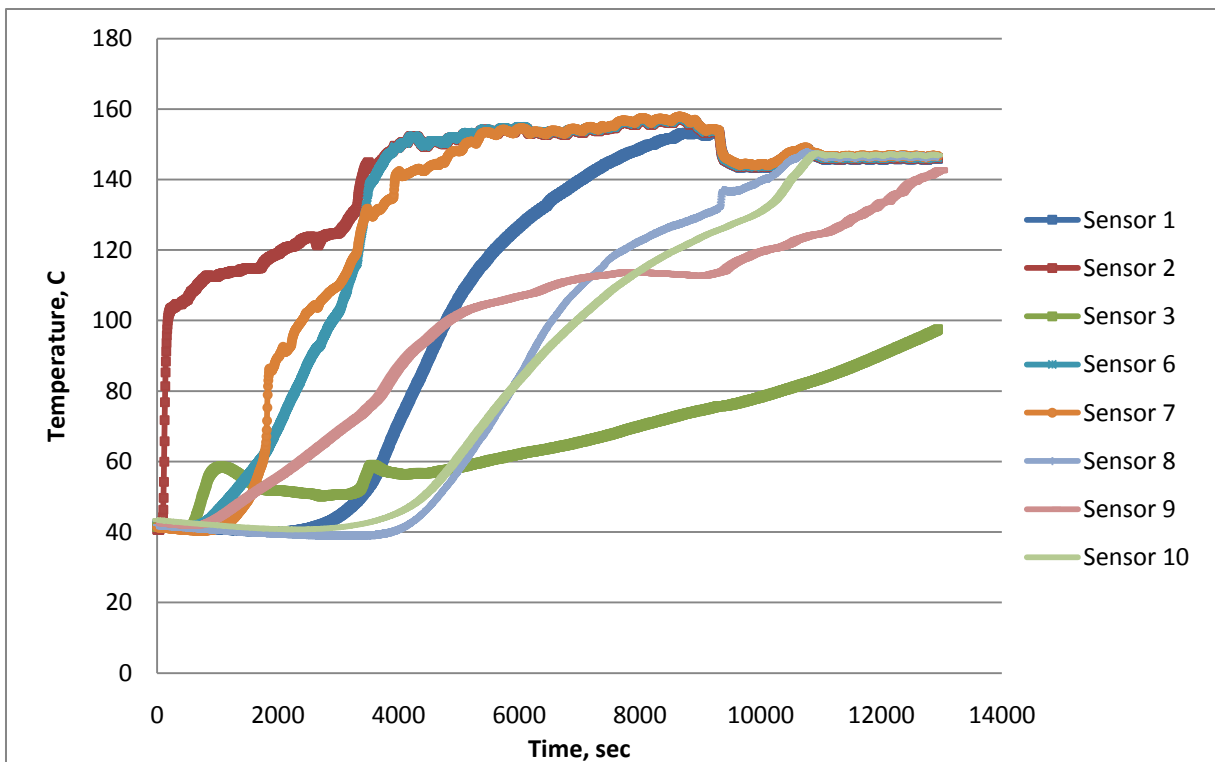
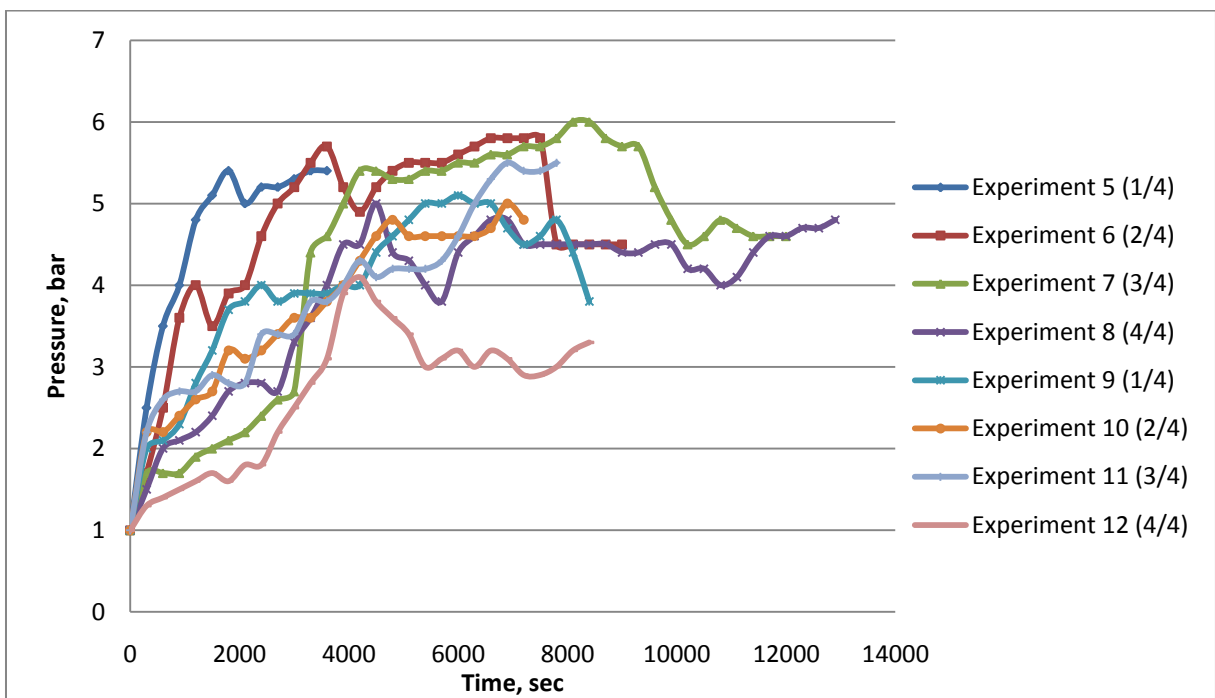**Figure 16: Temperature propagation in experiment 7, model 2**
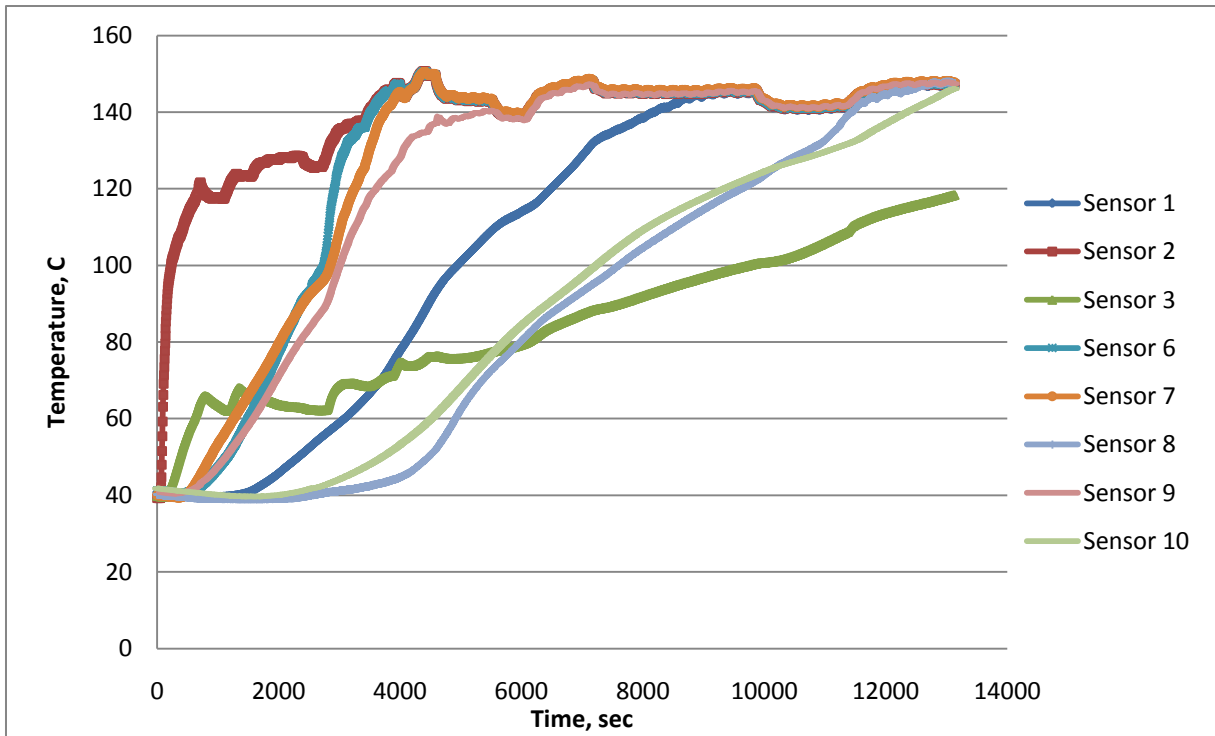
Figure 17: Temperature propagation in experiment 8, model 2
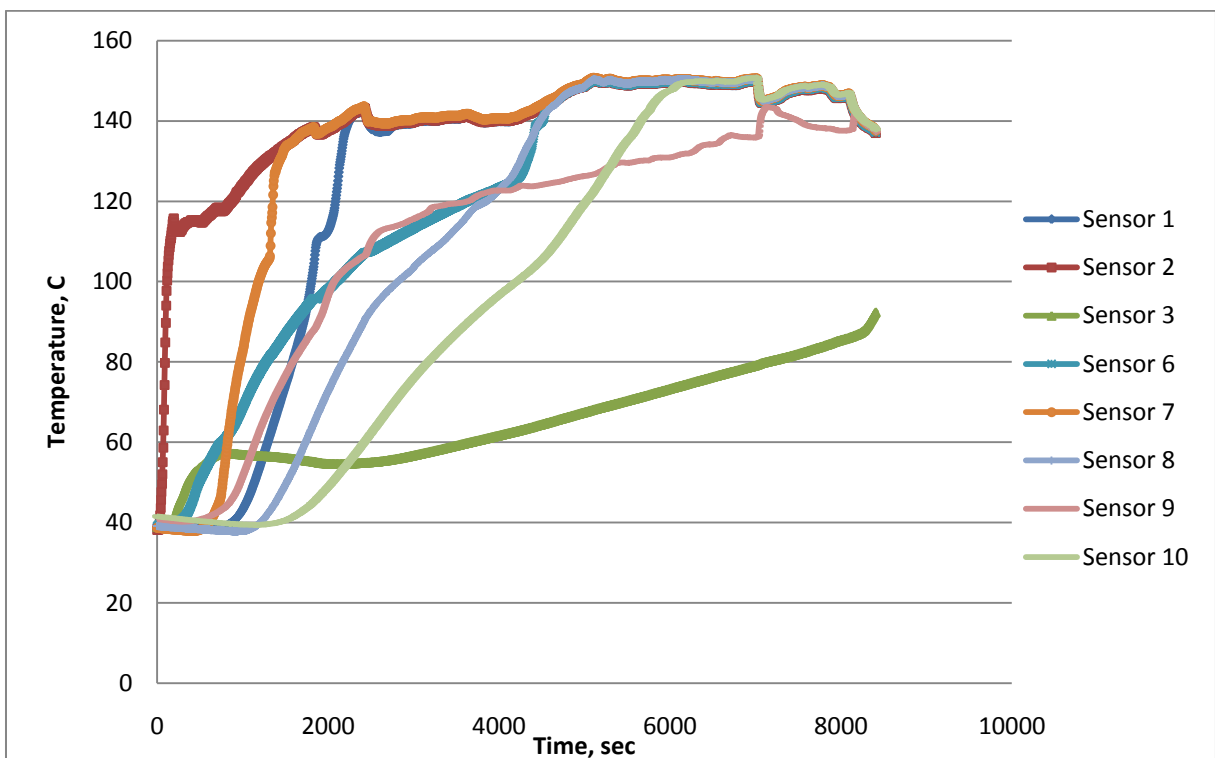
Figure 18: Temperature propagation in experiment 9, model 2
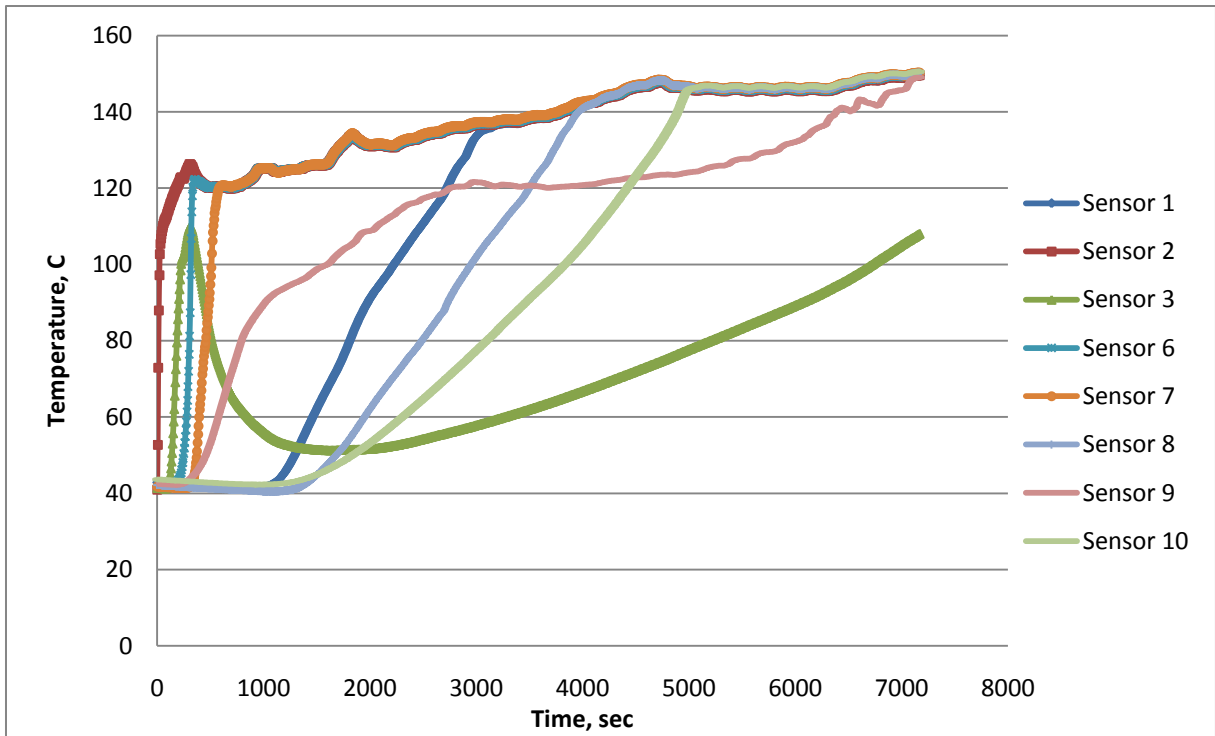
Figure 19: Temperature propagation in experiment 10, model 2
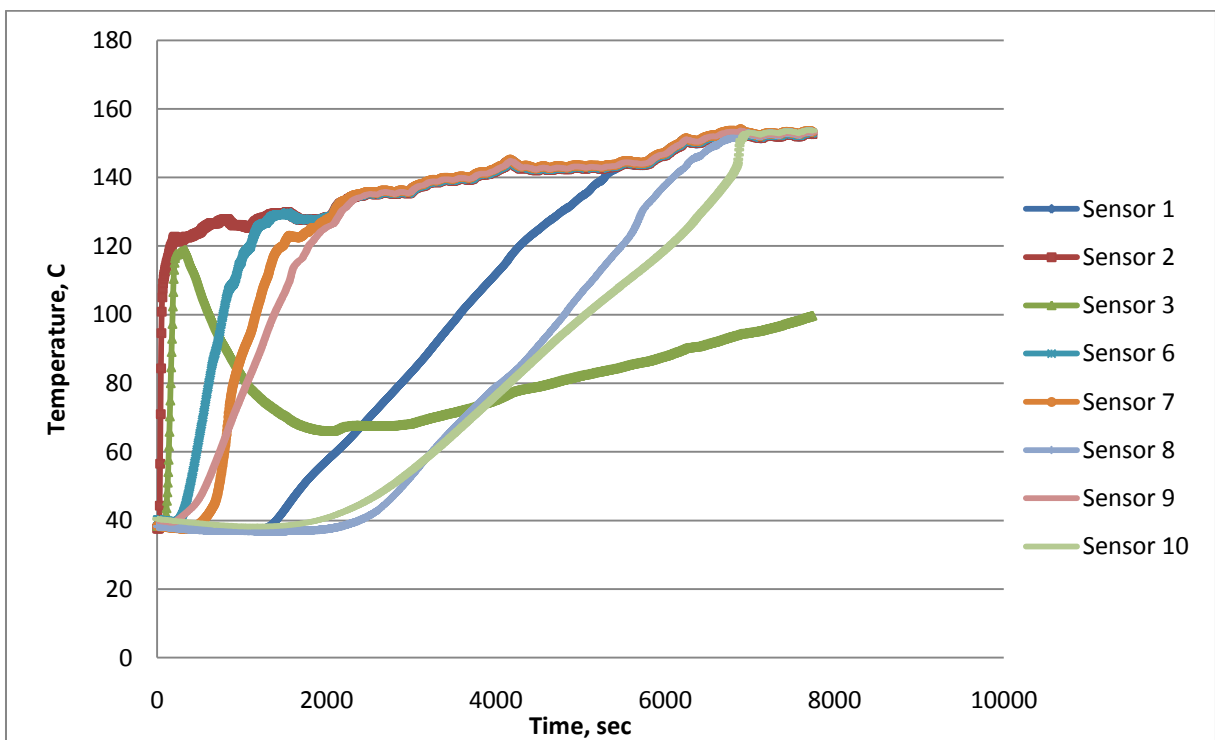
Figure 20: Temperature propagation in experiment 11, model 2
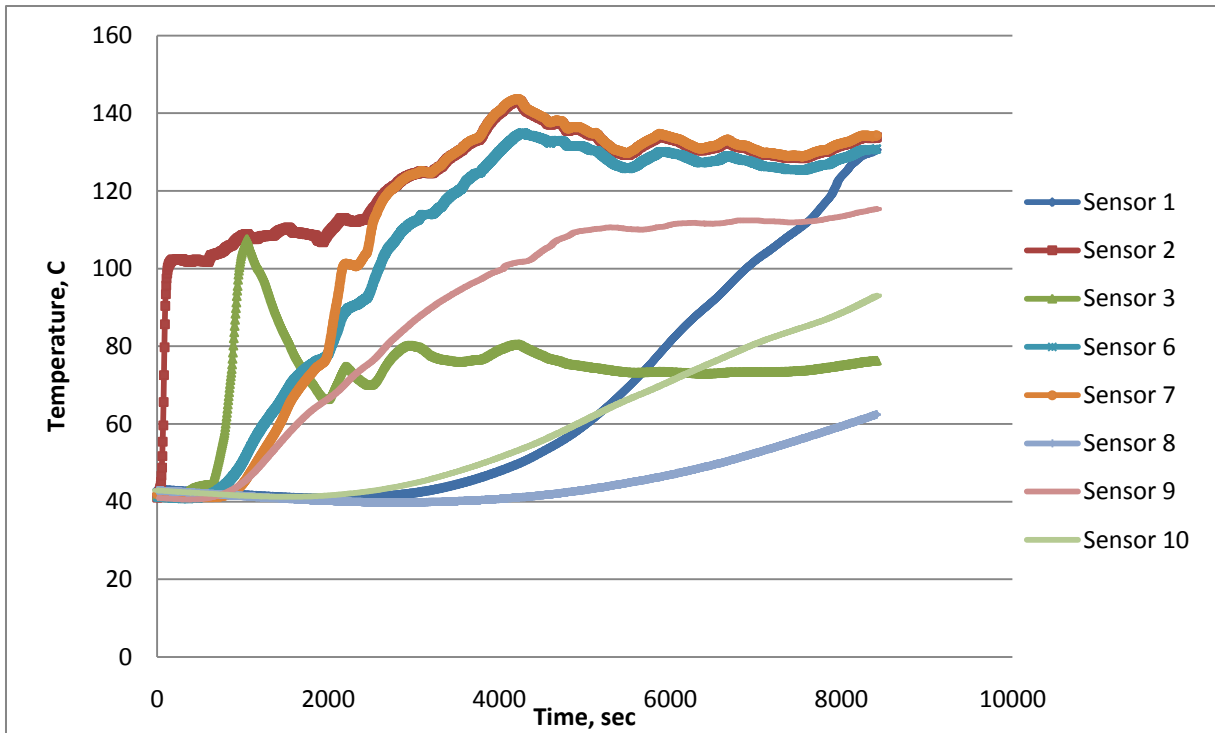
Figure 21: Temperature propagation in experiment 12, model 2

Figure 22: Pressure changes during experiments 5-12, model 2

Experiment 5 (Experimental model 2)

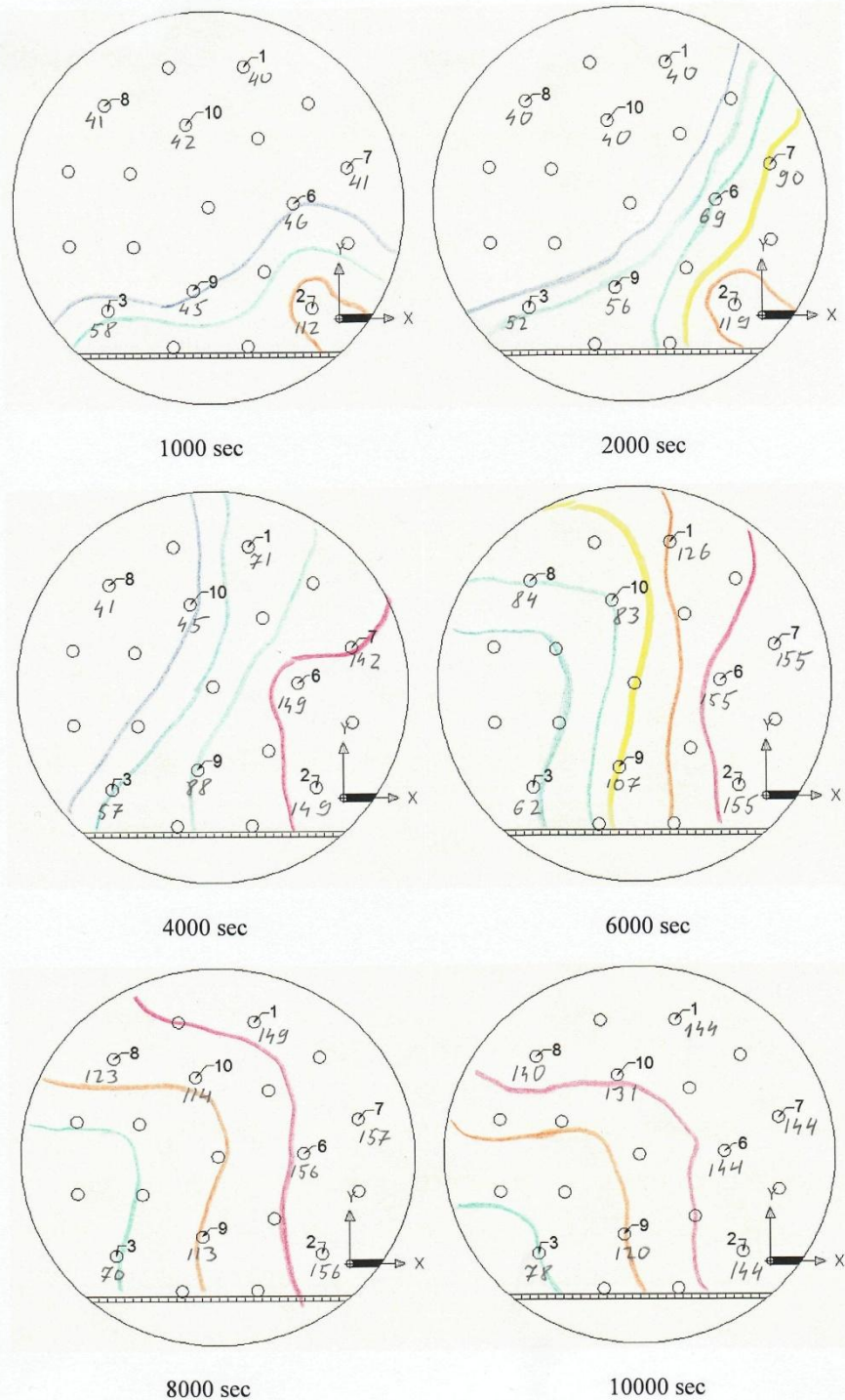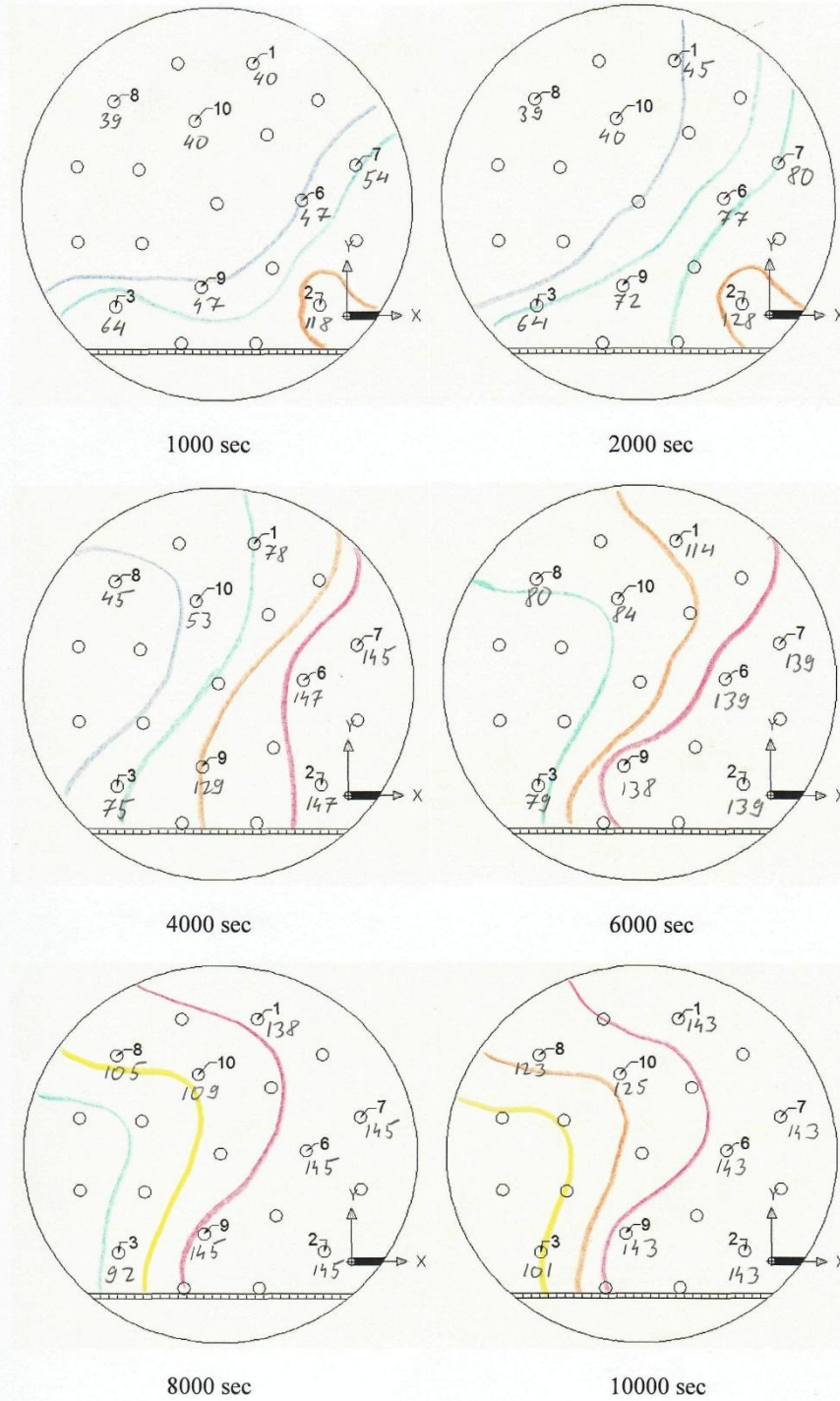500 sec

1000 sec

1500 sec

2000 sec

2500 sec

3000 sec
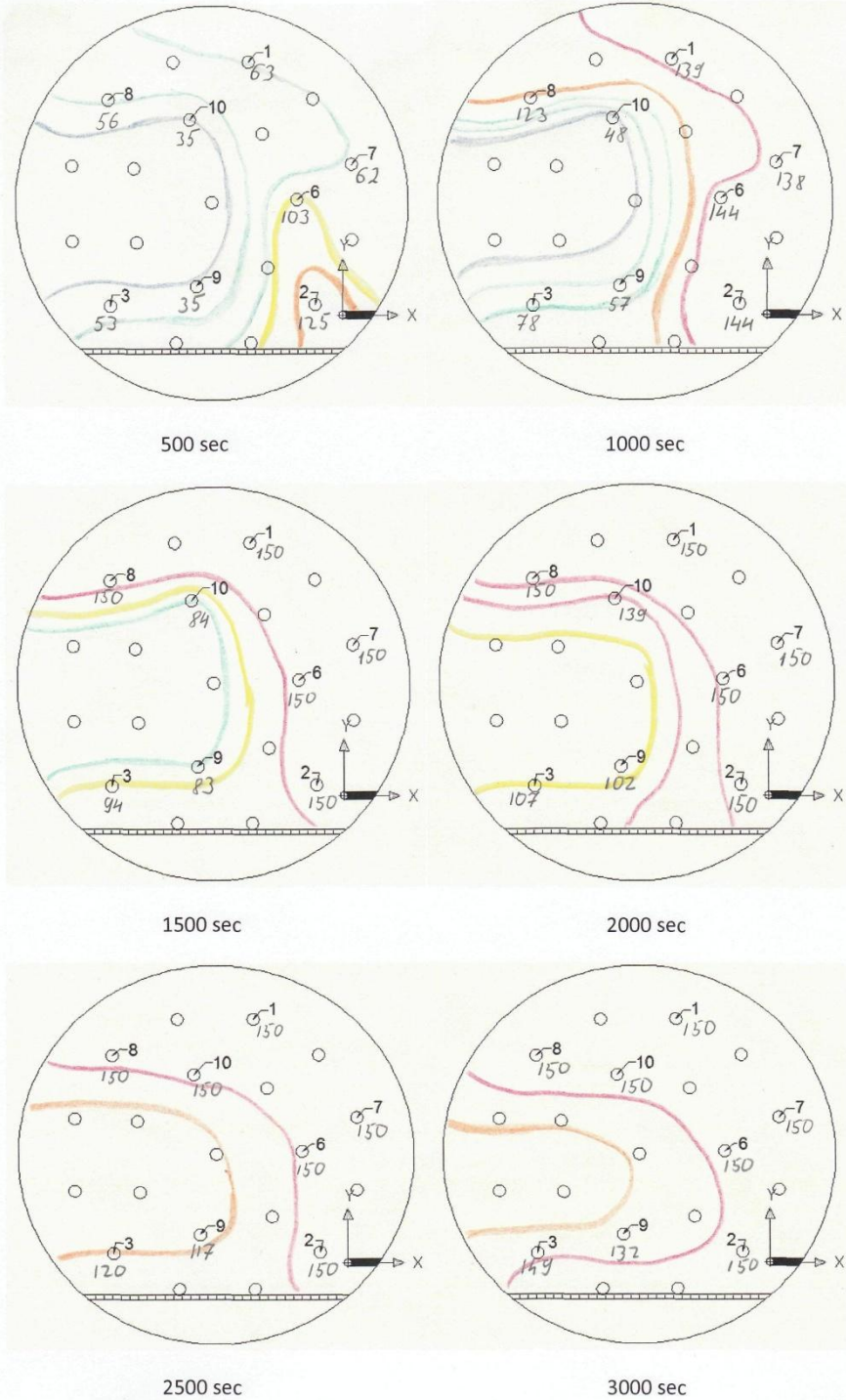
Figure 23: Temperature distribution in the experimental model 2 for different time intervals, experiment 5

Experiment 6 (Experimental model 2)

1000 sec   2000 sec

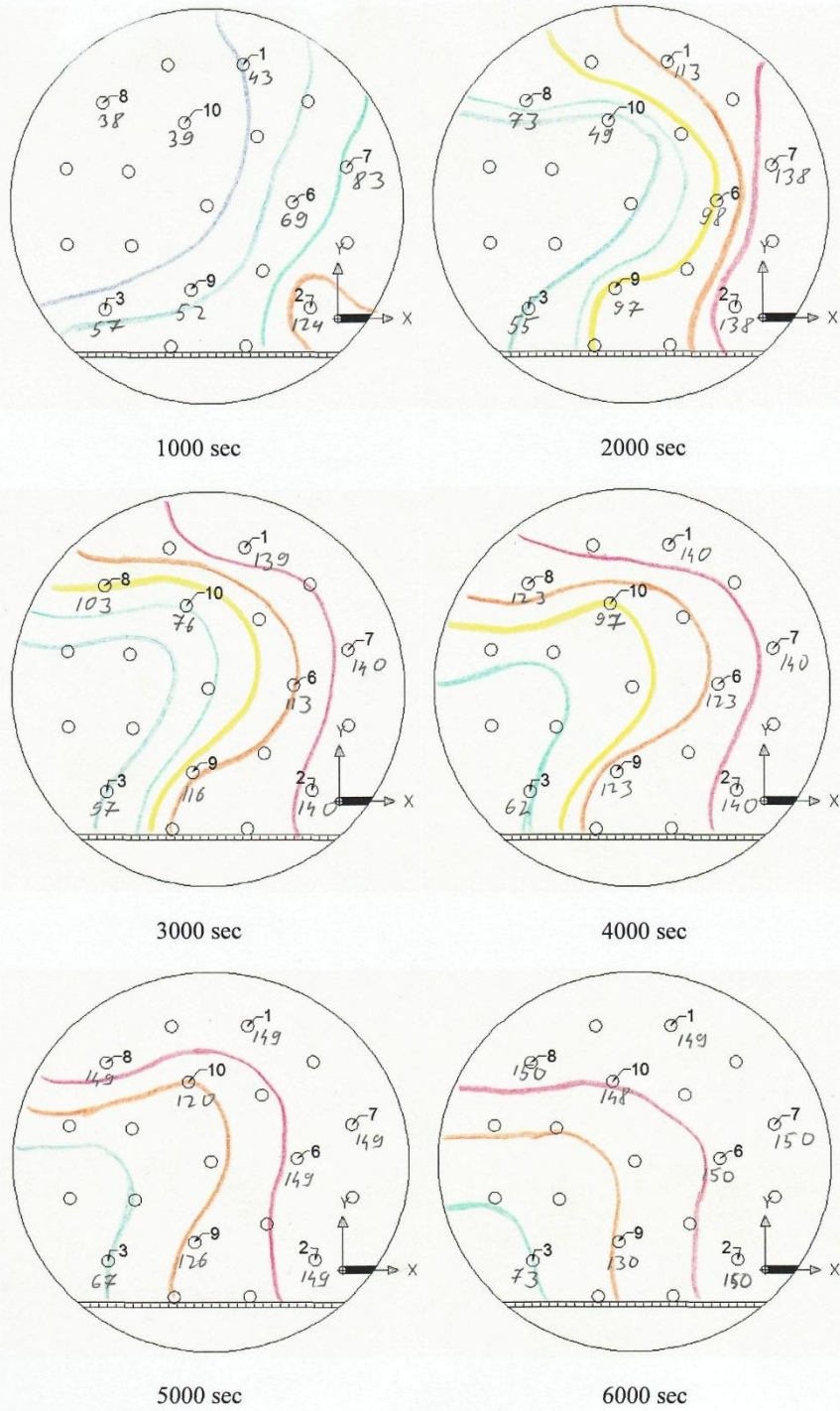3000 sec   4000 sec

5000 sec   6000 sec
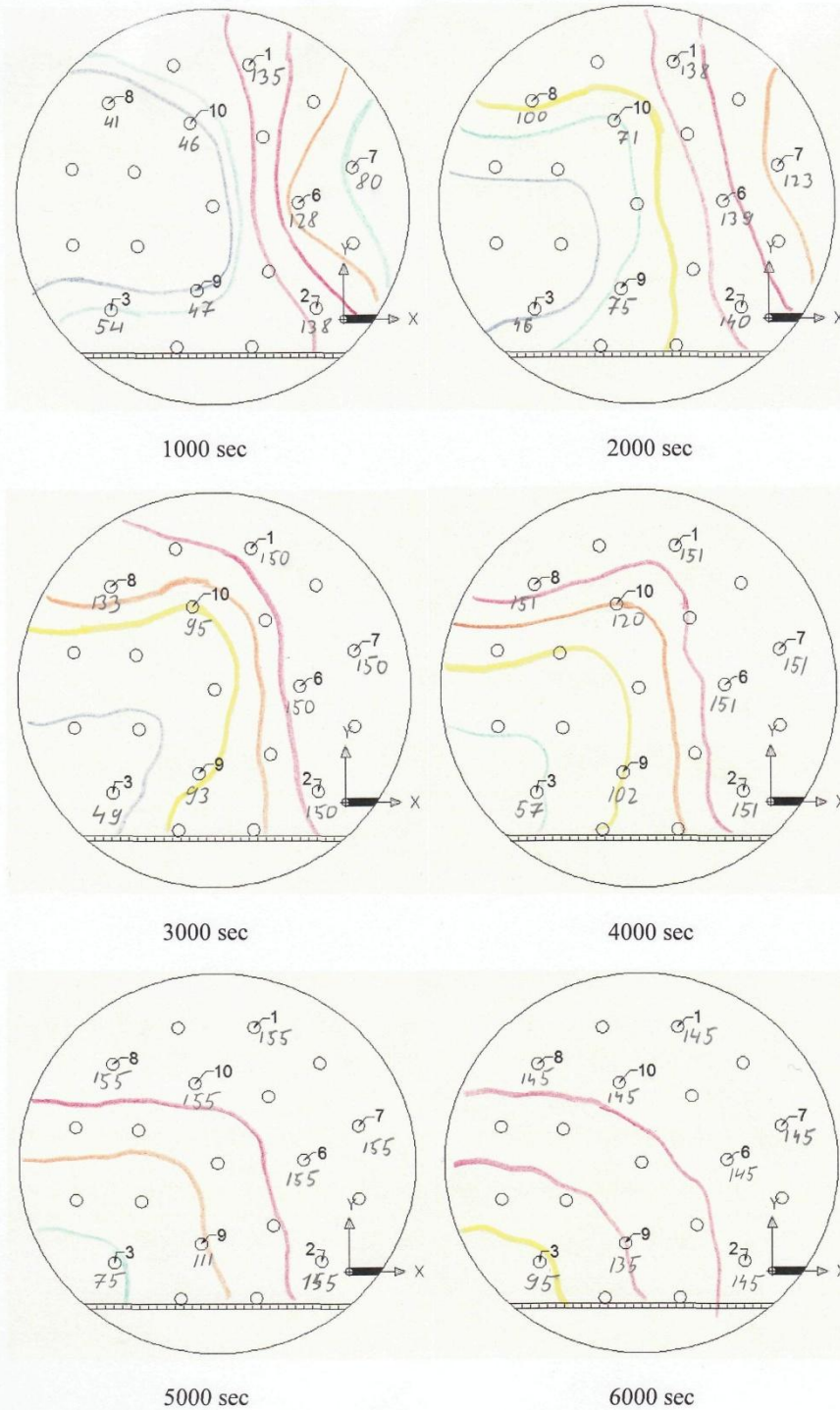
Figure 24: Temperature distribution in the experimental model 2 for different time intervals, experiment 6

Experiment 7 (Experimental model 2)

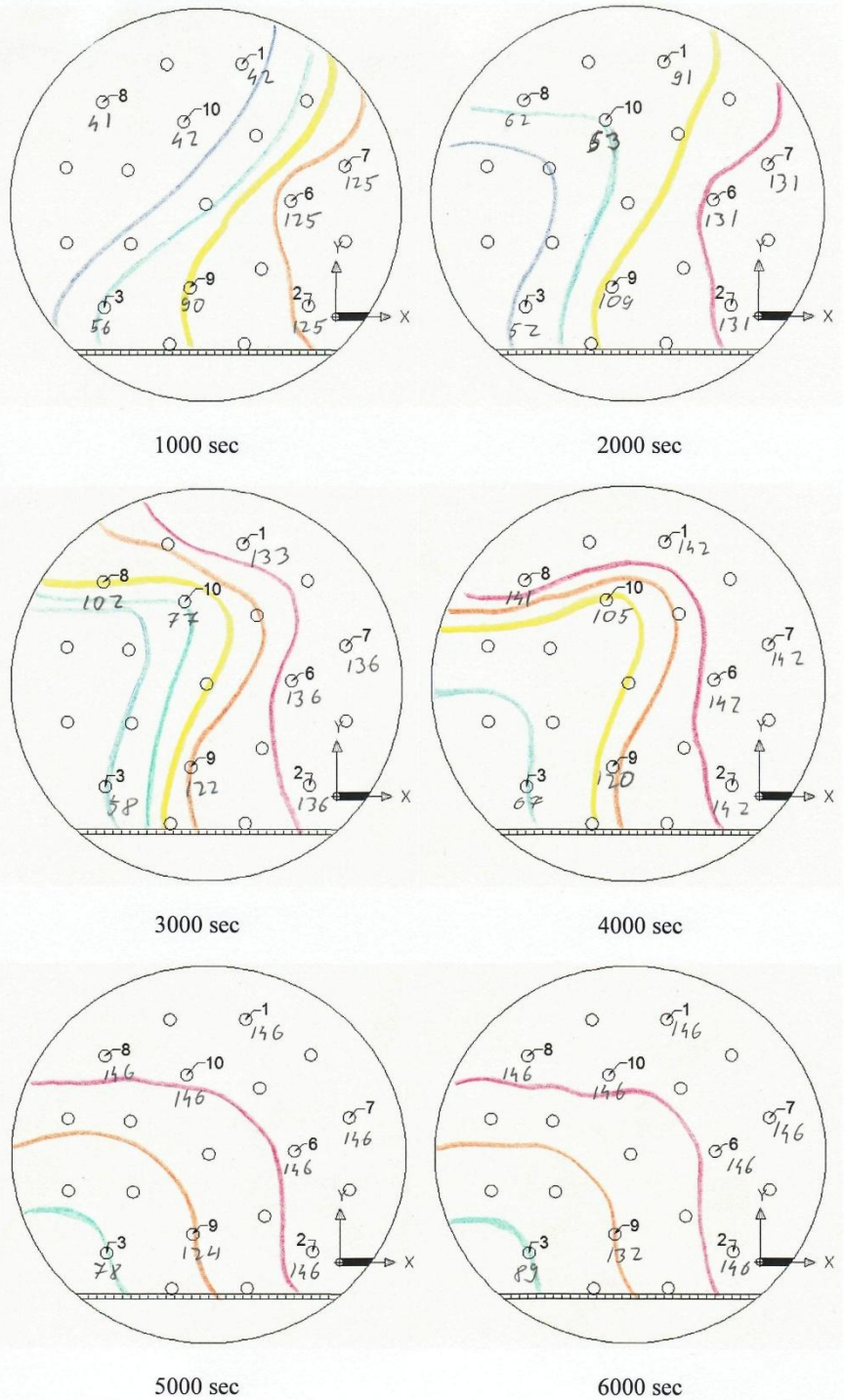1000 sec

2000 sec

4000 sec

6000 sec

8000 sec

10000 sec

Figure 25: Temperature distribution in the experimental model 2 for different time intervals, experiment 7

Experiment 8 (Experimental model 2)

1000 sec

2000 sec

4000 sec

6000 sec

8000 sec

10000 sec

Figure 26: Temperature distribution in the experimental model 2 for different time intervals, experiment 8

Figure 27: Temperature distribution in the experimental model 2 for different time intervals, experiment 9

Figure 28: Temperature distribution in the experimental model 2 for different time intervals, experiment 10

Experiment 11 (Experimental model 2)

1000 sec
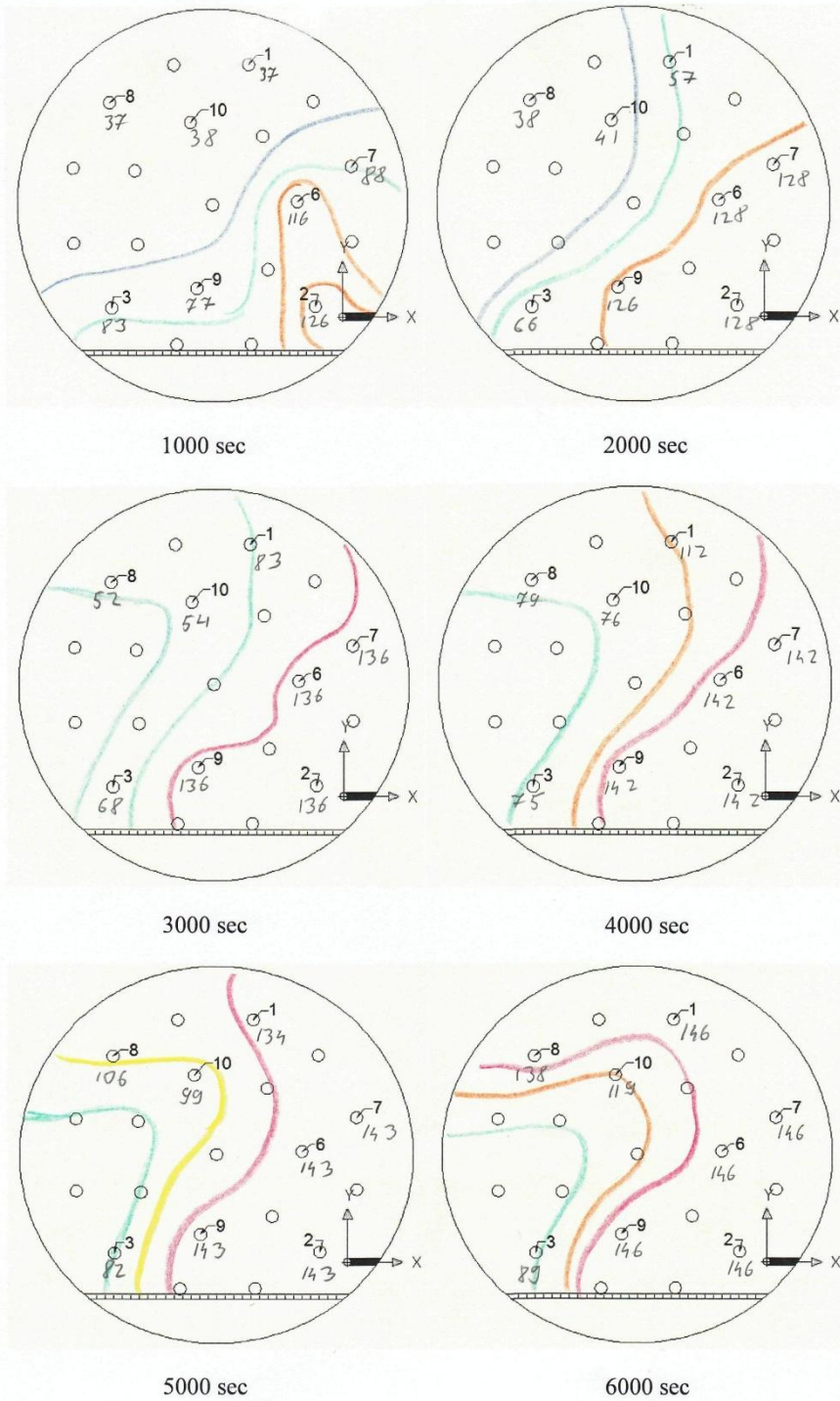
2000 sec

3000 sec

4000 sec

5000 sec

6000 sec

Figure 29: Temperature distribution in the experimental model 2 for different time intervals, experiment 11

Experiment 12 (Experimental model 2)

1000 sec
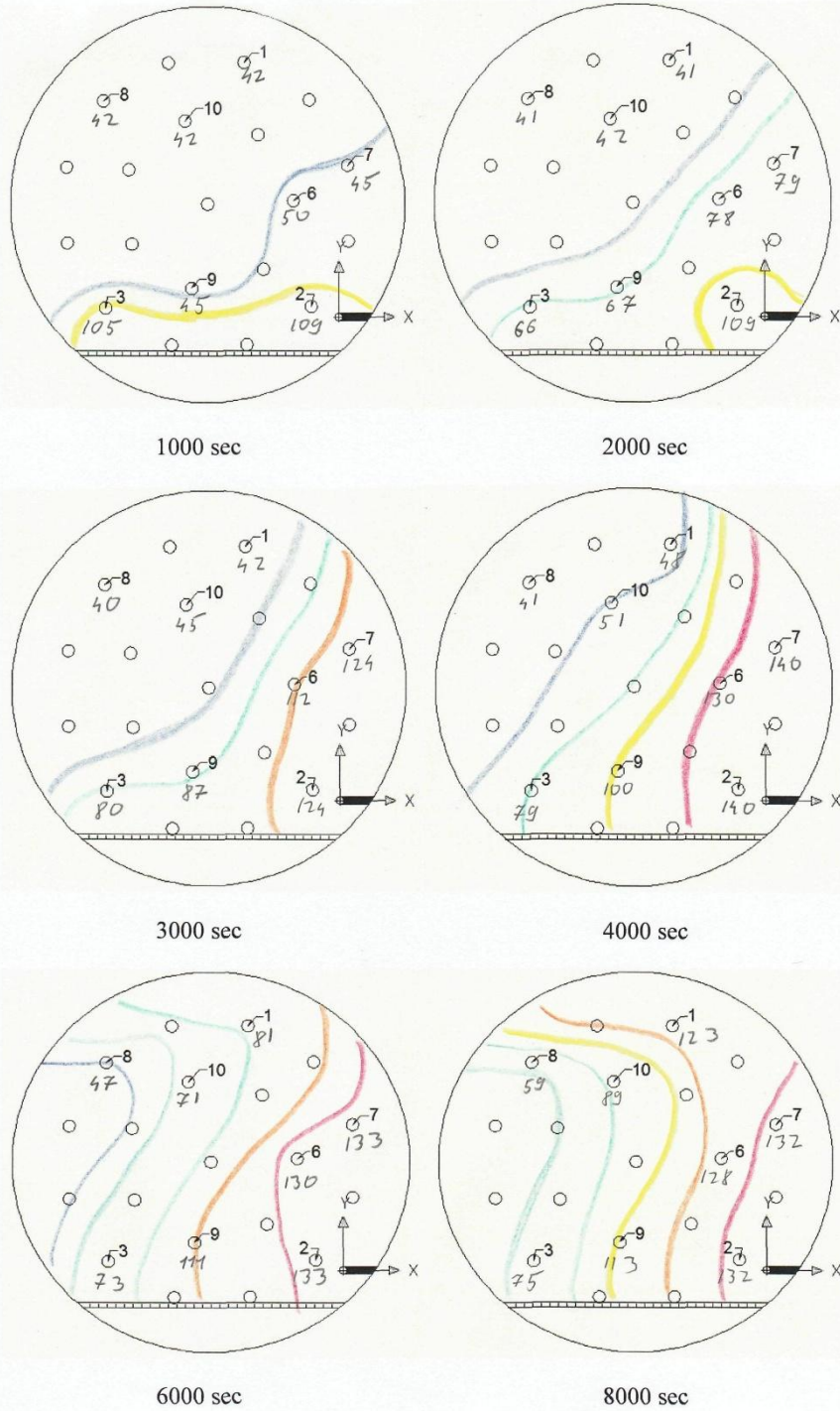
2000 sec

3000 sec

4000 sec

6000 sec

8000 sec

Figure 30: Temperature distribution in the experimental model 2 for different time intervals, experiment 12